TECH LIBRARY KAFB, NM
0060266

NASA CONTRACTOR REPORT

NASA CR-111
C. 1

NASA CR-1166

LOAN COPY: RETURN TO
AFWL (WLOL)
KIRTLAND AFB, N MEX

INVESTIGATION OF METHODS FOR PREDICTING THE AERODYNAMIC CHARACTERISTICS OF TWO-LOBED PARAWINGS

by M. R. Mendenhall, S. B. Spangler, and J. N. Nielsen

Prepared by
NIELSEN ENGINEERING & RESEARCH, INC.
Palo Alto, Calif.
for Langley Research Center

NATIONAL AERONAUTICS AND SPACE ADMINISTRATION • WASHINGTON, D. C. • SEPTEMBER 1968

TECH LIBRARY KAFB, NM

0060266

NASA CR-1166

INVESTIGATION OF METHODS FOR PREDICTING THE AERODYNAMIC CHARACTERISTICS OF TWO-LOBED PARAWINGS

add e-t: methods ... parawings,

By M. R. Mendenhall, S. B. Spangler, and J. N. Nielsen

Sep 68

Distribution of this report is provided in the interest of information exchange. Responsibility for the contents resides in the author or organization that prepared it.

~~Prepared under Contract No. NAS 1-6615 by~~

M.e. NIELSEN ENGINEERING & RES~~EARCH,~~ INC.
~~Palo Alto, Calif.~~

~~for Langley Research Center~~

~~NATIONAL AERONAUTICS AND SPACE ADMINISTRATION~~

For sale by the Clearinghouse for Federal Scientific and Technical Information
Springfield, Virginia 22151 – CFSTI price $3.00

TABLE OF CONTENTS

	Page No.
SUMMARY	1
INTRODUCTION	2
SYMBOLS	2
BASIC APPROACH TO THE PREDICTION METHODS	6
ANALYSIS	7
Canopy Shape Theory	7
Basic Canopy Aerodynamic Theory	8
Weissinger method	8
Pitching moment due to camber	9
Multhopp method	9
Profile-Drag Calculation	10
Section data	10
c_ℓ-method	12
α-method	14
Polhamus method	14
Effect of Leading-Edge Booms on Wing Characteristics	15
Iterative Nonlinear Lift Prediction Method	17
Luffing Boundary	18
RESULTS	20
Accuracy of Lifting-Surface Methods	20
Canopy Shape Studies	22
Comparison Between Experiment and Theory for Rigid Wings	23
Systematic data available	23
Lift	24
Drag	25
Pitching moment	27
Effect of Leading-Edge Booms on Wing Characteristics	29
Analytical investigation	29
Empirical investigation	30
Comparison Between Experiment and Theory for Flexible Wings	33
Systematic data available	33
Lift	33
Drag	34
Pitching moment	37
Luffing boundary	38

	Page No.
Limitations of the Theoretical Methods	39
Slackness ratio	39
Section data	40
Linear lift coefficient range	40
Viscous effects	40
CONCLUDING REMARKS	41
APPENDIX A - CALCULATION OF CAMBER AND TWIST DISTRIBUTIONS FOR A PARAWING LOBE FORMED FROM A RIGHT-CIRCULAR CONE	45
APPENDIX B - COMPARISON OF WEISSINGER AND MULTHOPP METHODS	53
REFERENCES	61
TABLES I AND II	63
FIGURES 1 THROUGH 26	66

INVESTIGATION OF METHODS FOR PREDICTING THE AERODYNAMIC CHARACTERISTICS OF TWO-LOBED PARAWINGS

By M. R. Mendenhall, S. B. Spangler,
and J. N. Nielsen
Nielsen Engineering & Research, Inc.

SUMMARY

The present study seeks to develop accurate methods for predicting the longitudinal aerodynamic characteristics of two-lobed conical parawings with leading-edge booms for high aspect ratios and high slackness. For prediction purposes, the assumption was made that the booms and canopy can be considered separately. The canopy was then considered to have a known shape for purposes of determining its aerodynamic performance. Various theoretical methods were studied for determining canopy aerodynamic characteristics, including profile drag. Force increments due to the leading-edge booms were studied both analytically and empirically.

Comparisons were made between theory and data for rigid wings of known shape with no leading-edge booms to check the canopy prediction methods. For approximately triangular wings of aspect ratios 3 and 4, good agreement was obtained for lift and moment within the range where no separation exists. The predicted drag was less than measured values, with the difference being small at moderate lift coefficients and increasing with increasing lift coefficient.

Comparisons were made for flexible wings of triangular and NASA planforms with leading-edge booms for overall evaluation of the methods. The canopy shape assumption was checked by comparison with earlier slender-body results, and the aerodynamic performance was found to be insensitive to small shape differences. Analytical estimates of the boom force increments, based on section data, were too small. Comparisons of data for rigid wings (with no booms) and flexible wings indicated the boom force and moment increments to depend on boom size and taper, and on method of canopy attachment to the booms. Systematic force and moment increments were found empirically in some cases. The major sources of differences between the primary prediction method and either data or more accurate theoretical methods are viscous effects and chordwise variations of induced downwash and loading.

INTRODUCTION

A large amount of research has been conducted on parawings with rigid leading edges, primarily at the Langley Research Center, NASA. Most of the work has been experimental in nature and has considered wings of moderate to high aspect ratio with relatively high slackness. The Office of Naval Research has sponsored a theoretical investigation of parawing aerodynamics (refs. 1 through 4) for parawings of low aspect ratio, small slackness, and no leading-edge booms. Polhamus and Naeseth (ref. 5) have predicted the lift and moment of conical and cylindrical parawings with high slackness using lifting-surface theory in connection with an analytical assumption for the canopy shape. Nielsen and Burnell (ref. 6) have considered such effects as profile drag, leading-edge booms, keel incidence, and bolt ropes, but these were treated primarily in an empirical fashion.

The purpose of the present investigation is to develop rational, analytical methods for predicting the longitudinal aerodynamic characteristics of two-lobed parawings of high slackness and high aspect ratio with leading-edge booms. The methods are developed for incompressible flow. The general approach is to prescribe an analytical shape for the canopy rather than attempt to solve simultaneously for shape and loading, as was done in reference 2. The experimental observations of the NASA work (refs. 5 and 7, for instance) form the basis for the shape selection. For the known shape, lift, induced and profile drags, pitching moment, center of pressure, and luffing angle are predicted. The leading-edge booms and basic canopy are considered separately, and their forces and moments are added to obtain overall values for the parawing. Experimental results on rigid conical parawings with no leading-edge booms are used to verify the basic canopy prediction methods. The final methods are compared and evaluated using flexible wing data obtained principally at the Langley Research Center.

SYMBOLS

A	aspect ratio, b^2/S
b	wing span
c	wing chord

c_d	section drag coefficient, based on c
c_{d_p}	section profile-drag coefficient, based on c
c_ℓ	section lift coefficient, based on c
c'_ℓ	equivalent wing lift coefficient, equation (7)
c_{ℓ_α}	section lift-curve slope, per radian
c_{m_o}	section moment coefficient for zero section lift, based on c
c_r	root chord
Δc_d	incremental section drag coefficient due to camber, based on c
Δc_ℓ	incremental section lift coefficient due to camber, based on c
C_D	wing drag coefficient, based on S
C_{D_i}	wing induced-drag coefficient, based on S
$C_{D_{i_o}}$	wing induced-drag coefficient at zero wing lift, based on S
C_{D_p}	wing profile-drag coefficient, based on S
C_L	wing lift coefficient, based on S
C_{L_α}	wing lift-curve slope, $dC_L/d\alpha$, per radian
C_m	wing moment coefficient taken about designated center of moments, based on S and ℓ_r
C_{m_o}	wing moment coefficient at zero wing lift, based on S and ℓ_r
C_{m_α}	wing moment-curve slope, $dC_m/d\alpha$, per radian
d	diameter of leading-edge booms
D'	profile drag parameter, $(cc_{d_p}/2b)$
f	maximum ordinate of the mean line for circular arc camber, figure 4(a)
G_ν	loading parameter for lift, $(cc_\ell/2b)_\nu$
G_{o_ν}	value of G_ν for no local leading-edge suction
ℓ	trailing-edge length of inflated parawing in planform, $\overline{AC'}$ in figure A-4
ℓ'	canopy trailing-edge length of inflated triangular parawing, figure 8

ℓ_i	distance from wing apex to a point on the trailing edge in uninflated state (Appendix A)
ℓ_o	trailing-edge length of uninflated parawing, $\overline{AC}$ in figure A-2
ℓ_r	reference length
$\frac{\ell_o - \ell}{\ell}$	slackness ratio, equation (A-21)
$\frac{\ell' - 2s}{2s}$	triangular wing slackness ratio
L	distance from wing apex to a point assumed on trailing edge of wing in the inflated state, equation (A-18)
m	number of control points across the span in the Weissinger and Multhopp methods
M'_ν	pitching-moment parameter for zero section lift, $\left[\frac{\left(c_{m_o}\right)_\nu c_\nu^2}{2b}\right]$
n	number of control points across chord in Multhopp method
q	free-stream dynamic pressure
r	radius of base of right circular cone, figure A-3
R	slackness ratio, equation (A-21), also used to indicate root stall in the figures
Re_c	Reynolds number based on chord, $\rho V_\infty c/\mu$
Re_d	Reynolds number based on leading-edge diameter, $\rho V_\infty d/\mu$
s	semispan of triangular wing
S	wing planform area, inflated
T	spanwise fabric tension per unit chord, also used to indicate tip stall on the figures
V_∞	free-stream velocity
x_{cm}	distance from wing apex to the center of moments
x_{cp}	value of x at the wing center of pressure
x,y,z	wing axes, figure 1
x_t, y_t, z_t	value of x,y,z at trailing edge
x_o, y_o, z_o	cone axes, figure A-1
x_1, y_1, z_1	rotated cone axes, figure A-1
y^*, z^*	y/x, z/x
α	wing geometric angle of attack measured relative to the root chord

α_o	geometric angle of attack for zero wing lift, measured relative to the root chord
$(\alpha_o)_\nu$	angle of zero lift of local airfoil section due to camber as calculated by reference 9
β	half the angle subtended by the lobe trailing edge, figure 1
γ	polar angle measured from x-axis for uninflated planform, figure A-2
ϵ	semiapex angle of inflated planform, $90^\circ - \Lambda$
ϵ_{eff}	revised twist to account for camber, $\epsilon_\nu - (\alpha_o)_\nu$
ϵ_ν	angle between chord line at z_ν and the plane of the leading edge and keel, positive if increasing ϵ_ν increases local angle of attack
η	fractional semispan, $z/(b/2)$
η_{cp}	spanwise location of center of pressure
η_ν	specific value of η, $\eta_\nu = \cos\left(\frac{\nu\pi}{m + 1}\right)$
θ	semiapex angle of one wing panel in inflated state, figure 1
θ_o	semiapex angle of one wing panel in uninflated state, figure 1
λ	leading-edge length; also tension parameter of reference 2, $T/(4\ sq\ \tan^2\epsilon)$
Λ	sweepback angle of leading edge of inflated wing
Λ_o	sweepback angle of leading edge of uninflated wing
$\Lambda_{1/4}$	sweepback angle of quarter-chord line of inflated wing
$\Delta\Lambda$	$\Lambda - \Lambda_o$
μ	absolute viscosity
ν	integer indicating the spanwise control point in Weissinger method, $1 \leq \nu \leq m$
ξ, ζ	coordinates parallel and perpendicular to local chord, respectively, figure 2
ρ	free-stream density
σ	angle between x_1 and x_o axes, figure 1
ϕ	angle between x and x_o axes, figure 1; also, transformed spanwise distance, $\phi = \cos^{-1}\eta$

Subscripts

cam	camber
ex	experiment
j	denotes value of D' at j'th spanwise station, equation (5)
luff	denotes condition of canopy luffing

M	Multhopp
n	denotes value at n'th chordwise station, equations (A-25) and (A-26), $1 \leq n \leq 13$
th	theory
W	Weissinger
ν	denotes specific Weissinger control point along span

BASIC APPROACH TO THE PREDICTION METHODS

Prediction of the aerodynamic characteristics of a parawing with leading-edge booms requires consideration of a number of inviscid and viscous phenomena. The approach taken here is to predict as many of the effects as possible on a rational basis. The remaining effects, which are expected to be a small part of the overall characteristics, are then treated on an empirical basis.

It is assumed initially that the leading-edge booms and the basic canopy can be considered separately for purposes of computing parawing aerodynamic characteristics. This assumption implies that the boom size be relatively small compared to a characteristic canopy dimension, such as root chord. The basic canopy aerodynamic characteristics are predicted, and force and moment increments due to the leading edge are added to obtain overall parawing performance.

The basic approach of reference 5 to the prediction of the canopy lift and moment was selected for the present study. The assumption is made, on the basis of experimental observations, that each lobe of the canopy forms a portion of the surface of a right circular cone, with the root chord and leading edge lying along the slant heights of the cone. With this assumption, the coordinates of any point on the canopy and the camber and geometric twist distributions can be predicted. The canopy lift, moment, and induced drag are computed using the Weissinger method (ref. 8). Since this method does not account directly for camber, the Pankhurst method (ref. 9) is used to compute the section angles of zero lift, which are added to the geometric twist angles to obtain an effective twist distribution. In this manner, the twisted, cambered canopy is replaced by an equivalent uncambered, twisted wing. A correction to the Weissinger zero-lift pitching moment must be made to account properly for camber. The correction is made using the section zero-lift pitching moment from reference 9.

The profile drag of the canopy is computed using a strip-theory approach and section data for thin plates with circular-arc camber. Several methods for using the section data were investigated. Where these methods require local lift coefficients or local angles of attack, the values obtained from the Weissinger results are used. The section drag coefficients are integrated over the span to obtain the wing profile drag.

The force and moment increments due to addition of the leading-edge booms are examined from both analytical and empirical points of view. Proper treatment of leading-edge booms involves consideration of a number of variables, including Reynolds number, diameter-to-chord ratio, taper of the leading-edge booms, location of the attachment of the canopy to the booms, and method of attachment (pocket versus wrap attachment). The analytical approach makes use of section data for a thin flat plate attached to the top of a cylindrical leading edge, together with local flow conditions obtained from the Weissinger program. The empirical approach consists of examining the differences between data or theory for rigid wings with no leading edges and data for flexible wings with booms to deduce the force and moment increments due to the booms.

An investigation was made to determine the limitations on the prediction methods. The limitations are associated with large slackness ratios, induced camber and chordwise loading, canopy luffing, and flow separation at high lift coefficients. These are discussed in detail in the appropriate sections of this report.

ANALYSIS

Canopy Shape Theory

It is assumed in the present work, as in reference 5, that the canopy of each lobe of the parawing is part of the surface of a right-circular cone, with the root chord and the leading edge lying along the slant heights of the cone. The shape of the configuration is specified in terms of the root chord length, the leading-edge length, and the sweep angles of the uninflated and inflated parawing, as illustrated in figure 1. The details of calculating the surface coordinates are given in Appendix A. The flow directions at a local spanwise station are shown in figure 2.

Basic Canopy Aerodynamic Theory

The method used to obtain the basic canopy aerodynamic performance, except profile drag, is the Weissinger theory adapted to account for camber.

Weissinger method.- The form of the Weissinger lifting-surface theory presented in reference 8 was programed and run on an IBM 7094 digital computer. In this method, the wing is considered to be twisted, but uncambered. A lifting line is placed at the quarter chord. Its spanwise lift distribution is computed by satisfying the condition of zero flow through the wing at the three-quarter chord due to the combined effects of the free-stream velocity and the velocities induced by the lifting line and trailing vortex sheet. Camber is taken into account, insofar as lift is concerned, in the manner of reference 5 by adding to the geometric twist an additional twist given by the local angle of zero lift. The results of this computation are wing basic loading parameters, such as α_o and C_{m_o} (which must be corrected for camber), and additional loading parameters, such as C_{L_α}, dC_m/dC_L, the spanwise center of pressure, and the spanwise variation of loading.

For use with a cambered and twisted wing, the Weissinger method requires a knowledge of the section angles of zero lift at several spanwise stations. These angles were obtained using the Pankhurst method (ref. 9) in the fashion used in reference 5. Pankhurst presents a relation for $(\alpha_o)_\nu$ in terms of the camber ordinates at a number of specified chordwise stations. The chordwise stations corresponding to Spacing (4) of table 1 of reference 9 were used. The camber ordinates were obtained as described in Appendix A. The section effective twist angle used in the Weissinger method is then

$$\left(\epsilon_{eff}\right)_\nu = \epsilon_\nu - \left(\alpha_o\right)_\nu \tag{1}$$

The Weissinger method satisfies the zero-flow boundary condition at several discrete points along the span at the three-quarter chord line. For most of the results presented herein, 7 points across the span were used, based on the good agreement with data and with other analytical methods. Several comparisons were also made between 7- and 15-point solutions which verified the accuracy of the 7-point calculations for the wings of interest here.

The Weissinger method uses as input the values of wing chord at the spanwise stations for which the boundary conditions are satisfied. For parawings having large twist angles at the tip, the actual chord is considerably larger than the planform chord. Use of the actual chord rather than the planform chord helps account for nonplanar wing effects as shown by comparisons with data. Consequently, the actual chord distribution was used for all the results presented here.

Pitching moment due to camber.- The zero-lift moment determined by the Weissinger method for the equivalent, twisted, uncambered wing does not include the moment due to camber. The latter was determined by a strip theory approach. The pitching moment on the section at zero section lift (a pure couple) was determined and integrated over the span to get the wing moment due to camber. This moment is additive to the moment computed from the Weissinger method. Certain effects are ignored in this approach, and these are discussed in Appendix B.

The pitching moments for zero section lift were computed using the Pankhurst method (ref. 9) and the camber coordinates determined from the canopy conical shape fit. The chordwise coordinate spacing and constants of Spacing (4) of table 4 of reference 9 were used. The integration over the span is based on the following equation

$$\left(C_{m_o}\right)_{cam} = \frac{b^2}{\ell_r S} \int_{-1}^{1} \left[\frac{\left(C_{m_o}\right)_\nu c_\nu^{\,2}}{2b}\right] d\left(\frac{z}{b/2}\right) \tag{2}$$

Using the quadrature formula, equation (A-15) of reference 8, equation (2) becomes

$$\left(C_{m_o}\right)_{cam} = \frac{\pi A}{m+1} \frac{1}{\ell_r} \left[M'_{(m+1)/2} + 2 \sum_{\nu=1}^{(m-1)/2} M'_\nu \sin \phi_\nu\right] \tag{3}$$

Multhopp method.- The Weissinger method does not account for variations in induced downwash along the local chord lines due to the vortex system. This downwash effect is accounted for by the Multhopp method, which satisfies the normal flow boundary condition at various stations along each local chord. A modified Multhopp lifting-surface method was

applied to several wing configurations for which Weissinger results were available in order to evaluate the effect of induced camber and chordwise loading neglected in the Weissinger method. Calculations were run on an IBM 7094 computer with NASA LRC Program No. A0313.[1] Generally, 6 chordwise stations were used, and the number of spanwise stations were then selected according to a relation dependent on aspect ratio given in the instructions on use of the program.

Profile-Drag Calculation

Profile drag generally is not predictable theoretically. The method of this report uses section data locally along the span in a strip-theory approach to estimate wing profile drag. The available section data are described below together with the several methods investigated for estimating wing profile drag from section data.

Section data.- The basic airfoil section chosen to represent the canopy of a parawing is that of a thin, cambered plate with semicircular leading edges, since data on rigid parawings using this section are available. Since section data for such an airfoil are unavailable over a wide angle of attack range, the section characteristics were approximated as described in the following paragraphs.

Section lift and drag data on a flat plate with a sharp leading edge are available in reference 11 and are shown in figure 3. In figure 3(a) the lift curve for the thin two-dimensional plate with a sharp leading edge is compared with those for NACA 0006 and NACA 64-006 sections from references 12 and 13, respectively. The differences in the nonlinear lift range are due to Reynolds number effects on the separated flow. These differences were neglected, and the smooth lift curve for the flat plate was adopted.

Some concern is expressed in reference 11 about the reliability of the drag data, shown in figures 3(b) and (c), at $\alpha < 20^{\circ}$ where leading-edge shape would have an important effect on profile drag. Data at low angles of attack for a thin plate with semicircular leading and trailing

[1]This program is a modified Multhopp lifting-surface program. The modifications include the extension to higher-order chordwise loading terms as developed by van Spiegel and Wouters (ref. 10) and refinements in the numerical procedure by John E. Lamar of the Langley Research Center.

edges were taken from reference 14 and are plotted on figures 3(b) and (c). The smooth curve was faired between the two sets of data to produce a section drag curve for a wide range of angle of attack.

No section data were found for cambered plates with semicircular leading and trailing edges but some data were found in reference 15 for wings using such a section. These data, shown in figure 4, are for a plate of aspect ratio 5 with semicircular leading and trailing edges, circular arc camber, and a taper ratio of one. These data were used to obtain lift and drag coefficient increments due to camber which were then added to the two-dimensional flat-plate data, as follows. The lift coefficient increment due to camber, Δc_ℓ, was obtained from figure 4(a) as the difference between the lift coefficient of the plate with camber and that without camber at the specified angle of attack. The drag coefficient increments due to camber, Δc_d, were obtained in a similar manner, using figure 4(b). However, the drag data were corrected to infinite aspect ratio before the differences were taken. This correction, made by removing the induced drag, $C_L{}^2/\pi A$, from each curve in figure 4(b), is very small. Some effect of finite aspect ratio probably still exists in both Δc_ℓ and Δc_d.

The section data used for all profile-drag calculations were obtained by adding the smoothed camber increments to the flat-plate data of figure 3. The resulting set of curves is shown in figure 5. Linear interpolation was used between the camber values shown in this figure.

In figure 5(a), it is interesting to note that the section lift curves become nonlinear at the same angle of attack for every camber value. The increments due to camber in the range 0° to 10° angle of attack in figure 4(a) are reasonably smooth. When these increments are added to the flat-plate curve of figure 3(a), all the resulting curves indicate the characteristic break at 8°. The stall characteristics shown in figure 4(a) for wings of aspect ratio 5 may occur at angles of attack higher than 8° as a result of the relieving effect of finite aspect ratio.

It is also of interest to note from the cambered plate data that neither the theoretical lift nor the theoretical moment due to camber is developed experimentally. The table below indicates, for two values of camber, the theoretical values of the section-lift coefficient at $\alpha = 0$ and the section moment at zero lift as determined from Pankhurst (ref. 9), together with the experimental values of the quantities from reference 15.

Camber Fraction	$c_{\ell_{\alpha=o}}$		c_{m_o}	
	Theo.	Exp.	Theo.	Exp.
0.05	0.63	0.31	-0.16	-0.07
.10	1.26	.60	- .32	- .08

It is apparent that about half of the predicted lift is actually developed and less than half of the moment is developed. Since the finite aspect ratio influence is not sufficient to account for these differences, viscous effects are probably the main cause.

The angle of attack range $-8^{\circ} \leq \alpha \leq 8^{\circ}$ is defined as the "linear range" of the section data and will be referred to without quotation marks hereafter. The camber and twist distributions of parawings cause large variations in local section-lift coefficient across the span of the parawing so that some sections of the wing may operate in the linear range of the section data while others may not. Questions arise in how to apply section data to spanwise sections operating in the nonlinear range. Several methods of applying section data to the calculation of wing profile drag were investigated to shed light on this question and on the question of the importance of induced camber effects on drag.

c_ℓ-method.- At the local lift coefficient, c_{ℓ_ν}, given by the Weissinger method, the corresponding profile-drag coefficient, $c_{d_{p_\nu}}$, was found in the section data of figure 5(c) for the actual cambered section. These values were then integrated over the span according to the following equation

$$C_{D_p} = \frac{b^2}{S} \int_{-1}^{1} \left[\frac{\left(c_{d_p}\right)_\nu c_\nu}{2b} \right] d\left(\frac{z}{b/2}\right) \tag{4}$$

to obtain the wing profile drag coefficient.[2] The integration was performed using the trapezoidal rule with 22 points across the semispan,

[2]This approach implies the use of the free-stream direction as the reference direction for section lift and drag. An alternate approach is to determine a local flow direction from c_ℓ and c_{ℓ_α}, to obtain the lift coefficient normal to the local direction from c_ℓ and c_{d_i}, and to use this lift coefficient with section data to determine profile drag. While the alternate approach may have merit, it was not used because of its complexity compared to that of the present approach.

$$C_{D_p} = 2A \sum_{j=1}^{21} \left(\frac{D'_{j+1} + D'_j}{2}\right)\left(\eta_{j+1} - \eta_j\right) \tag{5}$$

The points were chosen as follows to give a good sampling of the root or tip regions in cases of root stall or tip stall.

$$\eta = 0(0.02)0.2;\ 0.2(0.1)0.8;\ 0.85;\ 0.9;\ 0.95;\ 0.99;\ 1.0$$

Computation of local values of c_{d_p} requires simultaneous values of local lift coefficient and local section camber. The local values of c_ℓ were obtained from the Weissinger Fourier series representation of c_ℓ. A similar Fourier series was not found accurate enough for estimating the intermediate values of camber. Instead a 5-parameter polynomial was used which matched the known cambers at the Weissinger stations and yielded zero camber at the wing tip and root as well.

An interesting point arises in applying the foregoing analysis at high section-lift coefficients. With reference to figure 5(c), near a lift coefficient of 0.85, a reversal occurs in the drag curve for zero camber and the drag coefficient becomes a multivalued function of lift coefficient. However, the local lift coefficient predicted by the Weissinger method increases monotonically with α. Therefore, the drag was assumed to increase discontinuously as shown by the dashed line. When the section-lift coefficients at the spanwise points of the drag integration are equal to those for which discontinuities occur in the section drag curves, discontinuities are introduced into the wing drag curve. Since many spanwise stations are used, these discontinuities have a negligibly small effect, and a continuous wing drag curve results. The method also has the property that it estimates where wing stall first occurs and how it spreads as angle of attack increases.

No adjustments were made to the two-dimensional profile-drag coefficients to account for leading-edge sweep effects in either the c_ℓ- or α-methods. It might be possible to develop an adjustment means using the work of Polhamus reported in reference 16. He showed that for a given wing-lift coefficient, the leading-edge suction force increases as the aspect ratio decreases for a given planform type. For wings of

triangular or NASA planform,[3] a decrease in aspect ratio corresponds to an increase in leading-edge sweep angle. Thus, for such wings, the suction force would increase with increasing sweep angle. If the assumptions are made that all leading-edge suction is lost due to leading-edge flow separation and that the lost suction force appears as profile drag, then a theoretical variation of this profile drag with leading-edge sweep angle can be obtained. This reasoning would indicate that the profile drag should increase with increasing sweep angle. No attempt was made to develop such an approach as an adjustment to the strip methods described herein.

α-method.- The local section profile drag is found as a function of local section angle of attack in this method. The local streamwise section angle of attack is determined in accordance with the Weissinger method as follows

$$\alpha_\nu = \left(\alpha_o\right)_\nu + \frac{c_{\ell_\nu}}{c_{\ell_\alpha}} \tag{6}$$

with $c_{\ell_\alpha} = 2\pi$.

The local angle of zero lift, $(\alpha_o)_\nu$, appears in equation (6) because, in the use of the Weissinger method, camber is converted to an equivalent twist. A 5-parameter polynomial was used to estimate the intermediate values of α_o. The local profile-drag coefficient was found from figure 5(b) for the actual cambered section at angle of attack α_ν, and the total wing profile-drag coefficient was obtained from equation (5) as before. It is noted that the drag coefficient is a single-valued function of α so that no discontinuities arise in this case as in the case of the c_ℓ-method. Neither the c_ℓ-method nor the α-method include any effect of chordwise loading or induced camber.

Polhamus method.- In reference 16, Polhamus was able to correlate the profile drag due to lift for rectangular wings (having leading-edge separation) when induced camber effects are large. The application of the method to uncambered and untwisted wings with swept leading edges is possible with the assumption of elliptical span loading. The basic method yields an equivalent airfoil lift coefficient, c'_ℓ, for which the

[3]A NASA planform wing is defined as a wing having a root chord and leading edges of equal length.

section profile drag is equal to that for the wing acting at a lower lift coefficient, C_L. The following result for c'_ℓ is taken from reference 16.

$$c'_\ell = C_L\left(\frac{2\pi}{C_{L_\alpha}} - \frac{2}{A}\right)^{1/2} \tag{7}$$

Using Weissinger results for C_{L_α}, c'_ℓ is computed from equation (7) and C_{D_p} is read from the uncambered section data curve in figure 5(c). The total wing drag coefficient is then

$$C_D = C_{D_p} + C_{D_i} \tag{8}$$

where C_{D_i} is the induced-drag coefficient from Weissinger.

Since the effect of induced camber on profile drag becomes more important as aspect ratio decreases, it is desirable to know for a given planform what the lower limit of aspect ratio is at which induced-camber drag achieves a certain value. The induced-camber effects were evaluated by the calculated differences in wing drag coefficient estimated by the α- or c_ℓ-methods and the Polhamus method.

Effect of Leading-Edge Booms on Wing Characteristics

Leading-edge boom effects on wing forces and moments were investigated from both the empirical and theoretical standpoints. The empirical approach consists of evaluating differences in force and moment data between flexible wings with leading-edge booms, and conical rigid wings having the same aspect ratio, planform, and slackness but no leading-edge booms. The differences are interpreted as leading-edge effects, although there may possibly be some differences due to canopy shape. The results are discussed in a subsequent section. The theoretical approach consists of using two-dimensional data on plates with cylindrical leading edges in an attempt to gain an understanding of the three-dimensional boom problem. The methods are discussed here, and the results are discussed in a subsequent section.

The only systematic section data found for plates with cylindrical leading-edge booms are unpublished Langley Research Center data (hereafter called splitter-plate data). The data used are for a flat plate tangent to the top of the cylinder, as shown below.

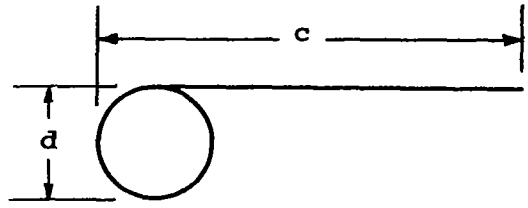

Data were obtained for diameter-to-chord ratios of 0.083, 0.222, 0.333, and 0.444. The data exhibit a critical Reynolds number, much as a cylinder does, the value of which is about that of a cylinder alone (4×10^5, based on boom diameter). Lift and drag data for Reynolds numbers of about 1.4×10^5 and 4.9×10^5 were taken to be representative of subcritical and supercritical Reynolds numbers, respectively, and are shown in figures 6 and 7, together with the flat-plate data of figure 3. The lift data at small d/c (figs. 6(a) and 7(a)) are very similar for both Reynolds numbers and indicate a loss in lift coefficient at a given angle of attack due to the addition of the booms. There is a much greater effect of d/c on lift for subcritical than for supercritical Reynolds number. The drag data (figs. 6(b) and 7(b)) are quite different for the two Reynolds numbers. Generally, the minimum drag coefficients are less for the supercritical case. In particular, at high angles of attack, the supercritical drag coefficient is less than that of the flat plate, whereas for the subcritical Reynolds number, the drag coefficient is higher than that of the flat plate. It appears that the leading-edge booms act to delay leading-edge separation for supercritical Reynolds numbers but not for subcritical Reynolds numbers.

These data were used as follows. The model flexible wing data used for comparison purposes correspond to the subcritical Reynolds number case. Thus, the data of figure 6 were used in the analytical leading-edge boom investigation. Lift and drag increments due to the leading edge were formed by taking the difference between the flat-plate values ($d/c = 0$) and the values at the various d/c ratios. The results are sets of curves of Δc_ℓ and Δc_d versus α and d/c. The leading-edge booms were considered to have a local effect on the flow near the (swept) leading edge. Consequently, sweep theory was used in applying the section

data to a parawing calculation.[4] In order to use the section data, it was necessary to define a chord and an angle of attack. Using sweep theory, the local chord may terminate directly at the trailing edge or may intersect the keel before terminating at the trailing edge of the opposite wing panel. In this latter case the chord line was taken as the distance from the leading edge to the keel. The angle of attack in a plane normal to the leading edge may be considered as the angle between the local flow direction and either the chord or the tangent to the leading edge of the analytical canopy shape, as shown below.

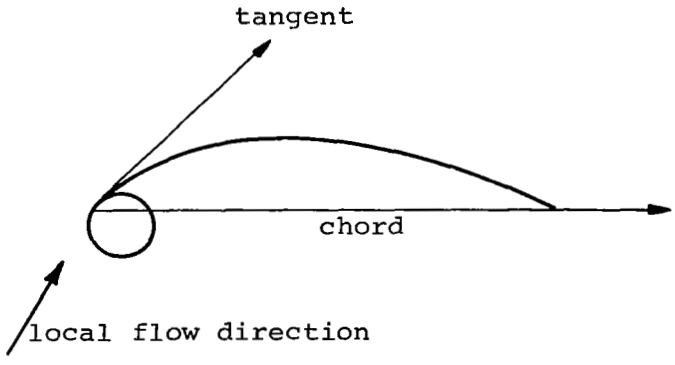

Both cases were considered in the calculations. The local flow direction was obtained from the Weissinger section-lift coefficient, a lift-curve slope of 2π, the section twist angle and angle of zero lift, and the leading-edge sweep angle. It should be noted that this approach does not permit any effect of chordwise downwash variation (induced camber) to be included. The resulting incremental lift and drag coefficients were resolved into a free-stream axis system and integrated over the span to get wing coefficients, which were then added to the basic canopy coefficients.

Iterative Nonlinear Lift Prediction Method

An aerodynamic prediction method was developed to attempt to account for nonlinearities in lift. The approach used is a combination of certain

[4]The use of sweep theory for subcritical flow over a swept cylindrical leading edge is suggested by the results of reference 17 for a yawed infinite cylinder, which tend to indicate that the "normal" drag coefficient based on velocity and force normal to the cylinder is constant with sweep angle.

features of the Weissinger method and strip theory. The resulting method is applicable to any wing for which section data are available. The results of the method agree with those of Weissinger-Pankhurst in the linear range of wing lift. However, it became apparent that additional work would be required to produce reasonable agreement with data in the nonlinear lift range, and this work could not be carried out within the scope of the investigation. The method is discussed herein to indicate the approach. Results are presented in a subsequent section.

For an initially assumed angle of attack distribution along the semispan (obtained from a Weissinger-Pankhurst solution), section data (for instance, figs. 5(a) and (b)) were used to determine the lift normal to the local angle of attack. This lift was resolved into lift relative to the free-stream direction, and the span loading was determined. The Weissinger theory was then used to determine the downwash at the three-quarter chord due to the known span loading which, together with the local section characteristics, allowed the local flow angle to be determined. This new angle of attack distribution was used and the process repeated until convergence was obtained. The profile drag was then obtained by the c_ℓ-method, as described in the previous section.

Luffing Boundary

Luffing occurs on a flexible parawing when the wing angle of attack is reduced to the point where, at some spanwise station, the leading-edge suction goes to zero, and the section lift is produced by camber alone. Zero suction corresponds to the condition where the stagnation point moves from the lower surface to the leading edge. Since the canopy aerodynamic analysis yields information on section lift along the span, an analysis was undertaken to predict the luffing angle from the Weissinger results. Three approaches for estimating the luffing boundary were investigated.

In the first approach, the slender-wing luffing criterion developed in reference 2 for triangular two-lobed parawings was used. This analysis, which neglects leading-edge booms, consists of determining a value of a canopy tension parameter for no leading-edge suction, with which is associated an unique value of the slackness parameter. Thus,

$$\frac{\ell' - 2s}{2s} = 0.6744 \left(\frac{\sin \alpha_{luff}}{\tan 2\theta}\right)^2 \tag{9}$$

From equation (9), the luffing angle, α_{luff} can be determined for a parawing of arbitrary planform, provided the slackness ratio is calculated in a cross-flow plane. The theory implies that all stations along the leading edge luff simultaneously for a conical lobe whether the trailing edge is swept forward or not.

In the second approach, the Weissinger results were examined to find the wing angle of attack for which zero leading-edge suction occurs anywhere along the span. Typically, as α is reduced, the lift coefficient at the tip station ($\eta = 0.924$) goes negative first. The angle of zero lift of the tip station was computed using the Pankhurst method, as previously described. The section lift coefficient corresponding to the condition for which all section lift is due to camber was computed as the product of the section angle of zero lift and the section lift-curve slope, 2π. The results for the local section lift coefficient calculated by the Weissinger method were then examined to find the wing angle for which this tip section lift coefficient occurs.

The third approach is based on the result that the Weissinger method gives good agreement on gross wing aerodynamic characteristics for conditions where the local section lift coefficients are known not to be accurately predicted. The method consists essentially of computing an "average" wing-lift coefficient for zero leading-edge suction. The local section lift coefficients for zero leading-edge suction were computed, as in the second approach above, for the stations along the span. These were integrated over the span using the quadrature formula, equation (A-15) of reference 9, to get an "average" wing lift coefficient for zero leading-edge suction, $(C_L)_{luff}$. Thus,

$$\left(C_L\right)_{luff} = \frac{\pi A}{m + 1} \left[\left(G_o\right)_{(m+1)/2} + 2 \sum_{\nu=1}^{(m-1)/2} \left(G_o\right)_\nu \sin \phi_\nu\right] \tag{10}$$

The wing luffing angle was then computed as the sum of the wing angle of zero lift and an angle given by $(C_L)_{luff}/2\pi$.

RESULTS

Accuracy of Lifting-Surface Methods

The accuracy of the results calculated by the Weissinger method were evaluated in two ways. The 7-point Weissinger results were compared with 15-point Weissinger results and with Multhopp results for a range of wing configurations. For the comparisons with the Weissinger method using different numbers of control points, 7-point solutions were calculated for several wings for which 15-point solutions were available from reference 18. The wings selected for the comparison were Nos. 421, 521, 621, 531, and 631 of reference 18, all of which have zero taper ratio. Their characteristics are shown in the following table:

Wing No.	421	521	621	531	631
A	3	3	3	6	6
$\Lambda_{1/4}$	30°	45°	60°	45°	60°

The solutions were compared for no camber and twist, and for no camber and a linear twist distribution having a maximum twist at the tip of one radian. The values compared were lift-curve slope, induced drag, and spanwise center of pressure. With the exception of the results for Wing No. 631, all values agreed to within 1 percent. For Wing No. 631, which represents an extreme case from a parawing standpoint, the 7-point lift-curve slope was low by 1.4 percent, the induced-drag coefficient was low by 6 percent, and the spanwise center of pressure was high by 1 percent. Span loadings were also compared. For all wings, the planar wing span loading differences were within the accuracy with which the curves of reference 18 can be read. The twisted-wing span loadings showed comparable accuracy outboard. At the root, the span loadings from the 7-point solutions ranged from about 2 to 10 percent lower than those from the 15-point solution for the highly-swept arrow wings which are lightly loaded at the root. On the basis of these results, the use of 7 spanwise control points in the Weissinger method is considered satisfactory for the parawing calculations of this study.

The differences between the calculated aerodynamic parameters from the Weissinger and Multhopp theories will be termed "chordwise effects"

for reasons which will now be explained. The Weissinger method represents the chordwise loading by one bound vortex and satisfies the normal flow boundary condition at one point per chord, the three-quarter chord point. The Multhopp method can represent the chordwise loading by several Fourier components of bound vorticity and at the same time satisfy the boundary condition at several chordwise positions. As such, it accounts simultaneously for chordwise variations in induced downwash and loading. The chordwise variation of induced downwash produces a curved streamline flow over the chord length which, on the basis of linear theory, is equivalent to a cambering of the airfoil in a uniform flow. The term "induced camber" is used to describe this effect, which is important at low aspect ratios where the wing chord is not small compared to the span of the trailing vortices. The term "chordwise loading" is used to denote the loading due to geometric camber. Since this loading is concentrated near the half chord rather than the quarter chord, its effect is important for conical parawings of high slackness, where a substantial fraction of the total lift is due to camber, regardless of aspect ratio.

Seven-point Weissinger results were compared with Multhopp results for a number of wings in order to verify the accuracy of the Weissinger-Pankhurst calculation method and to evaluate chordwise effects neglected in the Weissinger method. The results and discussion are presented in Appendix B. It was found that the Weissinger calculations agreed very closely with the Multhopp calculations made using 7 spanwise stations and 1 chordwise control point per station, a result which verifies the correctness of the Weissinger method. For a wide range of aspect ratios, slackness, and planform shapes, the Weissinger results for lift-curve slope, induced drag, and center of pressure agreed very well with Multhopp results obtained using 6 chordwise and 21 spanwise control points. For the quantities α_o, C_{m_o}, and C_{m_α}, significant differences between Weissinger and Multhopp results were obtained in some cases because of chordwise effects. Induced camber and chordwise loading effects are both significant for α_o. At low aspect ratios, where induced camber effects are important, the Weissinger method overpredicts α_o by as much as 4° for an aspect ratio of 1 and $2\beta = 149^o$. For high slackness, where chordwise loading effects are important, the Weissinger method underpredicts α_o. The chordwise loading effect becomes significant for $2\beta > 120^o$. For C_{m_o}, systematic differences also exist. The differences

can be as large as 0.01 to 0.02 for wings of this study. For C_{m_α}, the differences for a given planform are greatest at low aspect ratio. For the wings of this study with aspect ratios of 2 to 3, the differences in C_{m_α} are as large as 0.02.

On the basis of these comparisons, it was concluded that the 7-point Weissinger method can be used for parawings with aspect ratio greater than 2, which is the range of interest, to predict C_{L_α}, C_{D_i}, and center of pressure with good accuracy. The values of α_o, C_{m_o}, and C_{m_α} are less well predicted. Nevertheless, the Weissinger-Pankhurst values are used in the prediction method and the comparisons with data of this report for reasons which are discussed in a subsequent section.

Canopy Shape Studies

Two methods have been used to specify canopy shape in past work: the slender-body theory of reference 2 which accounts for canopy flexibility, and the method of reference 5 based on assuming the lobes of the canopy to lie on right-circular cones. The sensitivity of the calculated parawing aerodynamic characteristics to canopy shape can be assessed by applying the Weissinger method to shapes calculated by both methods. Since the slender-body theory of reference 2 is applicable only to triangular parawings, a triangular wing of aspect ratio 4 was used for the comparisons. The canopy shape computed by the right-circular cone technique of Appendix A assumes that the trailing-edge is straight in the uninflated state, so that a straight trailing edge is not obtained in the inflated state. It is nevertheless easy to construct an inflated wing with a triangular planform using Appendix A since all lateral cross sections are similar in the right-circular cone techniques.

Slender-body trailing-edge shapes were computed for the aspect ratio 4 triangular wing for two values of tension parameter; one value at the theoretical luffing boundary ($\lambda = 0.21$), and the second at a high lift condition ($\lambda = 1.0$). The trailing edge from the right-circular-cone method was calculated for the same slackness ratio. These trailing-edge shapes are shown in figure 8. Since the largest differences in shape between the cone method and slender-body theory occur when $\lambda = 1.0$, the aerodynamic characteristics of these two wings were compared on the basis of the Weissinger method. The calculated results indicated that the difference between the two shapes has very little effect on the aerodynamic

characteristics. The predicted angles of zero lift for the canopies are different by 0.2° or approximately 1 percent. The predicted moment at zero wing lift for both canopies agree within 10 percent. Since the planforms are identical, lift-curve slope and moment-curve slope are the same for both wings.

It is possible to show the effect of the shape assumption on induced drag in a simple way. On the basis of the results of reference 2, the induced drag of two-lobed triangular parawings can be correlated by the dimensionless parameters

$$\frac{C_{D_i}}{\tan^3\epsilon\left(\frac{\ell' - 2s}{2s}\right)} \quad \text{and} \quad \frac{C_L}{\tan^2\epsilon\sqrt{\frac{\ell' - 2s}{2s}}}$$

for any aspect ratio or slackness ratio. The theoretical curve from slender-body theory is shown in figure 9. The induced drags calculated by the Weissinger theory for several triangular wings whose shape is given by the right-circular-cone method are also shown in figure 9. These results agree very well with the slender-body curve; therefore, it was concluded that the induced drag from the Weissinger method for the triangular wings with shapes obtained by the cone method is virtually the same as the induced drag from slender-body theory for wings of the same aspect ratio and slackness ratio. For this correlation the slackness parameter was evaluated in a plane normal to the root chord.

Based on systematic calculations from the Weissinger method, a correlation similar to that for triangular wings in figure 9 is shown in figure 10 for NASA planforms. The results show that for a fixed aspect ratio, all slackness ratios fall on a single curve. The slender-body theory result for triangular planforms is shown on the same figure for comparison. Since the NASA planform approaches a triangular planform as aspect ratio decreases, the correlation curves for NASA planforms with low aspect ratio approach the slender-body theory.

Comparison Between Experiment and Theory for Rigid Wings

Systematic data available.- Systematic data are available for a series of rigid wings with 50° swept leading edges and canopy surfaces

formed from right-circular cones.[5] These data consist of lift, drag, and pitching moment over a large angle of attack range as well as photographs of tuft surveys. Since the wing shapes are known exactly and since there are no leading-edge booms, these data were taken to represent the aerodynamic characteristics of the basic canopy. The geometric characteristics of the wings are presented in table I.

Lift.- The lift data for the rigid wings are compared with the Weissinger theory in figures 11, 12, and 13. The theoretical results for the angle of zero lift and the lift-curve slope are in good agreement with the data in every case. The linear range for the wing is shown on all of the figures. With reference to figure 5(a) the wing linear range is exceeded when at any spanwise station the local angle of attack calculated from equation (6) exceeds $\pm 8^{\circ}$.

Agreement with experiment is good both inside and outside the linear range and even on wings without a linear range; for example, Wings No. 1 and No. 2 as shown in figures 11(a) and (b). The good agreement of predicted gross wing-lift coefficient is surprising in view of the fact that the Weissinger theory often predicts local lift coefficients greater than 2.0 in the range of good agreement.

The iterative nonlinear lift prediction method using the section data of figure 5(a) was applied to the rigid wings. The results for the aspect ratio 3 and 4 wings are shown in figures 14 and 15. For the flat wings (figs. 14(b) and 15(b)), the predicted and measured lift values agree very well. For the cambered and twisted wings, the lift-curve slope is predicted very well, but the angle of zero lift is high by about 2°. The agreement outside the linear range is as good as that within the linear range. However, the data do not show sufficient nonlinear behavior to serve as a good check on the method. The trend, however, is indicated by the upper end of the curve of figure 14. The predicted curve tends to break rather sharply when one section stalls. This break is due to the small number of semispan stations (4) used in the method, which results in a large influence of stall at one station on

[5]These data are unpublished results obtained from the Langley Research Center, NASA. The rigid wings have the same planforms and slackness ratios as the flexible wings of reference 19. Reference is made frequently to these data in the following text and the figures. Such reference will be denoted by the term "rigid wing data."

wing lift. No attempt was made to increase the number of span stations in the method, which was dropped in favor of the Weissinger-Pankhurst method.

It was noted in connection with the discussion of the section data of figure 5(a) that not all the lift due to camber is developed experimentally. Since the lift results of the iterative method are low, as noted above, the cambered section data of figure 5(a) were shifted upward until their α_o values matched those predicted by Pankhurst, and the shifted section data were used in the iterative method. In this case, the lift results for the cambered and twisted wings of figures 14(a) and 15(a) agreed exactly with Weissinger results for the linear range, as would be expected. The agreement serves as a check on the iterative method.

Drag.- The α- and c_ℓ-methods for profile-drag prediction were applied to all of the rigid wings. The results are shown in figures 11, 12, and 13. The total drag is obtained as the sum of the profile drag and the induced drag computed using the Weissinger method. For the total drag obtained using the α-method, the agreement is poor for the highly cambered and twisted wings having no linear range of lift coefficient (figs. 11(a) and (b)). For the remaining rigid wings, the α-method slightly underpredicts profile drag at the lower end of the linear range, where maximum lift-drag ratio occurs, and considerably underpredicts the profile drag at higher lift coefficients.

The photographs of the tuft studies in the rigid wing data give some indication of a reason for the discrepancy between theory and data at high lift coefficients. The photographs indicate extensive separation on the upper surface of the wings at high lift coefficients. If a prediction is being made in this region, the angle of attack determined from equation (6) will be low because the lift-curve slope (2π) is too high for separated flow over a section. Thus, the predicted value of section profile-drag coefficient will be low. For this reason, the α-method would be expected to underpredict wing drag at high lift coefficients.

With the c_ℓ-method, it was possible to predict stall. At the upper end of the theoretical drag curve is the symbol R to indicate root stall, the symbol T to indicate tip stall, or both symbols to indicate

simultaneous root and tip stall. The stall in this connection indicates that the local c_ℓ as obtained from the Weissinger method lies between the end of the linear range and the maximum lift coefficient. It was not possible to apply the c_ℓ-method for the wing with highest slackness (fig. 11(a)) because at any angle of attack some local lift coefficient exceeded the maximum (or minimum) lift coefficient from the section data.

In the linear range the c_ℓ-method yields about the same drag as the α-method, but outside the linear range it yields a higher drag. While this trend is in the right direction, the c_ℓ-method still underpredicts the measured drag in the nonlinear range. The accuracy of prediction increases as the aspect ratio and slackness ratio decrease. It is noted that tip stall is also associated with low aspect ratios and low slackness. Tip stall should cause less separation drag than root stall, since tip chords are small and the area subject to spanwise flow is less. Thus, the c_ℓ-method should be more accurate with tip stall than root stall.

The c_ℓ-method is based on local lift coefficients calculated from a linear lifting-surface theory and profile-drag coefficients from nonlinear section data. It thus does not account for any nonlinear effects on section-lift coefficient. Even though the Weissinger method predicts gross wing lift quite accurately under conditions of extensive flow separation, the local predicted lift coefficients under such conditions are sometimes much greater than the maximum lift coefficient of the airfoil section. Accordingly, it is probable that the section-lift coefficients are not accurately predicted by the Weissinger method near the stall. The nonlinear iterative lift prediction method was an attempt to account for nonlinear section-lift effects on the wing span loading in order to improve drag prediction. If further efforts result in a satisfactory nonlinear method, the prediction of drag by the c_ℓ-method should be improved.

The profile drag was computed by the Polhamus method (ref. 16) for the flat rigid wings of figures 11, 12, and 13. Combination with the Weissinger results for induced drag gives the predicted total drag, which is compared with experimental results in figure 16. The agreement is very good. The Polhamus method and the c_ℓ-method give drag results which are nearly identical for the linear range of lift coefficients.

In order to assess the effects of induced camber on drag, the Polhamus method was compared with both α- and c_ℓ-methods for flat NASA planform wings with varying aspect ratio. These results are shown in figure 17. At aspect ratios less than 2.0, the Polhamus method predicts higher profile-drag coefficients than do either the c_ℓ- or α-methods. This difference is attributed to induced camber. At aspect ratios of 2 or greater, all methods are in good agreement in the linear range. In the nonlinear range the c_ℓ-method predicts somewhat more drag than the Polhamus method. These comparisons with the Polhamus method are intended to illustrate the differences between a gross wing prediction method which includes induced camber and a strip-theory method which does not include induced camber. Improved accuracy of the Polhamus method might be obtained by adapting the method to account for variations due to camber across the span.

An estimate was made of the effect of Reynolds number on the profile-drag predictions. The cambered section data of reference 13 cover a Reynolds number range from 10^4 to 6×10^5, based on chord. Thus, the skin-friction portion of the section drag is primarily that for a laminar boundary layer. The Reynolds numbers for the model parawings used for comparison herein are of the order of 10^6, based on root chord. An estimate of the skin-friction drag was made for a rigid wing of aspect ratio 3. Flat-plate skin-friction laws for laminar and turbulent boundary layers were used with an assumed transition Reynolds number of 5×10^5. Reynolds number variations across the span were taken into account. The resulting skin-friction drag coefficient was approximately 30 percent of the minimum profile-drag coefficients or about 10 percent of the total drag at a lift coefficient of 0.4. Based on this result no corrections were made to the section drag data to account for variation of skin friction with Reynolds number.

Pitching moment.- The moment-curve slope, dC_m/dC_L, and the moment at zero wing lift of the equivalent uncambered and twisted wing were computed by the Weissinger method. The moment due to camber was computed from equation (3) and added to the above moment at zero lift to give the wing C_{m_o}. The results for the rigid wings are compared with experimental data in figures 11, 12, and 13.

Good agreement between theory and experiment is obtained on moment-curve slope for all the flat wings. These wings have C_{m_o} values of

zero. The agreement for the aspect ratio 3 and 4 cambered and twisted wings is also good for both moment-curve slope and C_{m_o}, although the predicted C_{m_o} value for the aspect ratio 4 wing is somewhat high. The agreement on $dC_m/d\alpha$ and C_{m_o} for the aspect ratio 5.45 cambered and twisted wings is poor except at low slackness ratios. It is probable that upper surface separation on the high aspect ratio wings is responsible in part for the disagreement.

At least four effects occur which are not reflected in the pitching-moment comparisons of figures 11, 12, and 13. Two are theoretical deficiencies of the Weissinger-Pankhurst method. First, incorporation of chordwise effects neglected by the Weissinger method tends to raise the predicted C_{m_o} and increase the magnitude of C_{m_α}, as shown in Appendix B. Second, incorporation of nonplanar effects in satisfying the wing boundary condition would probably change the moment predictions, although the direction of the changes is difficult to predict. The other two effects are viscous. The first is the aforementioned inability of highly-cambered sections to develop their predicted lift and moment. Incorporation of this effect would reduce the (negative) moment contribution due to camber, resulting in a higher predicted C_{m_o}. The second is the moment due to drag acting above the root chord plane. This effect was estimated to determine its significance. The moment due to drag was computed for several wings having 2β values of 103°, 131°, and 158°. At the lowest slackness, this moment is less than 10 percent of the moment due to camber and thus has a very small absolute value and a negligible contribution to the total moment. At the higher slackness values, the moment due to drag is an appreciable fraction of the moment due to camber and is thus large compared to the net Weissinger-Pankhurst C_{m_o}. Since the moment due to drag is positive, its incorporation would yield a higher predicted C_{m_o}. Consequently, three of the four effects just noted tend to increase the predicted moments over those given by the Weissinger-Pankhurst method.

The predicted moments for the cambered and twisted rigid wings either agree well with data (figs. 11(d) and 13(a)) or are high (figs. 11(a), 11(b), 11(c), and 12(a)). Thus, the moment effects just noted do not explain the differences in the data correlations, and it is apparent that the nonplanar influence or some unrecognized effect is compensating for the three effects noted to provide satisfactory agreement on moment

with the Weissinger-Pankhurst values for moderate aspect ratio. Consequently, these moment effects are not included in the moment predictions for flexible wings.

Effect of Leading-Edge Booms on Wing Characteristics

In comparing either the predicted Weissinger-Pankhurst canopy performance or rigid wing data with data for flexible wings, differences can be attributed not only to leading-edge booms but to other sources as well. One such source is change in canopy shape. The shape comparisons for low slackness indicated the predicted aerodynamic performance to be insensitive to the differences between the theoretical slender-body shape and the conical shape. However, no canopy shape measurements have been made at large slackness to check the conical shape assumption. Other sources of differences might include canopy weight, porosity, and seam effects; trailing-edge flutter; viscous effects; and nonplanar theoretical effects. It was felt, however, that leading-edge booms are the major source of differences, and for the sake of simplicity in the following discussion, the differences will be attributed to boom effects.

Analytical investigation.- The analytical investigation to determine the applicability of splitter-plate section data to a three-dimensional wing with leading-edge booms was carried out for a NASA planform wing with $\Lambda_o = 45^o$, $\Lambda = 50^o$, and a leading-edge boom of $d/c_r = 0.012$. For the case using the chord line as the reference direction for determining local angle of attack, the following results were obtained:

α	16°	22°	30°
ΔC_L	0.001	-0.034	-0.042
ΔC_D	.016	.004	.001

The incremental wing coefficients computed using the leading-edge tangent as the reference direction are similar in magnitude and sign to the above. The measured values of C_L and C_D for this wing (ref. 20) and the predicted values for the canopy using the Weissinger-Pankhurst method (without adjustment) are shown in figure 25(d).

The predicted incremental lift coefficients are negative at the higher α values, since the splitter-plate section data (fig. 6(a)) indicate a negative increment at positive α due to the addition of the leading edge. A comparison of the above values with the results of figure 25(d) indicates first that ΔC_L is less than half of the difference between measured and predicted values (without adjustment) and, second, that a negative increment is predicted whereas a positive increment is required to cause better agreement.

The incremental drag coefficients noted above are positive, in accordance with the splitter-plate data of figure 6(b). Furthermore, their magnitudes are of the same size as the difference between measured and predicted drag at moderate α. At high α, however, the predicted increment decreases, whereas the required increment for good agreement increases rapidly.

An interesting observation on the applicability of the splitter-plate drag data can be made on the basis of the comparison between rigid and flexible parawing data of figures 18 through 20. These data show that the flexible wing generally has a higher drag than the rigid wing (with no leading-edge booms) at moderate α but a lower drag at high α. It is very likely that the leading-edge booms act to increase the leading-edge radius and delay leading-edge separation on the flexible wings. Thus, it is apparent that three-dimensional booms act much like supercritical two-dimensional booms (fig. 7(b)), even though their Reynolds number is subcritical.

On the basis of these comparisons, it is evident that two-dimensional splitter-plate data are not applicable to the determination of three-dimensional boom effects in flexible parawings, although the data do provide some understanding of three-dimensional effects.

Empirical investigation.- The empirical investigation of leading-edge booms made use of data for both flexible and rigid wings and theory for the basic canopy. The data were taken from references 19, 20, and 21, and the rigid wing results. The quantities examined were α_o, $dC_L/d\alpha$, C_D, and $dC_m/d\alpha$.

Results for angle of zero lift of NASA wings with constant-diameter booms are shown in figure 21(a). The curves indicate difference between canopy theory and wing data for two sets of wings with different d/c_r

ratios and two different canopy attachment methods. These data are consistent in that the Weissinger method is indicated to yield too large an α_o by 2° to 4°. On the basis of these results, constant empirical adjustments of 2° to 4° were made to the theory for all subsequent comparisons with the wing-lift data of references 20 and 21, respectively. It should be noted that these adjustments probably contain not only the leading-edge boom effects but other effects as well.

Results for $\Delta\alpha_o$ for tapered leading-edge booms are shown in figure 21(b). Since data for only one boom size are available, the results are shown as a function of 2β. The results are consistent and show an increasing $\Delta\alpha_o$ with increasing 2β. The aspect ratio effect, shown by the variation in the values at $2\beta = 103^o$, is small.

Results for the ratio of experimental-to-theoretical lift-curve slope for NASA wings with constant-diameter leading-edge booms of two d/c_r ratios are shown in figure 22(a). There is no systematic boom effect in the results, and there is no direct manner in which any leading-edge effect can be extracted, since there are no comparable data for rigid wings of NASA planform. Since the deviations between experiment and theory are not systematic and generally lie within a ± 10 percent band for $2\beta < 180^o$, it does not appear that an adjustment to the Weissinger calculation for lift-curve slope is necessary for two-lobed parawings with constant-diameter leading-edge booms.

Results for the ratio of experimental-to-theoretical lift-curve slope for tapered leading-edge booms are shown in figure 22(b). Similar ratios for rigid wings are shown in order to assess the effect of the leading edge. The effect is systematic and serves to reduce the lift-curve slope by an amount which increases slightly with increasing slackness. The aspect ratio effect at a constant value of $2\beta = 103^o$ can be obtained by comparing the values for the aspect ratio 3 and 4 wings with values of $(\ell_o - \ell)/\ell$ of 0.113 and 0.085, respectively, with that of the aspect ratio 5.45 wing having $(\ell_o - \ell)/\ell = 0.054$. As is the case with $\Delta\alpha_o$, there is essentially no effect of aspect ratio.

The effect of canopy attachment method on lift for constant-diameter booms is illustrated in figure 23 for a NASA planform wing for which five sets of data are available. The significant effect on lift is a variation in α_o that is of the same magnitude as the change in α_o

due to the addition of the leading edge to the basic canopy, as shown in figure 21.

The possibility was investigated that an empirical adjustment could be made to drag to account for the presence of the leading-edge booms. No simple adjustment was found as for the angle of zero lift because of the more complicated influences of the leading-edge booms in this case. The effects of the booms can be seen directly from the data of figures 18, 19, and 20, which compare rigid-wing data with flexible-wing data for the same aspect ratio and slackness ratio. All of the flexible wings for the comparisons had tapered leading-edge booms. Almost without exception the flexible wings show lower rate of drag rise with lift coefficient than the corresponding rigid wings. As indicated previously, leading-edge booms tend to delay leading-edge separation at large angles of attack. The canopy attachment means are also significant, as shown in figure 23. The attachment means that have lowest drag at low α tend to have highest drag at high α.

With regard to pitching moment, the data of figures 18, 19, and 20 show a decrease in C_m for a given lift coefficient as a result of adding leading-edge booms. For wings which do not have very large slackness ratios, the slope dC_m/dC_L is not significantly changed. The addition of the leading-edge booms causes positive lift and negative moment for a given angle of attack. Thus, the main part of the lift is added behind the wing center of moments.

As a result of the comparisons noted above, the leading-edge boom effects were found to depend on the diameter-to-chord ratio, the taper of the leading edge, and the method of attachment of the canopy to the boom. Insufficient systematic data are available either to develop an analytical prediction method or to separate in an empirical fashion the influence of the various effects on wing performance. However, empirical correlations were obtained for angle of zero lift for the case of small, constant-diameter leading-edge booms with pocket attachment and for the case of large, constant-diameter leading-edge booms with front attachment. For the case of tapered leading-edge booms with front attachment, systematic empirical corrections were found for α_o and $dC_L/d\alpha$.

Comparison Between Experiment and Theory for Flexible Wings

Systematic data available.- The flexible wing data chosen to test the prediction methods are for two-lobed parawings with rigid leading-edge booms and rigid keel booms. The geometric characteristics of these parawings are presented in table II.

The first set of data (ref. 19) is for flexible wings having planforms identical to the rigid wings discussed previously. These wings have tapered rigid leading-edge booms with the canopy attached at the front of the boom. The second set of data (ref. 5) is for a conical parawing of aspect ratio 5.45. This high aspect ratio wing is identical to one of the wings from reference 19 and has tapered leading-edge booms with a front canopy attachment. The third set of data is for the triangular wings of reference 4. These wings have very low slackness ratios with front attachment and constant-diameter leading-edge booms. The most extensive and systematic data available for NASA planforms are those from reference 20. These data cover a wide range of aspect ratio and slackness ratio for constant leading-edge diameter booms using pocket canopy attachment. The effect of leading-edge diameter is studied as is the effect of canopy attachment method. The data of reference 21 for NASA planforms with constant aspect ratio and a wide range of slackness ratios are for parawings with large rigid leading-edge booms with front attachment.

It should be noted in the following discussion that differences between the flexible wing data and either rigid wing data or theory for the basic canopy were considered to be due primarily to leading-edge effects rather than to any effects due to departure of the flexible canopy from a conical surface. This position was adopted on the basis of the shape comparisons discussed previously. Some uncertainty still exists, however, concerning the effects of canopy shape, particularly for high slackness cases where data for shape comparisons are unavailable.

Lift.- In figures 18, 19, and 20 the flexible wing lift data from reference 19 are compared with the rigid wing data and the predicted results from the Weissinger method. The high-slackness, high-aspect-ratio wings which have no linear range exhibit some difference in angle of zero lift and lift-curve slope between the rigid and the flexible wings. At low lift coefficients above the luffing boundary, the leading

edge has the general effect of increasing the gross wing-lift coefficient at a given angle of attack. At low slackness ratio ($\Delta\Lambda \leq 5^{\circ}$) the lift-curve slope is approximately the same for both rigid and flexible wings for all aspect ratios. The deviations between experiment and theory for these wings have already been shown in figures 21(b) and 22(b) on a systematic basis.

The aspect ratio 5.45 flexible wing data from reference 5 are also shown in figure 18(c). The two flexible wings are identical and the lift curves are closely the same. However, the flexible wings exhibited less separated flow than the rigid wing without leading-edge booms. For an angle of attack where the rigid wing exhibited general separation with reversed flow over the rear of the wing, the tuft photographs of the flexible wing exhibited strong spanwise flow but no reversed flow.

The aerodynamic characteristics of the flexible triangular parawings of reference 4 are shown in figure 24 together with the Weissinger results. For these wings, which have constant-diameter leading edges, the Weissinger method without any correction for leading-edge booms gives good lift prediction. It is noted that these wings are of very low slackness ratio and use front attachment of the canopy to the booms.

The NASA planform data of reference 20 are shown in figure 25 for all the wings which have values of 2β less than 180° for the theoretical conical canopy. The predicted lift is shown for the Weissinger method with and without the empirical leading-edge adjustment for α_o from figure 21(a). The single adjustment of 2° works well for all the wings of figure 25.

Data from reference 21 for NASA planform parawings with large-diameter leading-edge booms are shown in figure 26. Again the Weissinger method with and without the empirical leading-edge correction is shown. As before, the single correction works well for all wings.

Drag.- Drag comparisons between theory and experiment can be made for four groups of flexible wings to deduce the effects of various sizes and types of leading edges and methods of canopy attachment. Comparison can also be made between data for wings with and without leading-edge booms to show the experimental boom effects on drag.

A significant factor in drag comparisons is the difference between methods for correcting the data for tare drag. In some cases, tare

measurements were made with the spreader bar and balance housing in the free stream while in others, tare measurements were made with the spreader bar and housing in the presence of a cylindrical canopy. Any effect of the spreader bar on the wing has been neglected in experimental evaluation of the tares. Also, differences between the influence of cylindrical and conical canopies on tares are not available. These comments indicate the difficulties that arise and care that must be taken to obtain accurate drag data for use in evaluating a prediction method.

For the wings of table II corresponding to references 4, 5, and 19, the drag data as presented include a correction for the drag tare due to the spreader bar. For the wings of references 20 and 21, the drag data contain no allowance for spreader-bar drag tares. Accordingly, a theoretical spreader-bar drag correction was applied to the latter sets of data on the assumption that the spreader bar is a cylinder in subcritical normal flow with a drag coefficient of 1.2. Data are available on the drag of a parawing with and without a spreader bar (ref. 21). The measured spreader-bar drag tare was approximately constant for all angles of attack, but it was only about 70 percent of the theoretical spreader-bar drag. The full theoretical spreader-bar drag tares were found to check measurements of the tare presented in reference 4. It was decided to apply the full tare corrections to the data of references 20 and 21.

In figures 18, 19, and 20, the rigid wing data are compared with corresponding flexible wing data from reference 19 and with theory for the basic canopy. At low lift coefficients, the flexible wing drag is higher than both the rigid wing data and theory, which is in accord with the results shown by the splitter-plate data. At high lift coefficients, the flexible wing drag is lower than the rigid wing data. Thus, the addition of a leading-edge member tends to delay separation on the wing at high angles of attack. These results are for tapered leading-edge booms and front canopy attachment.

Drag comparisons between measured values and predicted values using both the α- and c_ℓ-methods are shown in figure 24 for triangular flexible wings with constant-diameter leading-edge booms and front canopy attachment. In this case the data are slightly above the theory in the linear range. The c_ℓ-method does not extend far into the nonlinear range because of tip stall and is still in good agreement with experiment. The α-method lies under the experiment at high angles of attack.

The experimental drag data for the NASA planform parawings of reference 20 are compared with predicted results in figure 25. These wings have constant-diameter leading edges and a pocket canopy attachment; therefore, the leading edge has a fairing on the top and bottom surfaces. The experimental drag lies slightly above the theoretical drag over most of the linear range. At the upper end of the linear range and in the nonlinear range, the data usually lie well above the α-method prediction. In this region, the c_ℓ-method prediction is slightly below the experimental drag for moderate leading-edge sweep angles (40° to 50°), but the tendency to underpredict increases with leading-edge sweep angle. The tendency of the c_ℓ-method to underpredict is thought to be caused by the same effect as for the rigid wings: a region of separation which cannot be predicted.

The type of stall (tip or root) has been indicated on the curves of figure 25. Systematic examination of the type of stall shows root stall to be associated with high aspect ratio and high slackness ratios just as in the case of the rigid wings.

In figure 25(g) the appearance of tip stall at $C_L = 0.93$ in the c_ℓ-method drag curve occurs well within the linear range, as noted on the upper part of the figure. The upper limit of the linear range ($C_L = 1.05$) is found from the Weissinger method assuming that the limit occurs when the local angle of attack corrected for upwash exceeds 8° regardless of camber. In the Weissinger method as used herein, the Pankhurst method is used to predict the angle of zero lift due to camber, and it is known that the Pankhurst method overpredicts the camber effect for large cambers. If a prediction of the linear range is made using section-lift coefficient (i.e., fig. 5(a)) rather than angle of attack, a wing-lift coefficient of 0.92 is found as the upper limit of the linear range.

Drag results for NASA planform parawings with large, constant-diameter leading-edge booms and front attachment are shown in figure 26. The data are from reference 21. Both the c_ℓ-method and the α-method predicted values are shown and agree with each other in the linear range. The measured drag is considerably higher than values predicted for the basic canopy at high slackness but is of the same order for low slackness. The delay of wing separation at high lift coefficients due to the presence of the leading edge is evident from the measured results, which

behave more like the α-method predictions than the c_ℓ-method predictions. The experimental spreader-bar drag on these wings is approximately 30 percent smaller than the theoretical correction; however, for the worst case (fig. 26(e)), the resulting uncertainty in the theoretical correction for spreader-bar tares is about 10 percent of the minimum drag of the wing.

The results of these four sets of comparisons indicate that the leading edge generally increases the drag over that of the basic canopy at moderate lift coefficients. The increment is small for small leading edges and pocket attachments, and increases with d/c_r ratio. The presence of the leading edge delays wing flow separation to higher lift coefficients such that at high lift coefficients the drag of the parawing with leading-edge booms is lower than the canopy drag without leading-edge booms.

Pitching moment.- The wing pitching-moment coefficients for flexible and rigid wings of aspect ratios 5.45, 4, and 3, and various slacknesses are shown in figures 18, 19, and 20, respectively. A comparison of the differences between the rigid and flexible wing data in the linear range indicates that generally the moment-curve slope is not changed greatly by the addition of the leading-edge booms, but that a fairly constant negative increment between 0.035 to 0.045 is added by the booms to the moment curve for each wing. An exception to this case occurs in figure 18(d) where a nonlinear effect arises before the end of the linear range. Outside the linear range the comparisons are influenced by separation to which pitching moments are very sensitive. No systematic differences between the pitching-moment curves of the rigid and flexible wings were noticed in the nonlinear range.

Since the theory predicts the moment curve for the basic canopy with good accuracy in the linear range (except for fig. 18(c)) the negative moment increments noted above should be applicable as a simple adjustment to the theory. Thus, it is possible to adjust the prediction method to include boom effects by applying a negative increment of 0.035 to 0.045 to the moment curve in the linear range. This correction would be applicable to small, tapered leading-edge booms with canopy attachment at the front of the boom.

Pitching-moment results for the flexible NASA planform parawings with small leading-edge booms of constant diameter are shown in figure 25. Figures 25(a), (b), and (c) for the $\Lambda_o = 35^o$ series show that in the linear range the effect of the leading-edge booms is to decrease C_m by a nearly constant amount ranging from 0.015 to 0.020. Just the opposite effect is shown for the $\Lambda_o = 45^o$ series in figures 25(d) and (e) where C_m is increased by about 0.007 to 0.010. For the $\Lambda_o = 55^o$ series, figures 25(f) and (g) show both positive and negative increments in C_m. These experimental deviations between experiment and the canopy theory can be used as adjustments to the theory even though they are not as systematic as those for the tapered booms.

Pitching-moment results for the flexible NASA-planform parawings with large-diameter leading-edge booms are shown in figure 26. By comparison with theory, it appears that the large-diameter booms cause large negative contributions to C_{m_o} and also change the magnitude of dC_m/dC_L. Thus, a simple ΔC_m correction for the large booms cannot be made as for the small booms.

Luffing boundary.- The theoretical methods for predicting the luffing boundary can be evaluated using data from reference 20. The experimental luffing angle is taken as the lowest wing angle of attack for which lift data are presented and may contain some uncertainty. The data are for wings with a leading-edge diameter of 0.015 of the root chord and pocket canopy attachment.

The comparisons between the predicted and experimental luffing angles of attack are shown in figure 27. The solid lines show the slender-body predictions. For the lowest aspect ratio ($\Lambda_o = 55^o$) and low slackness, which conditions are most consistent with the assumptions of the theory, the agreement is good. Otherwise, the method considerably overpredicts measured results.

The results for the second approach, zero leading-edge suction at the tip station, are shown by the long dash curves. This method consistently overpredicts the measured luffing angles for all aspect ratios and slackness. Part of the difference can be attributed to neglect of leading-edge booms in predicting the luffing boundary. For a given lift coefficient, the predicted angle of attack for the basic canopy exceeds by about 2° the values measured for the flexible wings. The differences

in figure 27 are considerably greater than 2°, however, and cannot account for the difference between theory and experiment. For wing angles equal to the measured luffing angle, the Weissinger method indicates that the outboard quarter semispan is operating at a negative lift coefficient. The reason for this result is not apparent, except that the Weissinger method may not be accurate at the wing tip for the extreme twist distributions typical of conical parawings with large slackness.

The third approach is presented as an engineering prediction method. The short dashed curves indicate zero average leading-edge suction and are seen to give reasonably good agreement with the data. The difference is largest for the lowest aspect ratio wing, where the method predicts too low a luffing angle by about 2° to 3°.

Limitations of the Theoretical Methods

Slackness ratio.- Since the assumption is made that the flexible canopies in the inflated state lie on the surface of a right-circular cone, the shape-calculation procedure is limited to canopies that are half-cone ($2\beta = 180^{\circ}$) or less. The slackness ratio of canopies wrapped about a half-cone varies with planform shape; however, for NASA planforms the upper limit of slackness ratio is approximately 0.45 for all aspect ratios. Above this value the canopy must have some shape other than part of a circular cone.

As the slackness ratio increases, the parawing becomes more nonplanar. Since the Weissinger theory is based on a planar wing, the question arises as to how far the parawing can depart from a planar configuration and still be within the range of the Weissinger method. To shed light on this question, the ratio of experimental to theoretical lift-curve slopes are compared in figure 22 as a function of slackness ratio. For slackness ratios less than 0.45, the agreement for the NASA planforms shown in figure 22(a) is within ± 10 percent with one exception. It is noted that the use of the true chord rather than the projected planform chord tends to increase the theoretical value of $dC_L/d\alpha$ and helps in the correlation. For slackness ratios greater than 0.45, the theory considerably underpredicts the measured lift-curve slope.

As slackness ratio increases, camber and twist also increase. A NASA planform near a slackness ratio of 0.45 may have the tip twisted

70° with respect to the root chord. Lifting-surface theories would not be expected to give reliable results for such extreme twist distributions because the local sections are operating in the nonlinear angle of attack range. It is nonetheless noteworthy that the theoretical lift-curve slopes and angles of zero lift are in good agreement with experiment for these extreme cases.

Section data.- One of the basic difficulties encountered in developing the present prediction methods is the shortage of appropriate section data. The section profile-drag data used for basic canopy drag prediction are a combination of two-dimensional data for sharp-edged, flat plates and data for a rectangular wing of aspect ratio 5 and a round-edge circular-arc section. There are no other data to indicate trends or accuracy of the data used. In particular, there are no other data to verify the loss of lift and moment at high camber on thin plates indicated by the data of reference 15. Furthermore, there are no measurements of flexible canopy section shapes for high-slackness parawings to indicate the accuracy of the circular-arc camberline assumption used in the profile-drag calculation. For prediction of leading-edge boom effects, there is a lack of data on sections with cylindrical leading edges with various attachment means of the section to the cylinder, various cambers of the section, and various sweep angles. Such data would lead to better understanding of boom effects.

Linear lift coefficient range.- Each wing with moderate slackness has a certain range of angle of attack over which the entire wing can operate with local section-lift coefficients inside the linear range for the airfoil section. Inside the linear range for the wing, the profile-drag coefficient and other quantities can be computed with some degree of confidence from section data. Outside the linear range, local lift coefficients exceeding the maximum lift coefficient of the section are predicted by either the Weissinger or Multhopp theories and make strip profile-drag calculations unrealistic. A lifting-surface theory using nonlinear section data and yielding local lift coefficients not exceeding the maximum lift coefficient of the airfoil section could be useful in extending this limitation of the current method.

Viscous effects.- Viscous effects are generally neglected in the methods described herein, except for the computation of profile drag. Their effects and/or their limitations on the methods are important to

recognize, however. First, the photographs of the tuft study in the rigid wing data indicate that all of the twisted and cambered wings have some spanwise flow near the upper end of the linear range and ultimately separation at high angles of attack. Present prospects for an aerodynamic prediction method to account for these phenomena are not good. However, linear methods based on section data give an indication of separation, and a nonlinear method should provide some prediction capability for conditions of small separated regions. It is noted that the maximum lift-drag ratio falls within the linear region and should be predictable with a linear theory.

It was noted that the camber data of reference 15 indicate that highly cambered sections do not achieve all of their predicted lift and moment because of viscous effects. Nevertheless, the Weissinger-Pankhurst method, which utilizes theoretical camber lift and moment increments, agrees very well with rigid wing data (figs. 12 and 13), at all slackness ratios. In this case, a better prediction method is obtained by neglecting these viscous effects on camber lift and moment because of other compensating effects also neglected.

On parawings having high twist and camber, a drag force considered to act at the section center of pressure can cause an appreciable nose-up moment, as noted previously. To the extent that part of the drag (profile drag) is due to viscous effects, this moment is a viscous effect. Incorporation of this effect into the moment predictions for wings where the effect is significant ($2\beta > 103^{\circ}$) would cause the agreement to be worse (figs. 11(a) and (b)), since the Weissinger-Pankhurst moment overpredicts data without consideration of moment due to drag.

CONCLUDING REMARKS

Various methods of predicting the aerodynamic performance of two-lobed conical parawings were compared with each other and with experimental data in an effort to determine the best prediction means. Several methods were investigated for determining canopy shape, for calculating the basic canopy theoretical aerodynamic characteristics, for estimating the profile drag of the canopy, and for estimating its luffing boundary. The effect on the basic canopy of the addition of leading-edge booms was also studied.

There exist two means for estimating the canopy shape of a parawing: the slender-body theory of reference 2 and the assumption of reference 5 that the lobes of the canopy can be formed from the surface of a right-circular cone. Comparison of the cross-sectional shapes of two-lobed parawings of moderate slackness obtained from the two methods show slight deviations between the two. The differences in the predicted aerodynamic characteristics by the Weissinger method due to these deviations are negligible.

The canopy lift, moment, and induced drag without leading-edge booms can be predicted by the Multhopp method or a combined Weissinger-Pankhurst method. Comparisons of calculated wing characteristics based on these methods showed that the 7-point Weissinger method combined with the Pankhurst method to approximate camber effects gives sufficiently accurate results for wings of NASA planform except in certain special cases. These special cases involve the moment-curve slope C_{m_α}, the wing angle of zero lift α_o, and the wing moment at zero lift C_{m_o}. The value of C_{m_α} is predicted to within 0.02 for aspect ratios greater than 2. The α_o value is well predicted for 2β less than 120°. For larger 2β, the α_o value is lower than the Multhopp value by an amount which increases with increasing aspect ratio. The values of C_{m_o} are consistently underpredicted by amounts up to about 0.02, with the largest differences occurring for high slackness and low aspect ratio. The major source of difference between the two methods is attributed to chordwise variations of induced downwash and loading.

Several methods were investigated for estimating wing profile drag from section data. Strip-theory methods include an α-method, based on the use of estimated local section angles of attack, and a c_ℓ-method, based on the use of local section-lift coefficients. In addition, a gross method of Polhamus for flat swept wings was used which accounts for induced camber. For flat rigid parawing models without leading-edge booms, all three methods were in good agreement for aspect ratios of 3 or greater, which indicates that induced-camber effects are negligible in this range. For aspect ratios of 0.5 and 1.0 the Polhamus method predicted a larger drag due to significant induced-camber effects.

The ability of the lifting-surface and profile-drag methods to predict parawing aerodynamic characteristics without boom effects were evaluated from data for a series of nine rigid parawings of known shape.

The lift curves were accurately predicted for all wings even though the predicted section-lift coefficients exceeded the maximum section-lift coefficient at all wing angles of attack in one case. For the range of wing angle of attack in which the section-lift coefficients were within the linear range, good agreement was obtained between the predicted and experimental moment curves. Both the α- and c_ℓ-method combined with the Weissinger method tend to underpredict total drag in this linear range. Outside the linear range the c_ℓ-method predicts the drag better than the α-method but both underpredict the drag at higher lift coefficients.

It is noted that a number of effects occur which are not predicted by the Weissinger-Pankhurst method. From the standpoint of using the Weissinger-Pankhurst method as a prediction technique, no correction for these effects should be included for best results because the effects tend either to offset one another or to offset some effect which has not been recognized or estimated properly. Included in these effects are the difference between predicted and actual lift and moment developed by camber, the moment due to drag for highly-cambered and twisted wings, chordwise effects on α_o and C_{m_o}, and nonplanar lifting-surface effects.

The investigation of the effect of leading-edge booms on parawing aerodynamic performance indicated that the lift increment added to the canopy by the booms is much larger and of opposite sign to that predicted using section data. The drag increment added is somewhat larger and of the same sign as that predicted with section data. The force and moment increments depend on ratio of boom diameter to root chord, method of canopy attachment, and boom taper. For wings of NASA planform with tapered booms and top attachment, the addition of the booms affects both lift-curve slope and α_o. The boom addition causes an increase in drag at low lift coefficient and a decrease in drag at high lift coefficient The latter is associated with a delay in leading-edge separation due to increased leading-edge radius, which is characteristic of supercritical splitter-plate section data but not subcritical data, to which the model Reynolds number corresponds.

For NASA planforms with small booms of constant diameter and pocket attachment, it was found that the boom causes a parallel shift of the lift curve for all angles of attack and a nearly parallel shift of the moment curve for angles of attack in the linear range. The α- and

c_ℓ-methods of drag prediction were in fairly good agreement with the measured drag up to the point of maximum lift-drag ratio, but underpredicted the drag at higher lift coefficients. For large booms a parallel shift of the lift curve occurred, but nonlinear differences between the drag and moment curves precluded simple correlation of the boom effects.

For triangular wings of small slackness with small constant-diameter leading-edge booms with front attachment, no adjustment to the lift curves to account for the booms was necessary. Both the α- and c_ℓ-methods of drag prediction were in good agreement with the drag curves in the linear range since the added boom drag appears to be small. In the nonlinear range both methods underpredicted the drag.

With regard to drag prediction in general, increased drag in the nonlinear range was generally due to tip stall for the rigid wings or the wings of NASA or triangular planform at low to moderate aspect ratios and slackness ratios. However, for combinations of large aspect and slackness ratios, root stall occurred for the rigid wings and wings of NASA planform. The tuft photographs of the rigid wing data generally confirmed the predicted onset of separation.

A prediction method for a luffing boundary was developed which correlated well with the minimum angles of attack at which wind tunnel data were taken.

The prediction methods presented have limitations with regard to their range of applicability. The value of slackness ratio is limited to that attainable under the right-circular cone assumption ($2\beta = 180^\circ$). For angles of attack at which the local lift coefficients from linear lifting-surface theory exceed plausible values, a lifting-surface method using nonlinear section data is desirable. An attempt to develop such a method reported herein seems worthwhile continuing. The tendency of the c_ℓ-method to underpredict the drag in the nonlinear range suggests joining it here to a theory based on little or no leading-edge suction.

It is noted that maximum lift-drag ratio usually occurs in the linear range where the accuracy of drag prediction is best.

Nielsen Engineering & Research, Inc.
Palo Alto, California
December 1, 1967

APPENDIX A

CALCULATION OF CAMBER AND TWIST DISTRIBUTIONS FOR A PARAWING LOBE FORMED FROM A RIGHT-CIRCULAR CONE

Specification of the parawing canopy shape is equivalent to finding the coordinates of a point on the canopy surface in the x,y,z coordinate system shown in figure A-1. From this information the coordinates of the trailing edge can be determined, and the twist distribution can be obtained. The chordwise surface coordinates can be obtained at a given spanwise location, and from these coordinates the camber can be found.

Equation of the Parawing Surface

The desired equation of the canopy surface is of the functional form

$$y = y(x,z) \tag{A-1}$$

where the x-axis lies along the root chord, the x-z plane is the root chord plane (the plane formed by the root chord and the leading edge), and the y-axis is perpendicular to the chord plane. The equation of the surface is most easily obtained in the x_o,y_o,z_o coordinate system, where the x_o-axis is the axis of the cone, as shown in figure A-1. These results are then transformed first to the x_1,y_1,z_1 coordinate system by a rotation about the z_o-axis, and then transformed to the x,y,z coordinate system by a rotation about the y_1-axis.

The transformation from the x_o,y_o,z_o system to the x_1,y_1,z_1 system is by a rotation σ such that

$$\left.\begin{aligned} \sin\sigma &= \frac{\sqrt{\cos^2\theta - \cos^2\phi}}{\cos\theta} \\ \cos\sigma &= \frac{\cos\phi}{\cos\theta} \end{aligned}\right\} \tag{A-2}$$

The coordinate transformation is

$$\left.\begin{aligned} x_o &= x_1\cos\sigma - y_1\sin\sigma \\ y_o &= x_1\sin\sigma + y_1\cos\sigma \\ z_o &= z_1 \end{aligned}\right\} \tag{A-3}$$

The transformation from the x_1, y_1, z_1 system to the x, y, z system is a rotation θ about y_1, such that

$$\left.\begin{aligned} x_1 &= x \cos\theta + z \sin\theta \\ y_1 &= y \\ z_1 &= x \sin\theta - z \cos\theta \end{aligned}\right\} \tag{A-4}$$

The equation of the cone in the x_o, y_o, z_o system is

$$x_o^2 \tan^2\phi - \left(y_o^2 + z_o^2\right) = 0 \tag{A-5}$$

Substitution of equations (A-2), (A-3), and (A-4) into equation (A-5) permits the cone equation to be written as

$$\begin{aligned} y^* = \frac{\cos\theta \cos\phi}{\cos^2\theta - \cos^2\phi - \cos^2\theta \cos^2\phi} \Bigg\{ & (1 + z^* \tan\theta)\left(\cos^2\theta - \cos^2\phi\right)^{1/2} \\ & - \Big[(1 + z^* \tan\theta)^2 (\cos^2\theta - \cos^2\phi) \\ & - z^*(z^* - \tan 2\theta)(1 - \tan^2\theta)(\cos^2\theta \cos^2\phi - \cos^2\theta + \cos^2\phi)\Big]^{1/2} \Bigg\} \end{aligned} \tag{A-6}$$

where

$$\left.\begin{aligned} y^* &= y/z \\ z^* &= z/x \end{aligned}\right\} \tag{A-7}$$

Determination of the Trailing-edge Coordinates

The trailing edge in the uninflated state can be specified by the polar equation

$$\ell_i = \ell_i(\gamma) \tag{A-8}$$

as shown in figure A-2. For a straight trailing edge[6], the coordinate, ℓ_i, can be expressed as

[6]While the analysis is not limited to a straight trailing edge, the computer program used in the analysis is so limited, because it uses equation (A-9).

$$\frac{\ell_i}{c_r} = \frac{\cos\gamma \pm \sqrt{\cos^2\gamma - \left(1 - \frac{k^2\sin^2\gamma}{\lambda^2\sin^2\theta_o}\right)}}{1 - \frac{k^2\sin^2\gamma}{\lambda^2\sin^2\theta_o}} \tag{A-9}$$

where

$$k^2 = \lambda^2 + c_r{}^2 - 2c_r\lambda\cos 2\theta \tag{A-10}$$

The sign convention on the radical of equation (A-9) is as follows:

positive for $c_r < \lambda\cos 2\theta_o$

negative for $c_r > \lambda\cos 2\theta_o$

In order to obtain a relation between the cone semiapex angle, ϕ, and the angles θ and θ_o, imagine that the uninflated planform is a circular sector, as shown dashed in figure A-2. When the canopy is wrapped around the cone, the trailing edge will be along the circular arc $\widehat{BC}$, as shown in the end view, figure A-3. The length of this arc may be expressed as

$$\widehat{BC} = 2\theta_o\lambda = 2r\beta = 2(\lambda\sin\phi)\beta \tag{A-11}$$

from which

$$\sin\phi = \frac{r}{\lambda} = \frac{\theta_o}{\beta} \tag{A-12}$$

The ratio of the arc length $\widehat{BC}$ to the chord $\overline{BC}$ is

$$\frac{\widehat{BC}}{\overline{BC}} = \frac{\beta}{\sin\beta} = \frac{2\lambda\theta_o}{2\lambda\sin\theta} = \frac{\theta_o}{\sin\theta} \tag{A-13}$$

Since θ_o and θ are specified quantities, equation (A-13) can be used to obtain β, which can then be used in equation (A-12) to obtain ϕ and r.

It is now necessary to obtain a relation between a given direction γ in the uninflated planform, figure A-2, and its associated angle in the chord plane of the inflated planform, say $\tan^{-1} z^*$ in figure A-4.

In figure A-3, the angle BOP' is given by $\lambda\gamma/r$. Then the following length relationship can be written

$$\overline{BE} = \overline{BD} - \overline{DE} = r \sin \beta - r \sin\left(\beta - \frac{\lambda\gamma}{r}\right) \tag{A-14}$$

The quantity z^* can be written in terms of $\overline{BE}$ as

$$z^* = \frac{\overline{BE} \cos \theta}{\lambda - \overline{BE} \sin \theta} \tag{A-15}$$

or using equation (A-14)

$$z^* = \frac{r\left[\sin \beta - \sin\left(\beta - \frac{\lambda\gamma}{r}\right)\right] \cos \theta}{\lambda - r \sin \theta \left[\sin \beta - \sin\left(\beta - \frac{\lambda\gamma}{r}\right)\right]} \tag{A-16}$$

Solving for γ yields first

$$\sin\left(\beta - \frac{\lambda\gamma}{r}\right) = \sin \beta - \frac{z^*\lambda}{r(\cos \theta + z^* \sin \theta)}$$

and finally, making use of equation (A-11),

$$\gamma = \beta \sin \phi - \sin \phi \sin^{-1}\left[\sin \beta - \frac{z^*}{\sin \phi(\cos \theta + z^* \sin \theta)}\right] \tag{A-17}$$

The determination of the trailing-edge coordinates is now done in a trial and error process using the above relationships. Basically, a spanwise station z is chosen and x is varied until the length ℓ_i to the trailing edge, figure A-2, is equal to that measured along the cone surface to the trailing-edge point. Let z be the spanwise station at which the trailing-edge coordinate is required. Form z^* by division with a trial value of the trailing-edge coordinate, x_t. From this value of z^*, a value y^* is computed from equation (A-6). Then the length L from the apex to the trailing edge can be computed from the relation

$$L = x_t \sqrt{1 + y^{*2} + z^{*2}} \tag{A-18}$$

From z^* and equation (A-17), the angle γ of the uninflated parawing can be obtained. The trailing-edge shape $\ell(\gamma)$ then yields a value of ℓ_i for comparison with L. If the two are not sufficiently close, a

new value of x_t is selected and the calculations repeated until convergence is obtained.

A slackness ratio can be defined for the type of planform shown in figure 1, although it does not have the same significance as in the triangular inflated planform case. In that case, the slackness ratio is defined as the difference between the canopy trailing-edge length and the inflated semispan, divided by the inflated semispan. This definition can be carried over to an arbitrary planform by defining the two lengths as the canopy trailing-edge length and the distance from the aft end of the leading edge to the aft end of the root chord measured in the inflated state. The former is the length $\overline{AC}$ of figure A-2, and can be expressed as

$$\overline{AC} = \sqrt{\lambda^2 \sin^2 2\theta_o + (\lambda \cos 2\theta_o - c_r)^2} \tag{A-19}$$

The latter is the straight-line distance between A and C' in figure A-4, say $\overline{AC'}$, where

$$\overline{AC'} = \sqrt{\lambda^2 \sin^2 2\theta + (\lambda \cos 2\theta - c_r)^2} \tag{A-20}$$

The slackness ratio, R, then is

$$R = \frac{\overline{AC} - \overline{AC'}}{\overline{AC'}} \tag{A-21}$$

where $\overline{AC}$ and $\overline{AC'}$ are obtained from equations (A-19) and (A-20).

Twist and Camber Distribution

With the trailing-edge coordinates known, the determination of the twist distribution is straightforward. Let z_ν be the spanwise station at which the twist and camber are desired. The other coordinates of the trailing edge, computed as in the previous section, are y_{t_ν} and x_{t_ν}. The local chord, c_ν, joining the leading and trailing edges has as its length

$$c_\nu = \sqrt{\left(x_{t_\nu} - x_{\ell_\nu}\right)^2 + y_{t_\nu}{}^2 + z_{t_\nu}{}^2} \tag{A-22}$$

where the leading-edge coordinates are given by

$$x_{\ell_\nu} = z_\nu \operatorname{ctn}(2\theta) \qquad y_{\ell_\nu} = 0 \qquad z_{\ell_\nu} = 0 \tag{A-23}$$

The geometric twist angle is then

$$\epsilon_\nu = -\sin^{-1}\left(\frac{y_{t_\nu}}{c_\nu}\right) \tag{A-24}$$

The coordinates for the camber determination are illustrated in figure A-5. The desired camber distribution is the variation of the ζ/c_ν of the canopy surface with ξ/c_ν. Since the canopy surface coordinates are known in the x,y,z system from equation (A-6), these may be transformed into the ζ,ξ system for a given z to obtain the desired camber variation. Rather than doing this, however, an iterative approach was used in a computer program, and this is described below.

It is desired that the camber be known at 13 specific ξ/c_ν values since the Pankhurst method is used later to compute the angle of zero lift of the local section and its zero-lift pitching moment.[7] For the nth ξ/c_ν station, an initial value of x is selected and the quantities y_a and y_b are computed as shown in figure A-5. The quantity y_a is the coordinate of the surface as given by equation (A-6). The quantity y_b is computed from the following expression

$$y_b = \frac{\left(\frac{\xi}{c_\nu}\right)_n c_\nu}{\sin \epsilon_\nu} - \frac{x - x_{\ell_\nu}}{\tan \epsilon_\nu} \tag{A-25}$$

The values of y_a and y_b are compared, and if they do not agree within a specified limit, the value of x is changed and the y_a and y_b recomputed and compared. This process is repeated until agreement is obtained, which will occur when $x = x_n$. Then the camber can be obtained by the relation

$$\zeta_n = y_n \cos \epsilon_\nu - \left(x_n - x_{\ell_\nu}\right) \sin \epsilon_\nu \tag{A-26}$$

This is done for each of the 13 chordwise stations at every spanwise station of interest.

---

[7]The values of ξ/c_ν correspond to "Spacing (4)" of tables 1 and 4 of reference 9.

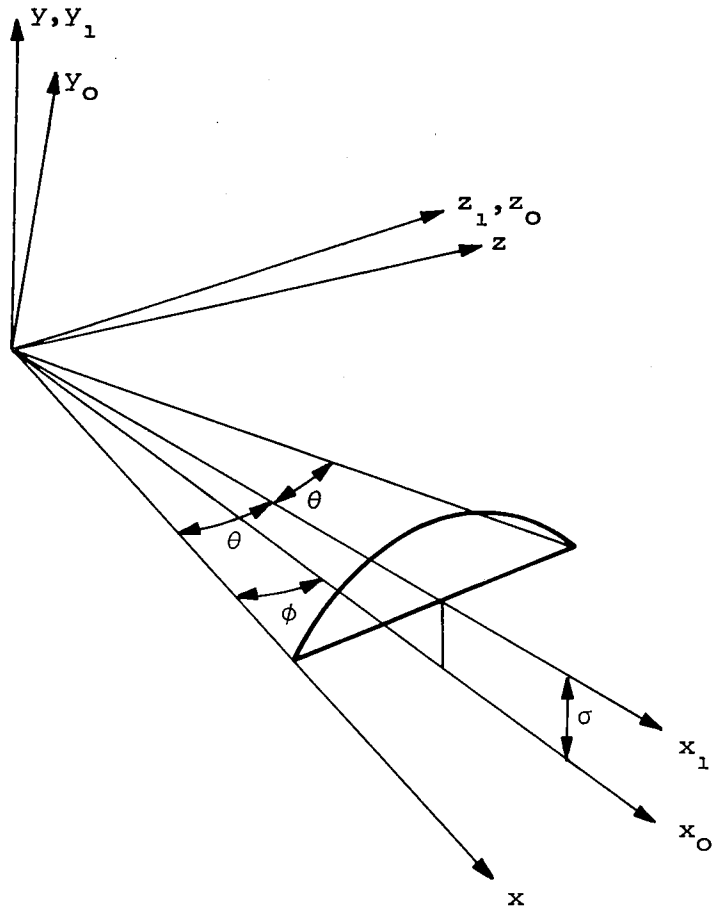

Figure A-1.- Coordinate axis systems for parawing conical surface.

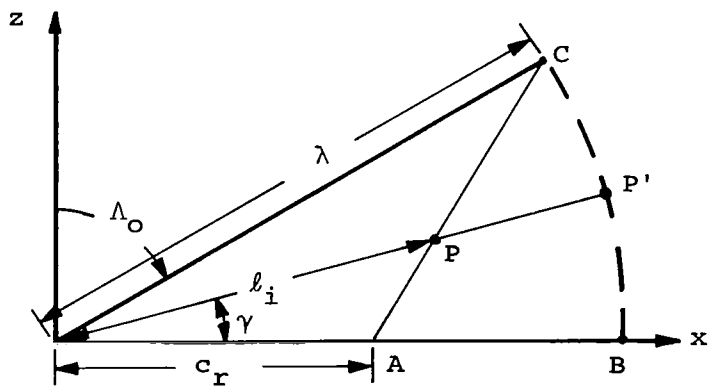

Figure A-2.- Parawing planform in the uninflated state.

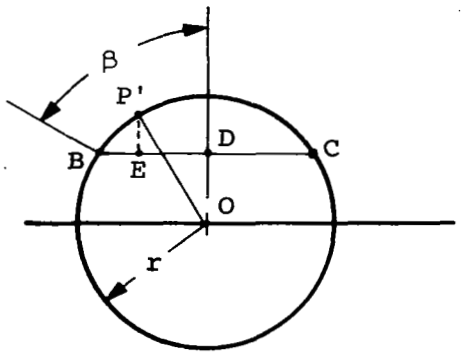

Figure A-3.- End view along cone axis of the inflated parawing.

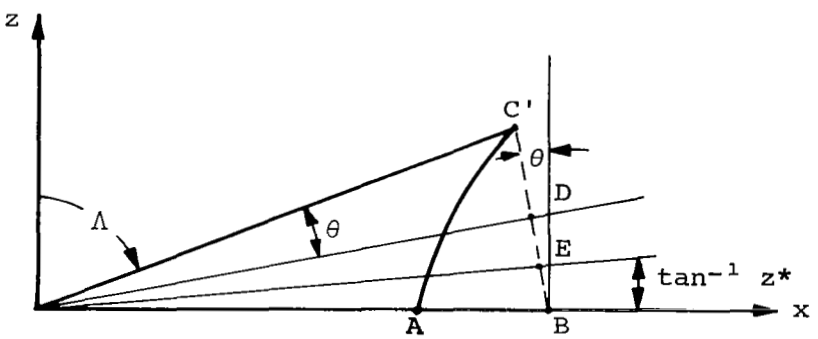

Figure A-4.- Parawing planform in the inflated state.

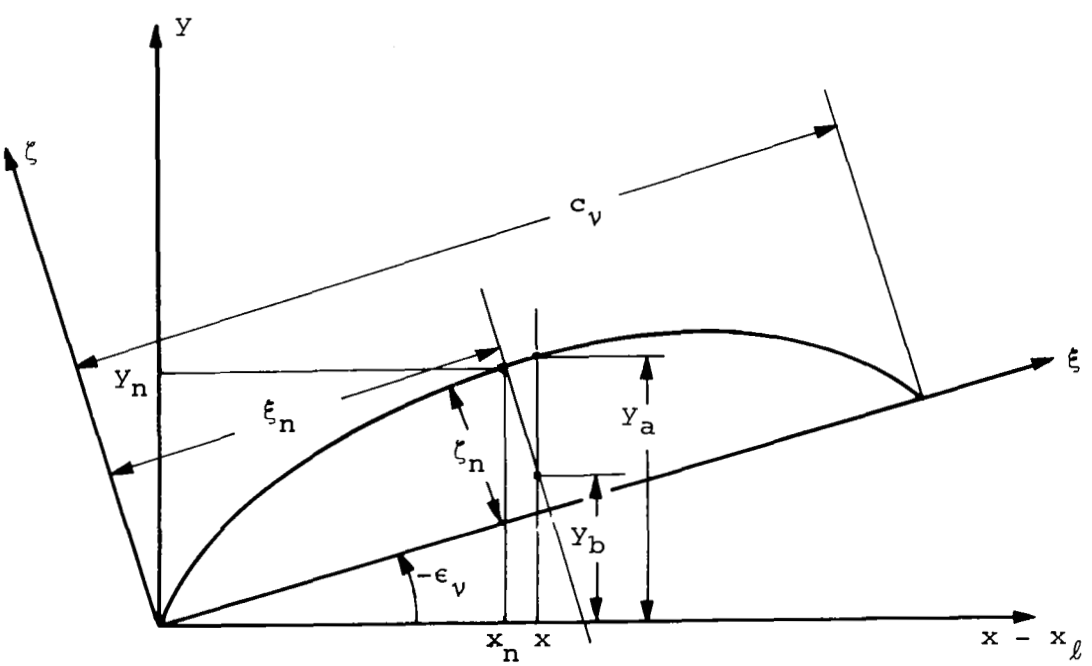

Figure A-5.- Camber coordinates.

APPENDIX B

COMPARISON OF WEISSINGER AND MULTHOPP METHODS

Comparisons were made for a number of wings between the aerodynamic characteristics computed using the Weissinger-Pankhurst method and those computed with the Multhopp method. The purpose was twofold: first, as a check on the accuracy of the Weissinger-Pankhurst calculative method; and second, as an evaluation of the magnitudes of the effects neglected or approximated in the Weissinger-Pankhurst method. These effects are generally associated with chordwise variations of induced camber and loading and any sweep effects on C_{m_o} which the Weissinger-Pankhurst method is unable to take into account.

The first consideration is the difference in chord distribution between the Weissinger and Multhopp calculative methods. The chord lengths used with the Weissinger method are computed from a conical fit to the canopy shape which considers the canopy trailing edge to be straight in the uninflated state. Thus, the inflated canopy trailing edge is curved, and its projection onto the root chord plane is curved. The Weissinger computer program can also be run with a planform chord distribution for a straight planform trailing edge, and this was done for some check cases. The Multhopp program computes a chord distribution based on a straight planform trailing edge. For numerical computation reasons, however, the Multhopp program fairs a radius to any discontinuous slope change in a constant percent chord line, such as occurs at the root section. An example of the differences in the chord distributions for a high slackness wing is shown in figure B-1. The Multhopp curve, with 21 control points across the span, illustrates the fairing at the root chord with a linear variation for $\eta > 0.14$. The 7-point Multhopp results in the figure indicate a somewhat larger deviation from linearity over the span. The maximum difference between the Multhopp and conical canopy chords occurs near $\eta = 0.2$ and represents about a 10 percent difference.

A comparison of predicted aerodynamic performance for the wing of figure B-1, illustrating the influence of both chord distribution and chordwise effects, is shown in table B-I. Four cases were computed. The first two cases are based on Weissinger calculations using first the actual (cone fit) chord and then a linear chord variation (straight planform trailing edge). The last two cases are based on Multhopp calculations

first with 21 span and 6 chord points and then with 7 span and 1 chord points. The latter case should correspond most closely to the Weissinger run with a linear chord variation since, with only one chord station, the Multhopp flow model is that of an uncambered twisted wing. The two Weissinger and the 7-point Multhopp cases agree very closely, except for the Multhopp lift-curve slope. The reason for the high C_{L_α} value for Multhopp is not known. It should be noted that these three C_{m_o} values do not include the effect of the moment due to camber. A comparison of the 21-point Multhopp case with the other three indicates the magnitude of the chordwise effects neglected in the Weissinger method. The greatest difference occurs in α_o. With the relatively high camber of this wing (up to 10 percent), the loading due to camber cannot be considered as concentrated at the quarter chord, as assumed in the present application of the Weissinger method to cambered wings. The Weissinger method, however, gives a good estimate of the lift-curve slope, induced drag, center of pressure, and moment-curve slope, as well as C_{m_o} when the Pankhurst correction for moment due to camber is added.

Comparisons of Weissinger and Multhopp predictions for a number of wings are given in table B-II. The Weissinger results were obtained using the actual chord distributions from the cone method. The Multhopp results were obtained using 21 spanwise and 6 chordwise control points. The first three wings have NASA planforms and the same 2β value, and illustrate the effect of aspect ratio on the agreement between the two methods. The major differences occur in α_o, C_{m_o}, and C_{m_α}. The Weissinger method overpredicts α_o and C_{m_α} at low aspect ratio and underpredicts the two at high aspect ratio. The C_{m_o} values of Weissinger, which include the correction for camber, are consistently low, but the difference decreases with increasing aspect ratio. The next series of three wings, also NASA planforms, illustrates the slackness effect at a constant, moderate aspect ratio. For low slackness, the methods agree well, except for C_{m_o}. The agreement remains good to high slackness, except for α_o. It should be noted that the C_{m_o} calculation of the Weissinger method requires taking the difference between two numbers which are large compared to their difference. Thus, small inaccuracies in either one will affect their difference considerably. The last three rigid wings of moderate to high aspect ratio and moderate slackness were used as the basis for drawing conclusions on the basic canopy

aerodynamic prediction methods. The agreement is good for all values except C_{m_α}, where the maximum difference is about 14 percent.

The results of the Weissinger-Multhopp comparisons for α_o are summarized in figure B-2. The upper and lower sets of curves contain the same results and differ only in the manner of presentation. These results indicate two simultaneous chordwise effects occurring that are neglected in the Weissinger method. The first effect is associated with induced camber produced primarily by the trailing vortex system. This effect becomes significant at low aspect ratio. Figure B-2 indicates that the Weissinger method overpredicts α_o by as much as 4° for a NASA planform of aspect ratio 1 and a high slackness. The second effect is associated with the chordwise loading due to high camber at high slackness. In this case the chord loading is concentrated further aft than the quarter chord, and the Weissinger method underpredicts α_o. For a given aspect ratio, the difference increases with increasing slackness and can attain a value of -4° at aspect ratio 3 and $2\beta = 150^o$.

The results of the Weissinger-Multhopp comparisons for C_{m_o} are summarized in figure B-3. The values predicted by the Weissinger-Pankhurst method in figure B-3 consist of the sum of the moment at zero wing lift on the equivalently twisted (and uncambered) wing and the moment due to camber. The latter is evaluated by using the Pankhurst method to obtain c_{m_o} values at the 7 Weissinger span stations and integrating these over the span using equation (3). The results of figure B-3 indicate that the Weissinger-Pankhurst method underpredicts C_{m_o} by an amount that increases with increasing slackness and decreasing aspect ratio. The differences represented in figure B-3 are differences between two theoretical, inviscid aerodynamic prediction methods and are due primarily to chordwise effects, which the Weissinger method is unable to take into account, a sweep effect neglected in the Pankhurst method in obtaining the moment due to camber, and possibly some inaccuracy due to the integration method. In addition to these differences, there are viscous effects on C_{m_o} which are discussed in the RESULTS section. It should be noted that the results of figure B-3 can be used as a correction to the Weissinger-Pankhurst method for NASA planform wings, in the absence of the Multhopp computer program.

TABLE B-I

COMPARISON OF PREDICTED AERODYNAMIC PERFORMANCE FOR A NASA PLANFORM WING OF ASPECT RATIO 2.57, $\Lambda = 50^{\circ}$, and $2\beta = 158^{\circ}$

	Weissinger		Multhopp	
	Planform Chords	Circular Cone Chords	m = 21, n = 6	m = 7, n = 1
C_{L_α}	2.7365	2.7223	2.7196	2.8023
C_{m_α}	-.1654	-.1685	-.1735	-.1667
C_{D_i}/C_L^2	.1252[a]	.1247[a]	.1265[a]	.1249[a]
α_o	18.463	18.569	21.820	18.541
C_{m_o}	.0645[b]	.06591[b]	-.00580	.0698[b]
η_{cp}	.4091	.4114	.4025	.3935
x_{cp}/c_r	.4611	.4623	.465	.461
S/c_r^2	.643	.643	.643	.643

[a]These values are for a flat wing of the appropriate planform and aspect ratio and were used only to evaluate the differences between the theoretical methods.

[b]No correction added for moment at zero wing lift due to camber. With the correction for camber, the value for the Weissinger method with circular cone chords is -0.0138.

TABLE B-II

COMPARISON OF WEISSINGER AND MULTHOPP RESULTS

Wing	Theory	α_o (deg)	C_{m_o} [a,b]	C_{L_α}	C_{m_α} [a]	C_{D_i}/C_L^2 [c]	η_{cp}	$x_{cp}/(b/2)$
$A = 1$, $\Delta\Lambda = 5^\circ$	W	6.37	-0.0177	1.261	-0.114	0.318	0.421	2.204
$2\beta = 149^\circ$	M	2.51	- .0001	1.332	- .185	.319	.410	2.326
$A = 2$, $\Delta\Lambda = 10^\circ$	W	12.94	- .0159	2.269	- .195	.160	.416	1.012
$2\beta = 149^\circ$	M	13.64	.0027	2.284	- .214	.161	.407	1.036
$A = 3$, $\Delta\Lambda = 15^\circ$	W	20.09	- .0199	2.984	- .131	.108	.405	.554
$2\beta = 149^\circ$	M	24.21	- .0237	2.989	- .118	.110	.398	.551
$A = 2.5$, $\Delta\Lambda = 3^\circ$	W	7.47	- .0126	2.677	- .161	.129	.410	.745
$2\beta = 85^\circ$	M	7.31	- .0037	2.670	- .181	.130	.403	.755
$A = 2.5$, $\Delta\Lambda = 8^\circ$	W	12.74	- .0156	2.673	- .161	.129	.411	.746
$2\beta = 125^\circ$	M	13.24	- .0051	2.670	- .181	.130	.403	.755
$A = 2.5$, $\Delta\Lambda = 15^\circ$	W	18.31	- .0125	2.673	- .166	.128	.412	.748
$2\beta = 159^\circ$	M	21.43	- .0043	2.670	- .181	.130	.403	.745
Rigid Wing No. 3	W	12.66	.126	3.360	- .464	.0604	.400	.588
$A = 5.45$, $2\beta = 103^\circ$	M	13.72	.127	3.480	- .497	.0613	.394	.589
Rigid Wing No. 6	W	11.51	.044	3.174	- .309	.082	.404	.631
$A = 4$, $2\beta = 103^\circ$	M	12.07	.0513	3.203	- .362	.083	.397	.639
Rigid Wing No. 8	W	10.50	.00	2.910	- .208	.108	.407	.684
$A = 3$, $2\beta = 103^\circ$	M	10.70	.0088	2.913	- .239	.109	.401	.693

[a] The reference quantity for C_{m_o} and C_{m_α} is the mean aerodynamic chord, and the moment center is at the quarter mean aerodynamic chord.

[b] The Weissinger values include the correction for moment at zero wing lift due to camber calculated by equation (3).

[c] These values are for a flat wing of the appropriate planform and aspect ratio and were used only to evaluate the differences between the two theoretical prediction methods.

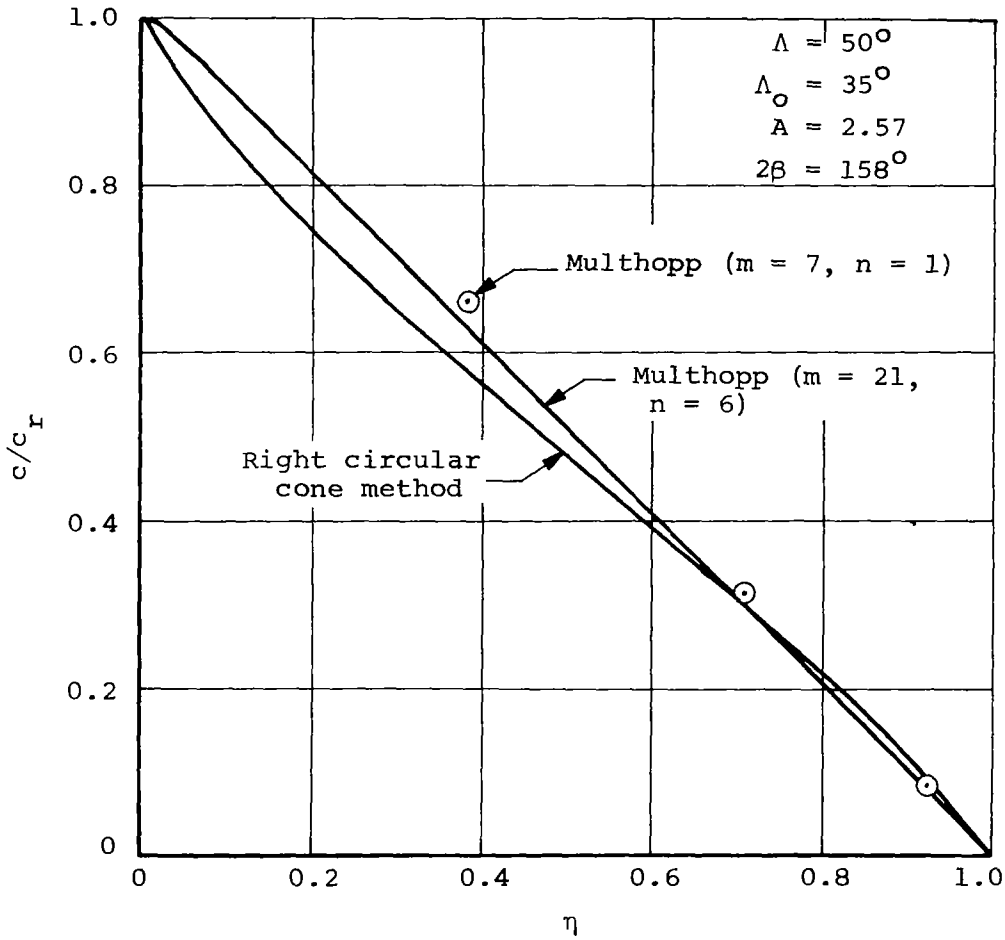

Figure B-1.- Comparison of theoretical chord distributions for a NASA planform parawing.

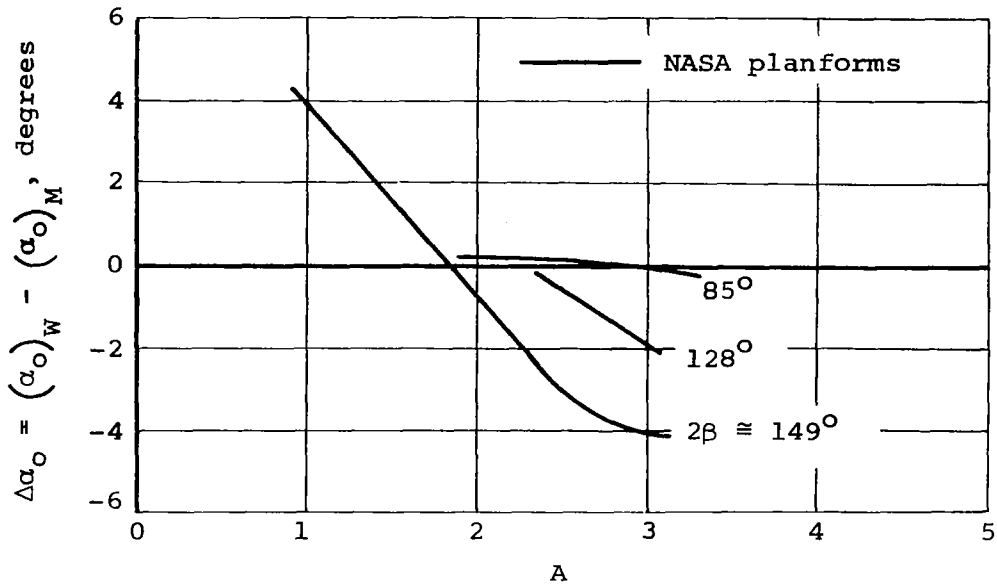

(a) Aspect ratio effect at constant slackness.

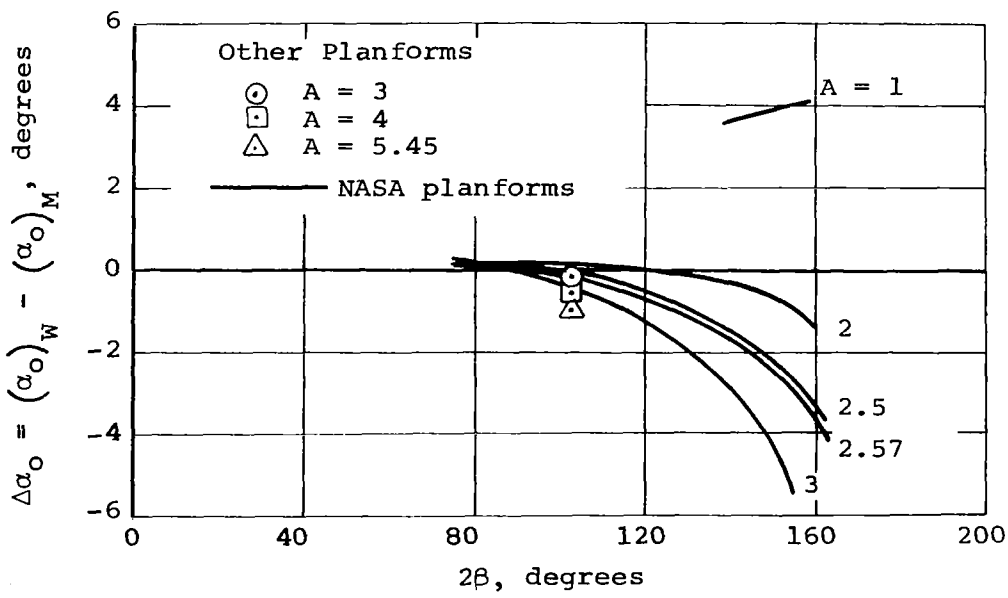

(b) Slackness effect at constant aspect ratio.

Figure B-2.- Summary of comparisons of Multhopp and Weissinger predictions for angle of zero lift.

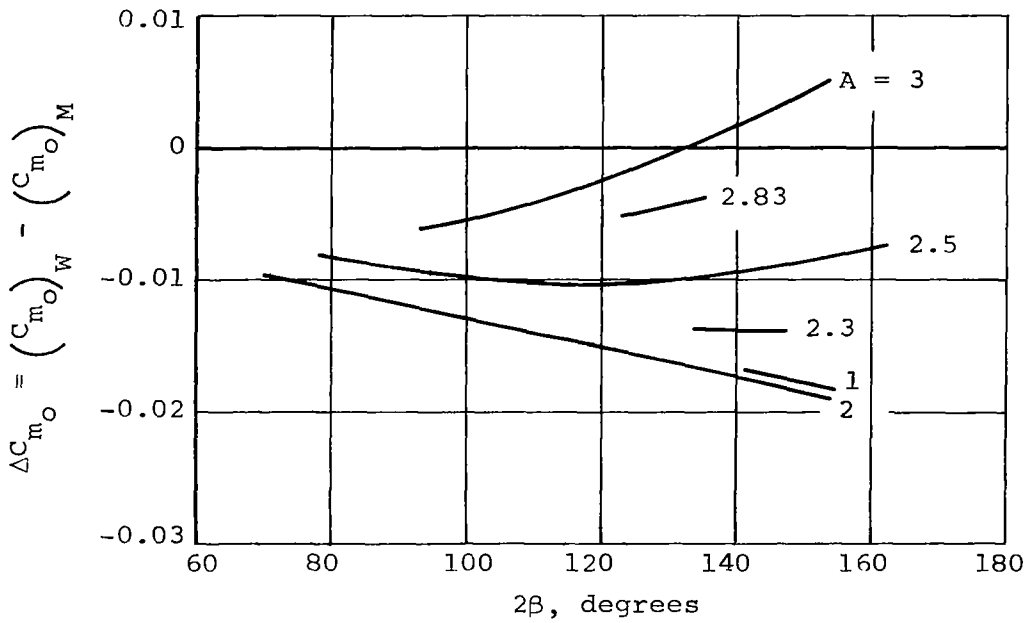

Figure B-3.- Summary of comparisons of Weissinger-Pankhurst and Multhopp predictions for wing moment at zero lift of NASA planform wings.

REFERENCES

1. Nielsen, J. N., Kriebel, A. R., and Goodwin, F. K.: Theoretical Aerodynamics of Flexible Wings at Low Speeds, Part I - One-Lobed Parawings. Vidya Rep. No. 84, covering period Jan. 15, 1962 to Feb. 15, 1963.

2. Nielsen, J. N., et al.: Theoretical Aerodynamics of Flexible Wings at Low Speeds, Part II - Two-Lobed Parawings. Vidya Rep. No. 133, May 1964.

3. Kriebel, A. R. and Nielsen, J. N.: Theoretical Aerodynamics of Flexible Wings at Low Speeds, Part III - Approximate Results for Wings of Large Aspect Ratio. Vidya Rep. No. 146, July 1, 1964.

4. Burnell, J. A. and Nielsen, J. N.: Theoretical Aerodynamics of Flexible Wings at Low Speeds, Part IV - Experimental Program and Comparison with Theory. Vidya Rep. No. 172, Feb. 15, 1965.

5. Polhamus, E. C. and Naeseth, R. L.: Experimental and Theoretical Studies of the Effects of Camber and Twist on the Aerodynamic Characteristics of Parawings Having Nominal Aspect Ratios of 3 and 6. NASA TN D-972, Jan. 1963.

6. Nielsen, J. N. and Burnell, J. A.: Theoretical Aerodynamics of Flexible Wings at Low Speeds, Part V - Engineering Method for Estimating Parawing Performance. Vidya Rep. No. 209, Dec. 1, 1965.

7. Fournier, P. G. and Bell, B. A.: Low Subsonic Pressure Distributions on Three Rigid Wings Simulating Paragliders with Varied Canopy Curvature and Leading-Edge Sweep. NASA TN D-983, Nov. 1961.

8. DeYoung, J. and Harper, C. W.: Theoretical Symmetric Span Loading at Subsonic Speeds for Wings Having Arbitrary Planform. NACA Rep. No. 921, 1948.

9. Pankhurst, R. C.: A Method for the Rapid Evaluation of Glauert's Expressions for the Angle of Zero Lift and the Moment at Zero Lift. ARC R&M No. 1914, Mar. 23, 1944.

10. van Spiegel, E. and Wouters, J. G.: Modifications of Multhopp's Lifting Surface Theory with a View to Automatic Computation. Nat'l. Aero- and Astronautical Research Inst. Rep. NLR-TN W.2, Amsterdam, Netherlands, June 1962.

11. Wick, B. H.: Study of the Subsonic Forces and Moments on an Inclined Plate of Infinite Span. NACA TN 3221, June 1954.

12. Abbott, I. H. and von Doenhoff, A. E.: Theory of Wing Sections. Dover Publications, Inc., New York, 1959.

13. Wilson, H. B. and Horton, E. A.: Aerodynamic Characteristics at High and Low Subsonic Mach Numbers of Four 6-Series Airfoil Sections at Angles of Attack from -2° to 31°. NACA RM L53C20, June 5, 1953.

14. Lindsey, W. F. and Landrum, E. J.: Flow and Force Characteristics of 2-Percent-Thick Airfoils at Transonic Speeds. NACA RM L54I30, Jan. 1955.

15. Prandtl, L. and Betz, A.: Ergebnisse der Aerodynamischen Versuchsanstalt zu Göttingen. R. Oldenbourg, Munich and Berlin, vol. II, 1932. Flachsbart, O.: Messungen an ebenen und gewölbten Platten, pp. 96-100.

16. Polhamus, E. C.: A Note on the Drag Due to Lift of Rectangular Wings of Low Aspect Ratios. NACA TN 3324, Jan. 1955.

17. Bursnall, W. J. and Loftin, L. K.: Experimental Investigation of the Pressure Distribution about a Yawed Circular Cylinder in the Critical Reynolds Number Range. NACA TN 2463, Sept. 1961.

18. Diederich, F. W. and Zlotnick, M.: Experimental Investigation of the Pressure Distribution about a Yawed Circular Cylinder in the Critical Reynolds Number Range. NACA TN 2463, Sept. 1961.

19. Bugg, F. M.: Effects of Aspect Ratio and Canopy Shape on Low-Speed Aerodynamic Characteristics of 50.0° Swept Parawings. NASA TN D-2922, July 1965.

20. Naeseth, R. L. and Gainer, T. G.: Low-Speed Investigation of the Effects of Wing Sweep on the Aerodynamic Characteristics of Parawings Having Equal-Length Leading Edges and Keel. NASA TN D-1957, Aug. 1963.

21. Croom, D. R., Naeseth, R. L., and Sleeman, W. C.: Effects of Canopy Shape on Low-Speed Aerodynamic Characteristics of a 55° Swept Parawing with Large Diameter Leading Edges. NASA TN D-2551, Dec. 1964.

TABLE I

GEOMETRIC PARAMETERS FOR RIGID WINGS

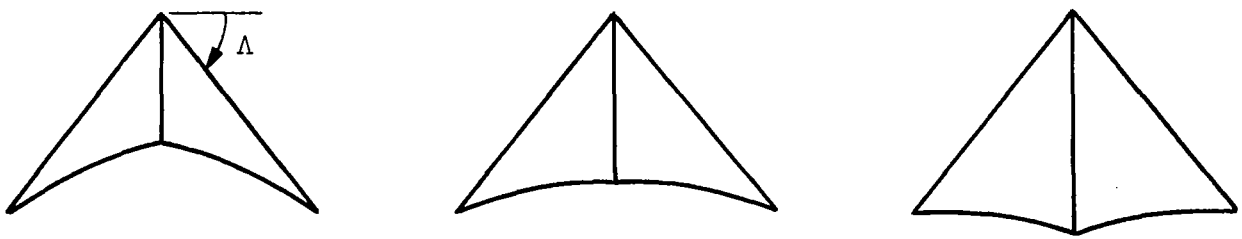

A = 5.45 A = 4.0 A = 3.0

Inflated canopy planforms

Wing No.	Reference No.	A	Λ_o (deg)	Λ (deg)	c_r (in.)	λ (in.)	b (in.)	$\frac{\ell_o - \ell}{\ell}$	2β (deg)	x_{c_m} (in.)	ℓ_{ref} (in.)
1	8	5.45	35.0	50	23.57	50	64.28	0.167	157.8	16.70	15.71
2		↕	40.0	↓	↕	↓	↓	.110	135.1	↕	↕
3			45.0					.054	102.9		
4			47.5					.027	79.2		
5		5.45	50.0		23.57			0	0	16.70	15.71
6		4.0	45.0		32.14			.085	102.9	18.16	21.44
7		4.0	50.0		32.14			0	0	18.16	21.44
8		3.0	45.0		42.80			.113	102.9	19.90	28.55
9		3.0	50.0		42.80			0	0	19.90	28.55

TABLE II

GEOMETRIC PARAMETERS FOR FLEXIBLE PARAWINGS

Wing No.	Reference No.	A	Λ_o (deg)	Λ (deg)	c_r (in.)	b (in.)	$\frac{d}{c_r}$	$\frac{\ell_o - \ell}{\ell}$	2β (deg)	x_{cm} (in.)	ℓ_r (in.)	Canopy Attachment[b]
11	19	5.45	35.0	50.0	23.57	64.28	0.021[a]	0.167	157.8	16.70	15.71	F
12		↕	40.0	↓	↕	↓	↕	.110	135.1	↕	↕	↓
13		↓	45.0		↓		↓	.154	102.9	↓	↓	
14		5.45	47.5		23.57		.021[a]	.027	79.2	16.70	15.71	
16		4.0	45.0		34.14		.016[a]	.085	102.9	18.16	21.44	
18		3.0	45.0		42.80		.012[a]	.113	102.9	19.90	28.55	
23	5	5.45	45.0	50.0	23.57	64.28	.021[a]	.054	102.9	15.70	23.57	F
AR2-2.07	4	2.0	61.23	63.43	36.0	36.0	.021	.059	74.2	22.8	24.0	F
AR2-2.10		2.0	60.73	63.43	↓	36.0	↓	.094	90.3	22.8	↓	↓
AR3-2.04		3.0	51.45	53.10		54.0		.038	68.9	21.8		

[a]The value shown is an average, the leading-edge diameter is tapered from 0.75 in. at the root to 0.25 in. at the tip.

[b]Canopy attachment: F - front
P - pocket

TABLE II

CONCLUDED

Wing No.	Reference No.	A	Λ_o (deg)	Λ (deg)	c_r (in.)	b (in.)	$\frac{d}{c_r}$	$\frac{\ell_o - \ell^c}{\ell}$	2β (deg)	x_{cm} (in.)	ℓ_r (in.)	Canopy Attachment[b]
35-40	20	3.06	35.0	40.0	50.0	76.60	0.015	0.0926	98.8	25.0	50.0	P
35-45		2.83		45.0		70.71		.207	130.5			
35-50		2.58		50.0		64.28		.350	157.8			
35-55		2.30		55.0		57.36		.536	-			
35-60		2.00		60.0		50.0		.784	-			
35-65		1.69		65.0		42.26		1.133	-			
45-50	20	2.58	45.0	50.0	50.0	64.28	.015	.119	102.9	25.0	50.0	P
45-55		2.30		55.0		57.36		.273	141.1			
45-60		2.00		60.0		50.0		.479	-			
45-65		1.69		65.0		42.26		.768	-			
45-70		1.37		70.0		34.20		1.204	-			
55-60	20	2.0	55.0	60.0	50.0	50.0	.015	.162	133.9	25.0	50.0	P
55-65		1.69		65.0		42.26		.389	159.0			
55-70		1.37		70.0		34.20		.733	-			
55-75		1.04		75.0		25.88		1.305	-			
52.5-55	21	2.30	52.5	55.0	39.3	45.07	.07	.069	80.9	19.6	39.3	F
50.0-55			50.0					.137	106.8			
47.5-55			47.5					.205	125.8			
45.0-55			45.0					.273	141.1			
42.5-55			42.5					.339	153.8			

[c]For NASA planforms, canopies having $(\ell_o - \ell)/\ell > 0.45$ cannot lie on the surface of a right circular cone.

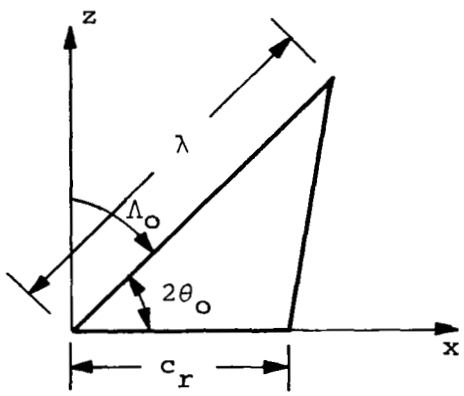

(a) Planform of uninflated wing panel.

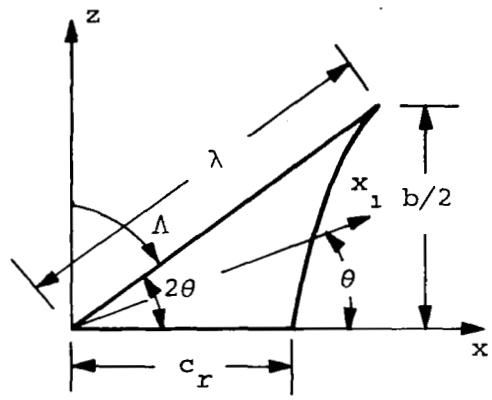

(b) Planform of inflated wing panel.

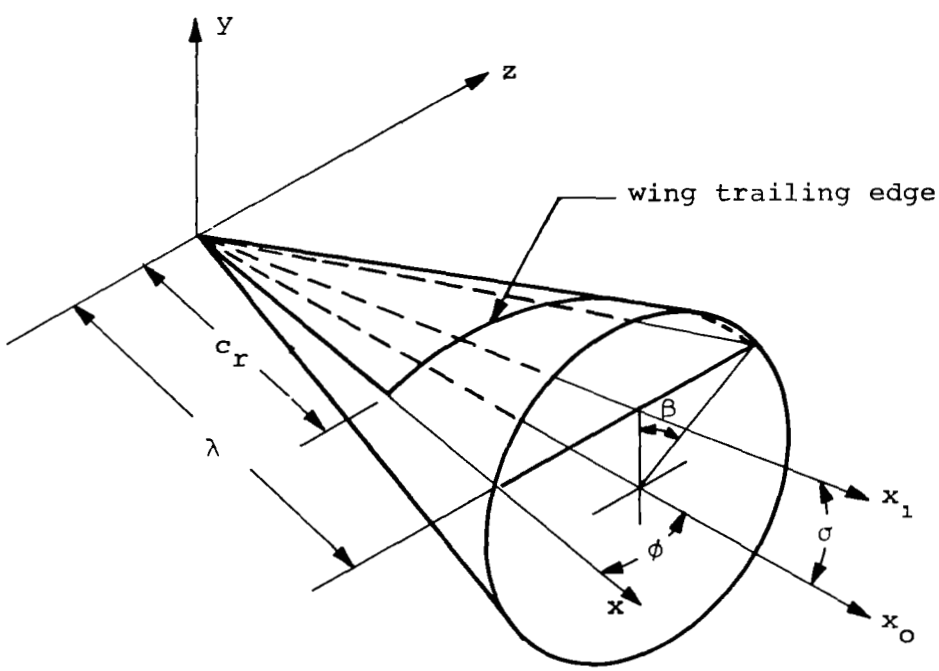

(c) Parawing panel as part of a right circular cone.

Figure 1.- Parawing lobe as part of the surface of a right circular cone.

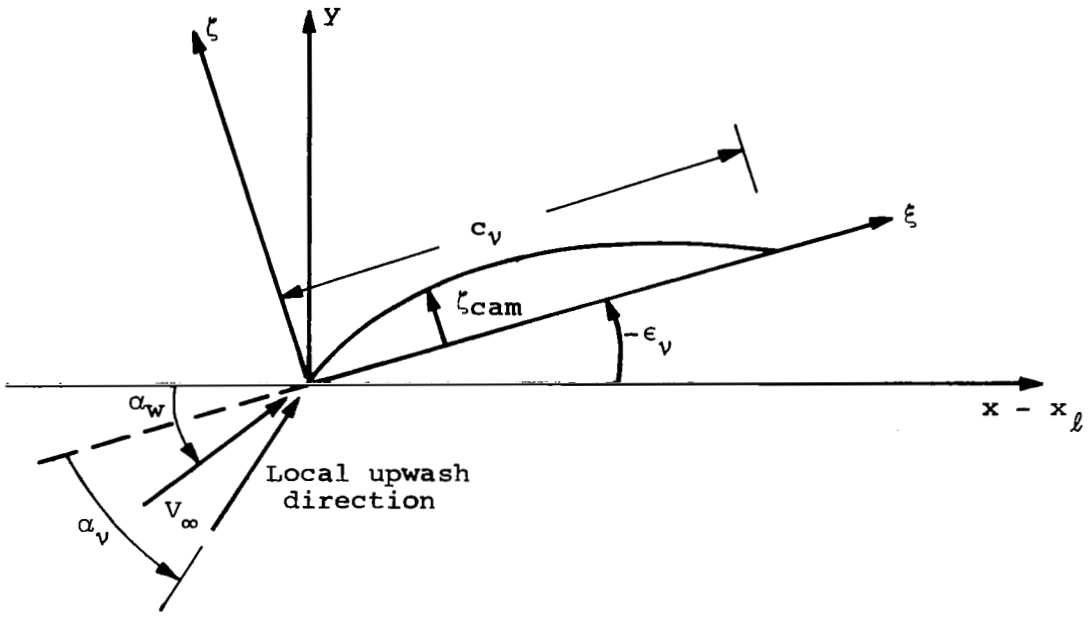

Figure 2.- Flow directions at local spanwise station.

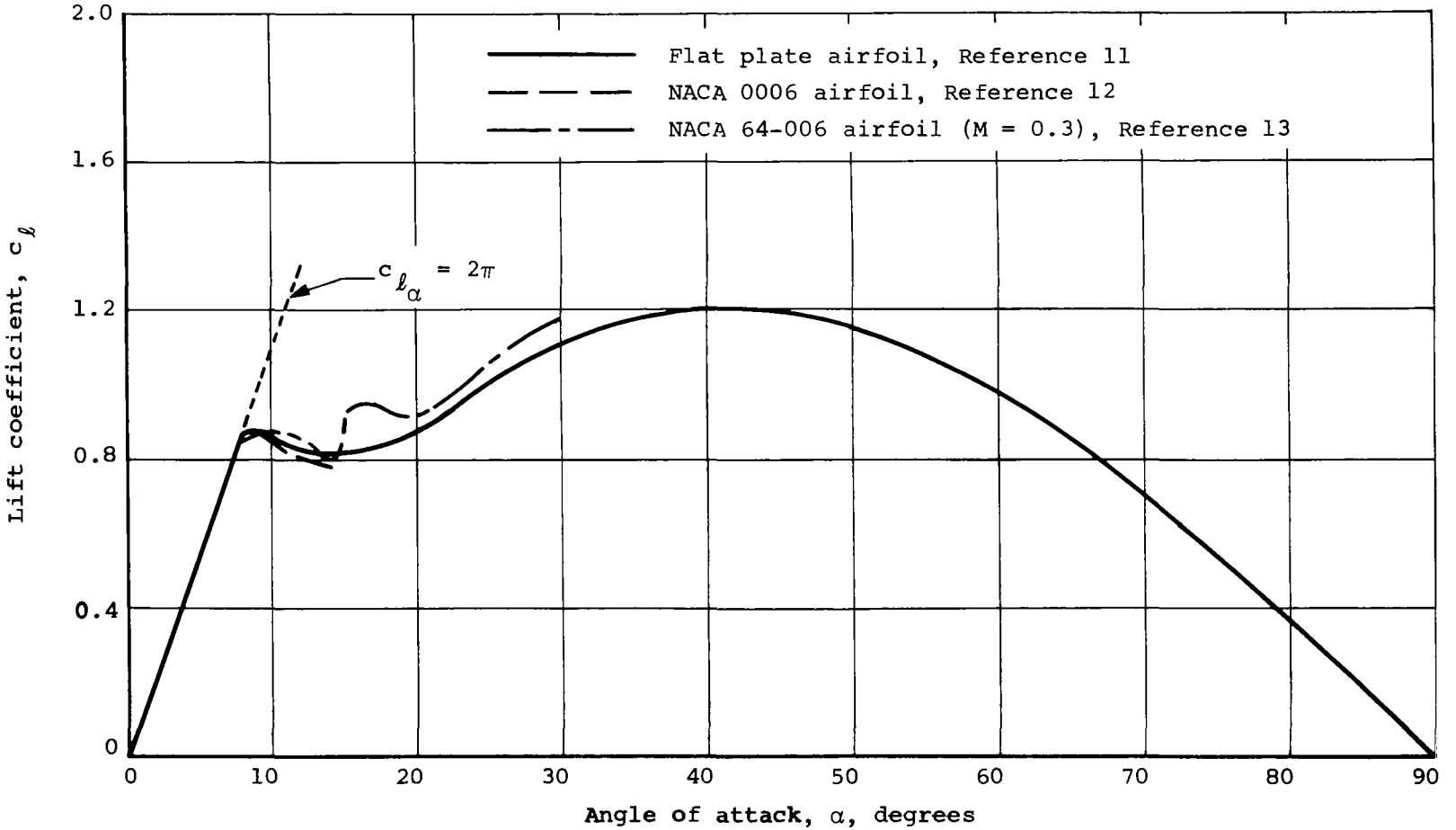

(a) Lift coefficient versus angle of attack.

Figure 3.- Section data for uncambered thin airfoils.

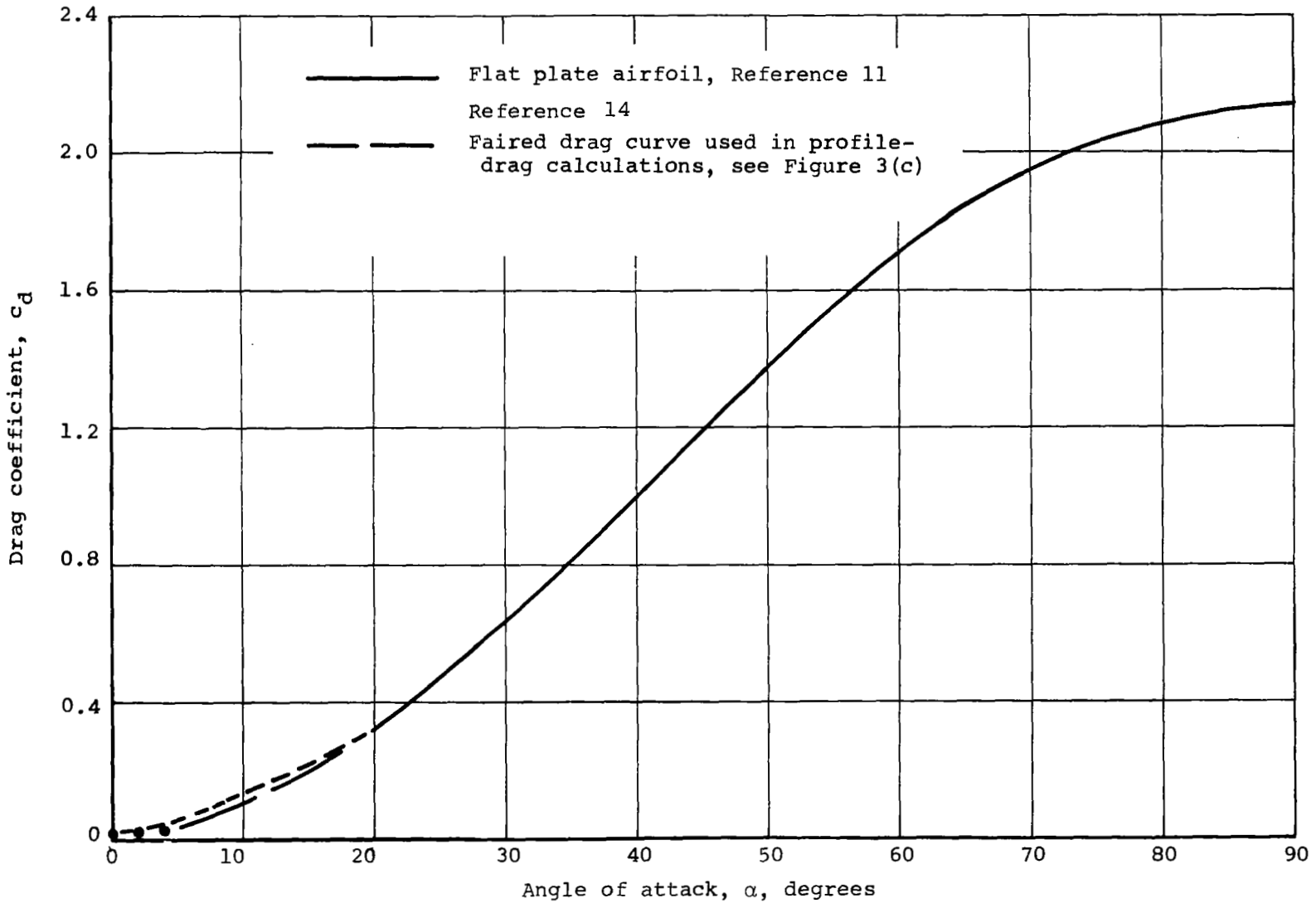

(b) Drag coefficient versus angle of attack.

Figure 3.- Continued.

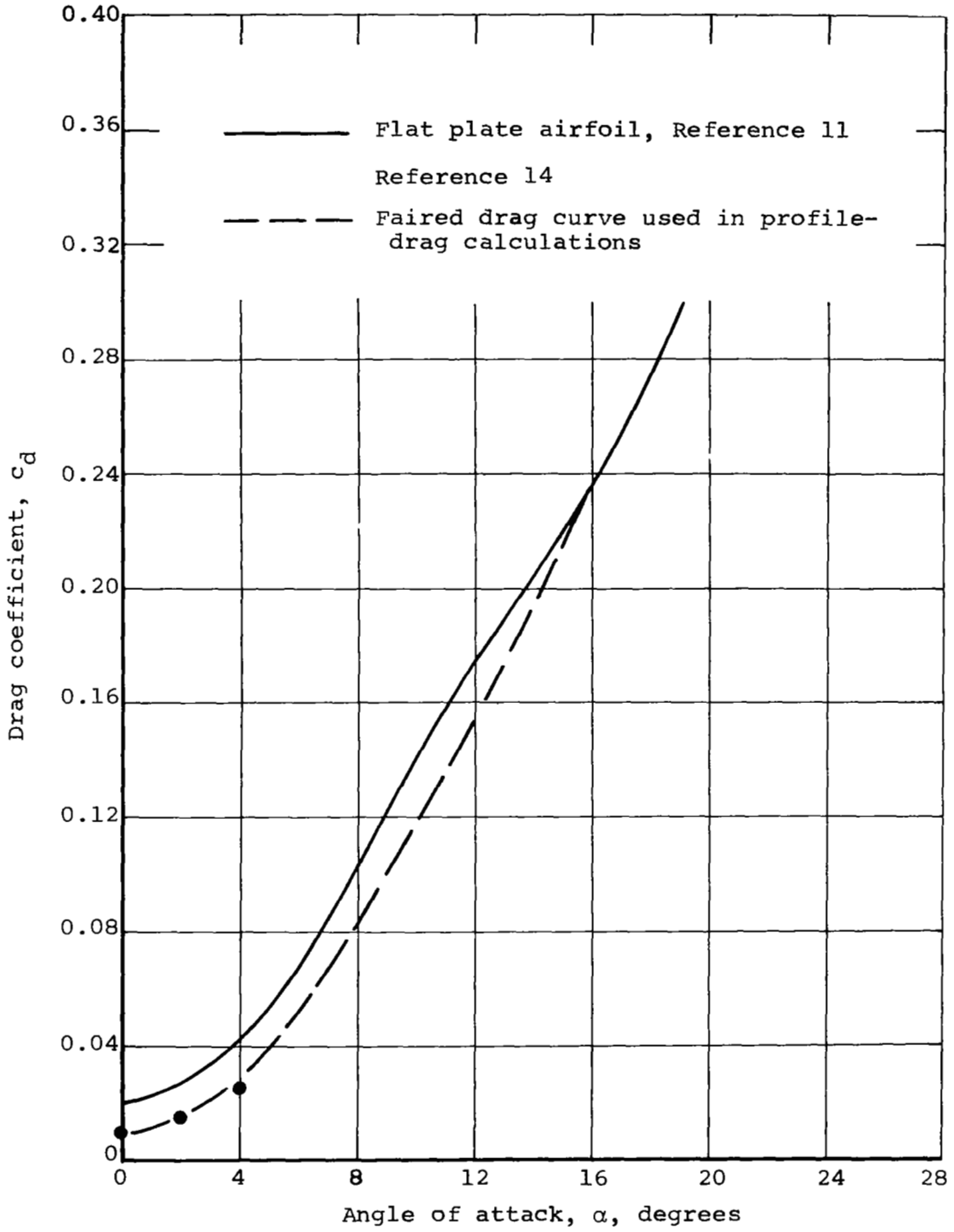

(c) Drag coefficient versus angle of attack; low angle of attack range.

Figure 3.- Concluded.

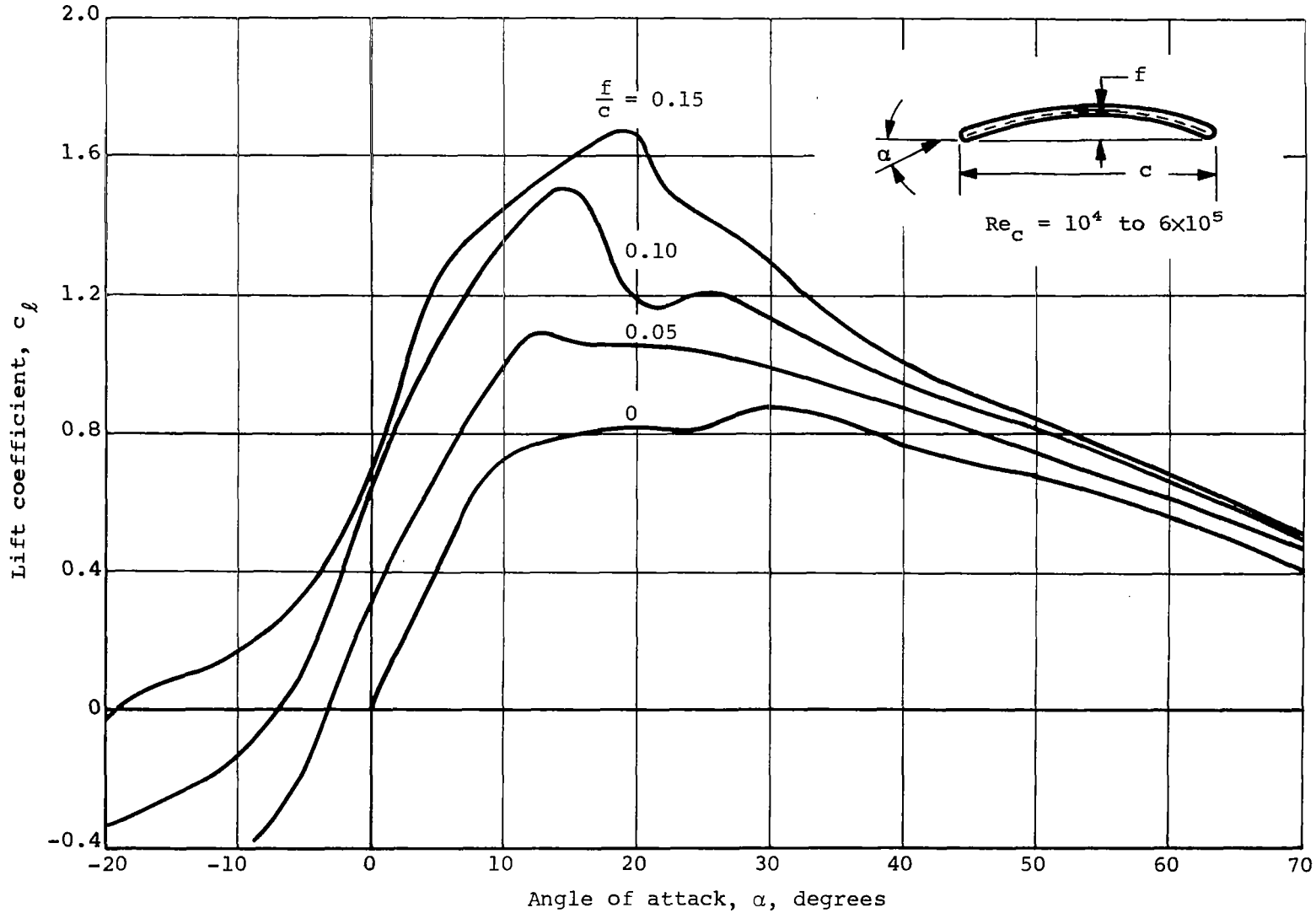

(a) Lift coefficient versus angle of attack.

Figure 4.- Section data for cambered rectangular plates of aspect ratio 5.

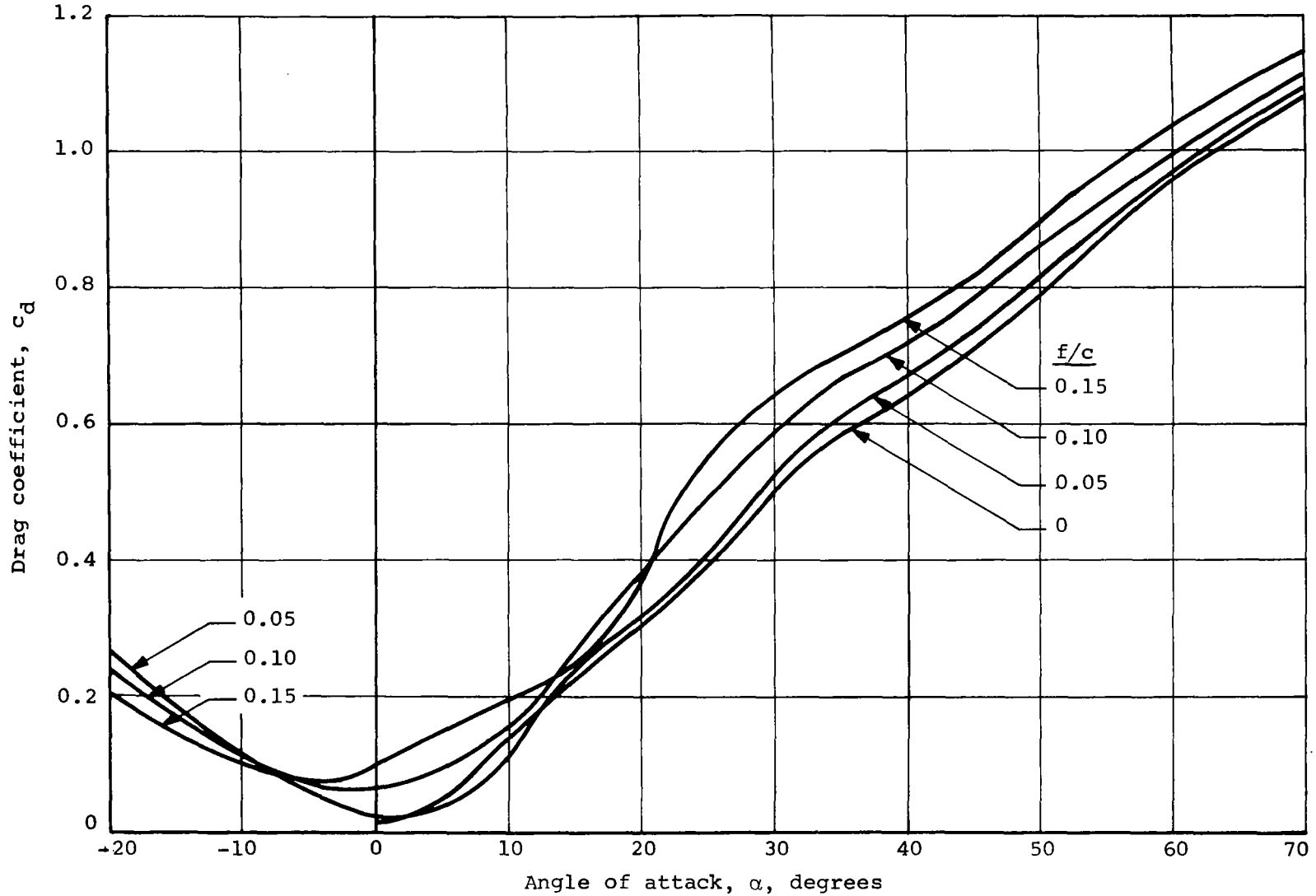

(b) Drag coefficient versus angle of attack.

Figure 4.- Concluded.

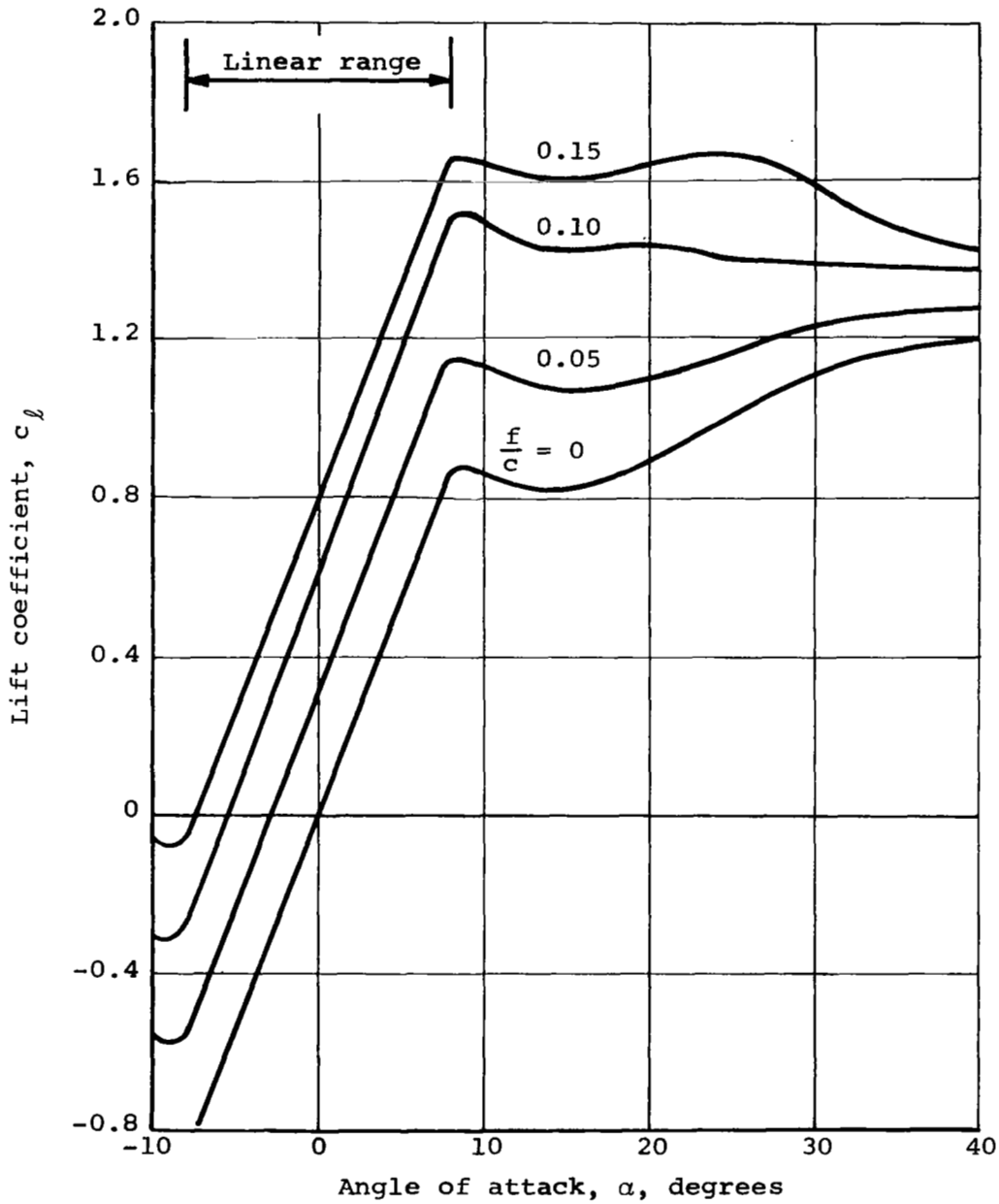

(a) Lift coefficient versus angle of attack.

Figure 5.- Constructed section data for cambered plates.

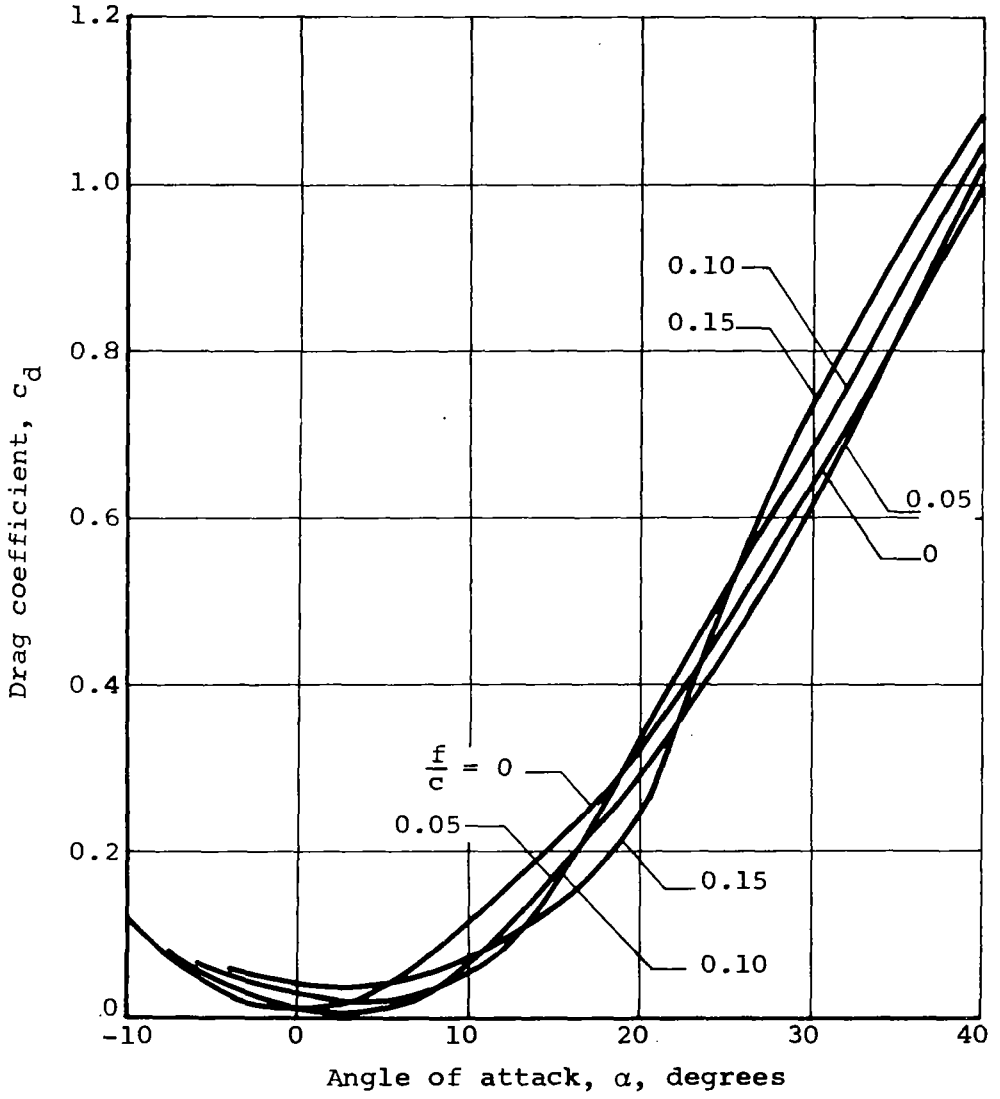

(b) Drag coefficient versus angle of attack.

Figure 5.- Continued.

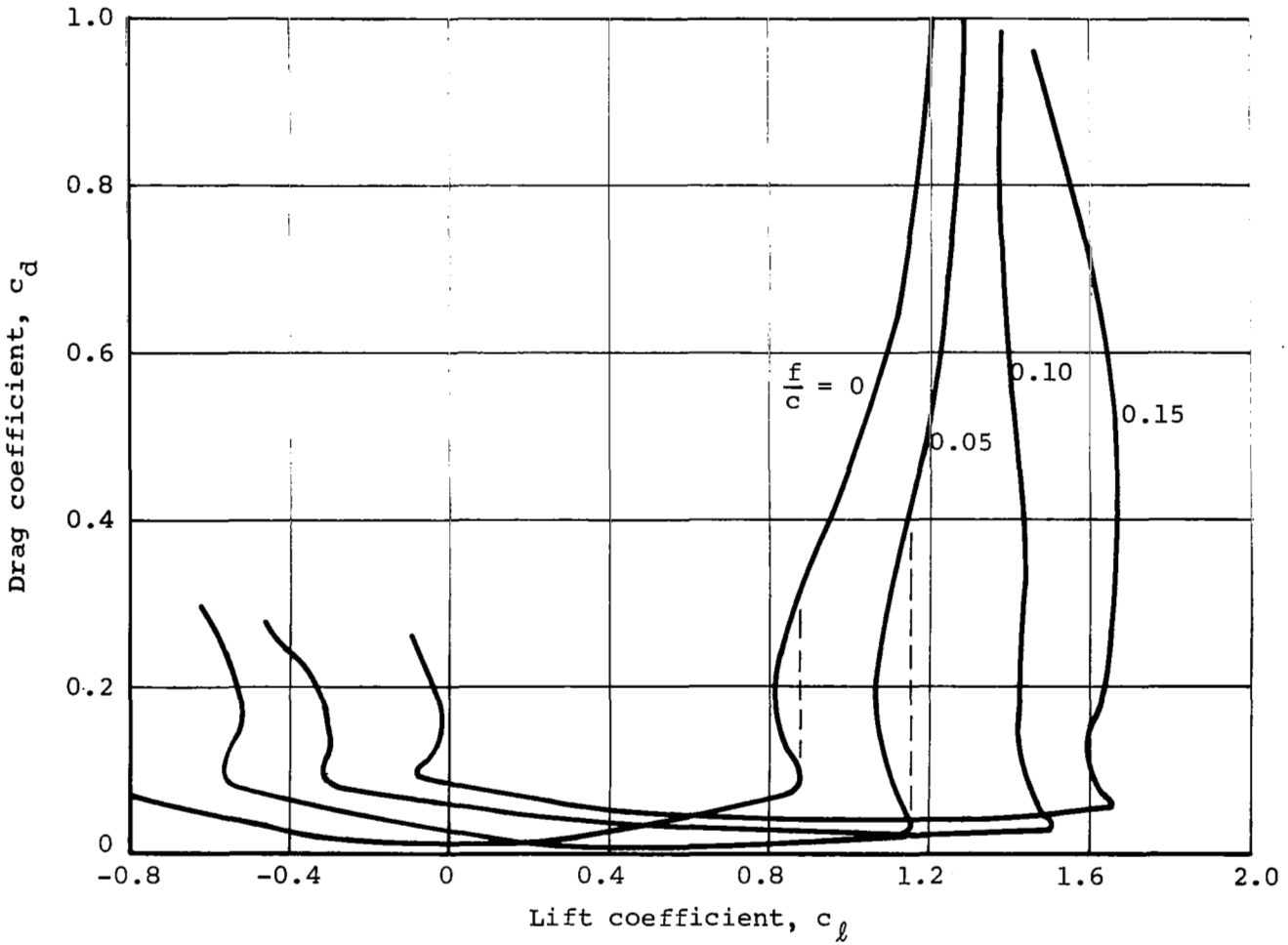

(c) Drag coefficient versus lift coefficient.

Figure 5.- Concluded.

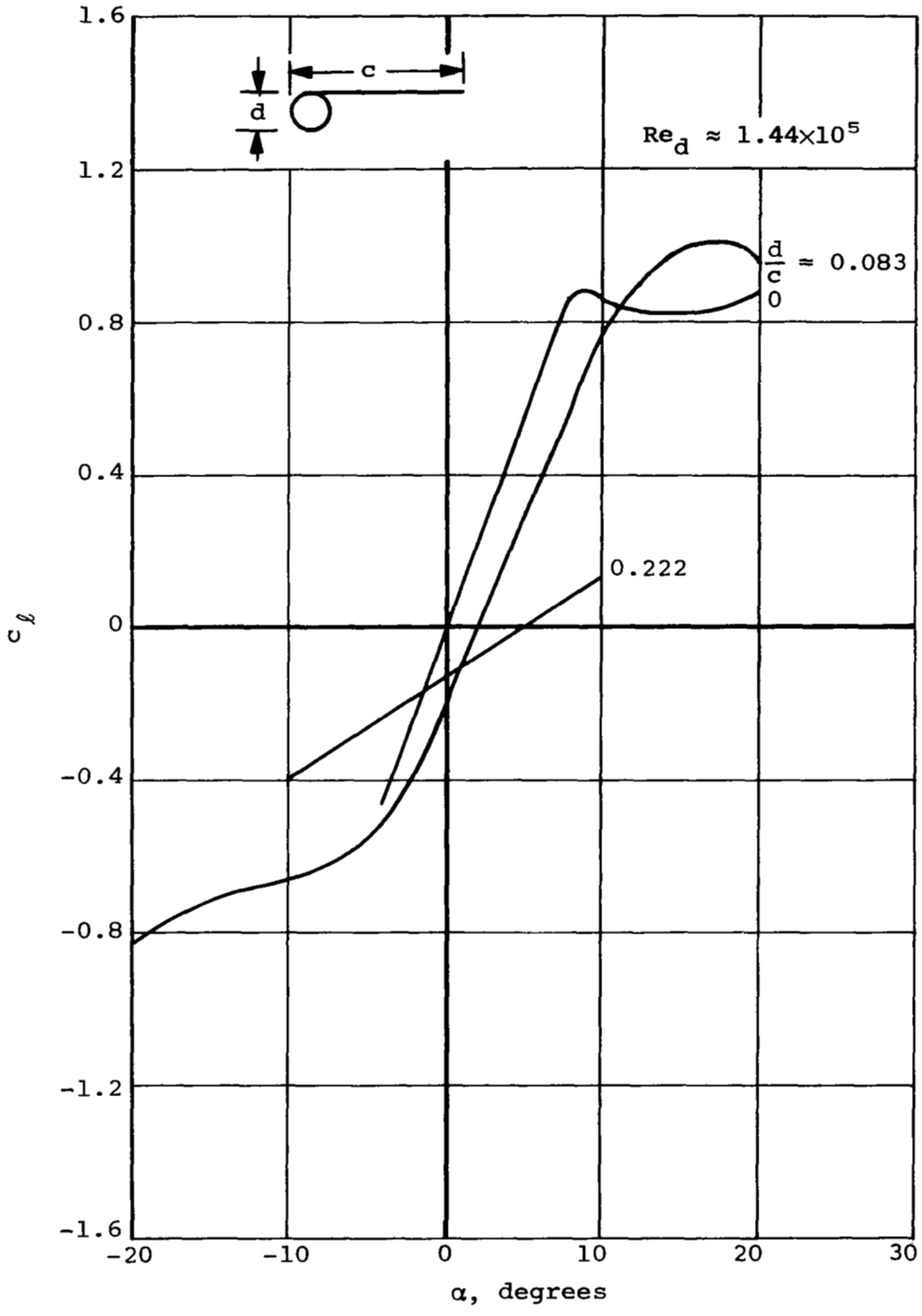

(a) Lift coefficient versus angle of attack.

Figure 6.- Section data for a splitter plate with top attachment for a subcritical Reynolds number.

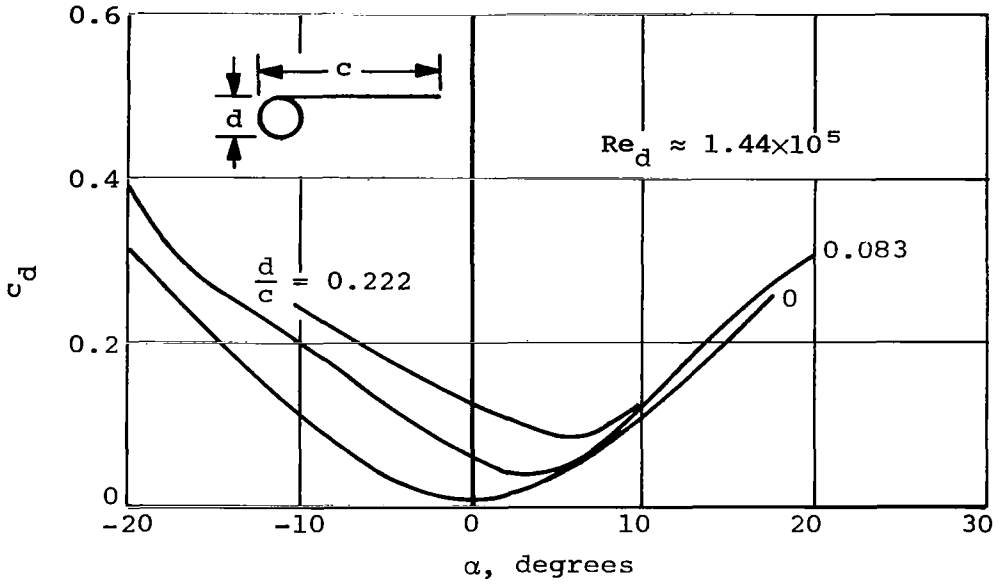

(b) Drag coefficient versus angle of attack.

Figure 6.- Concluded.

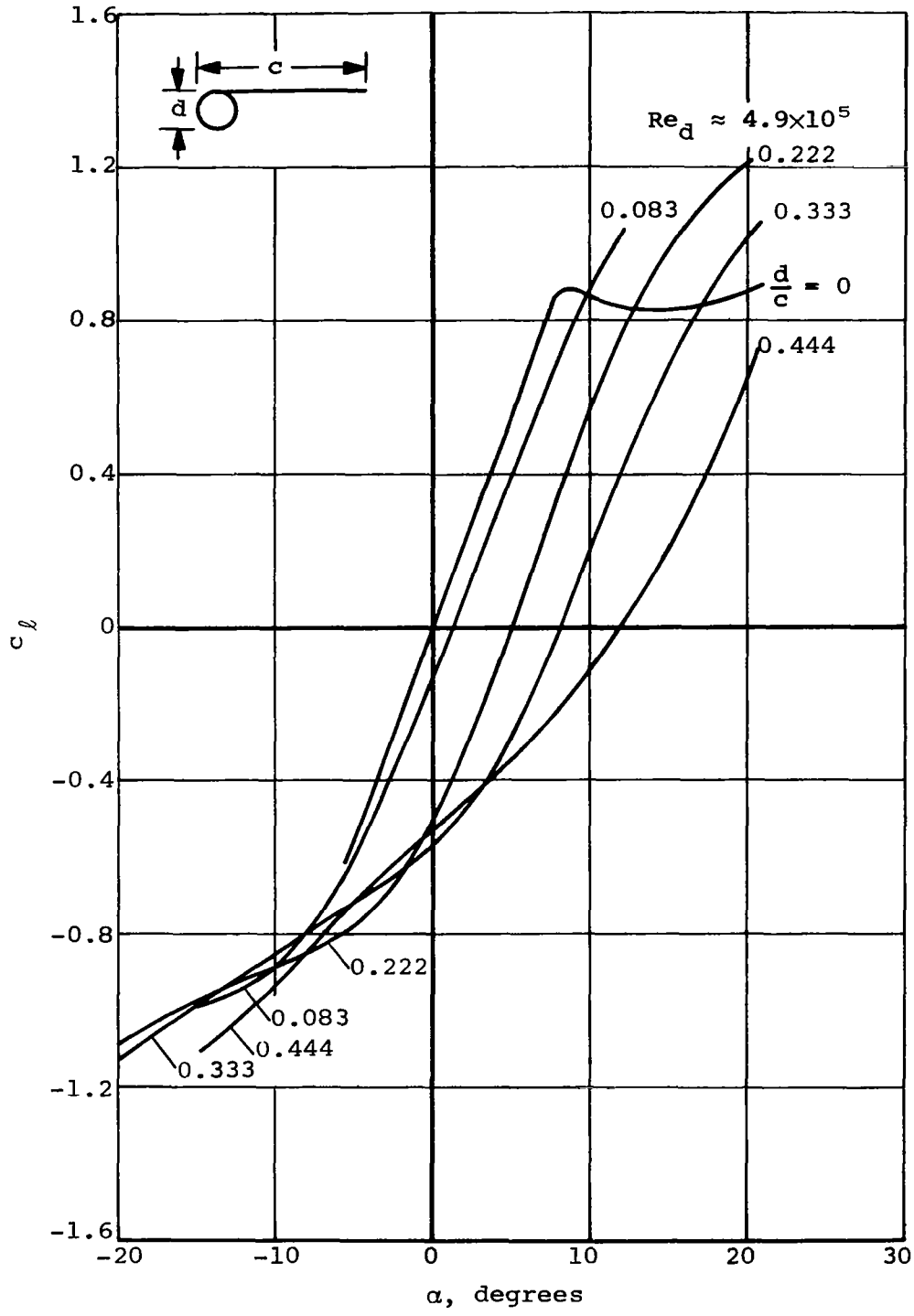

(a) Lift coefficient versus angle of attack.

Figure 7.- Section data for a splitter plate with top attachment for a supercritical Reynolds number.

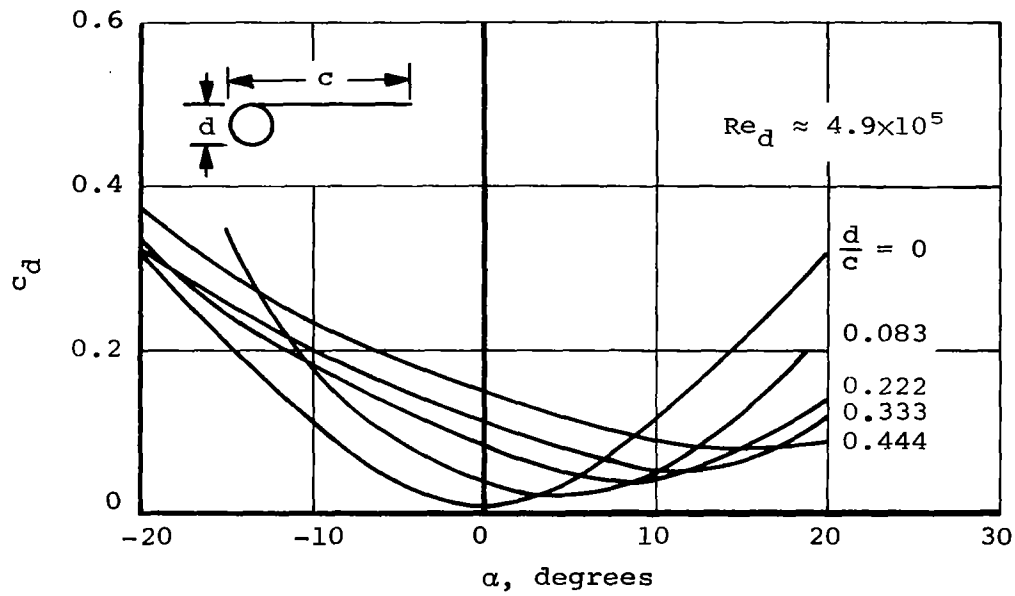

(b) Drag coefficient versus angle of attack.

Figure 7.- Concluded.

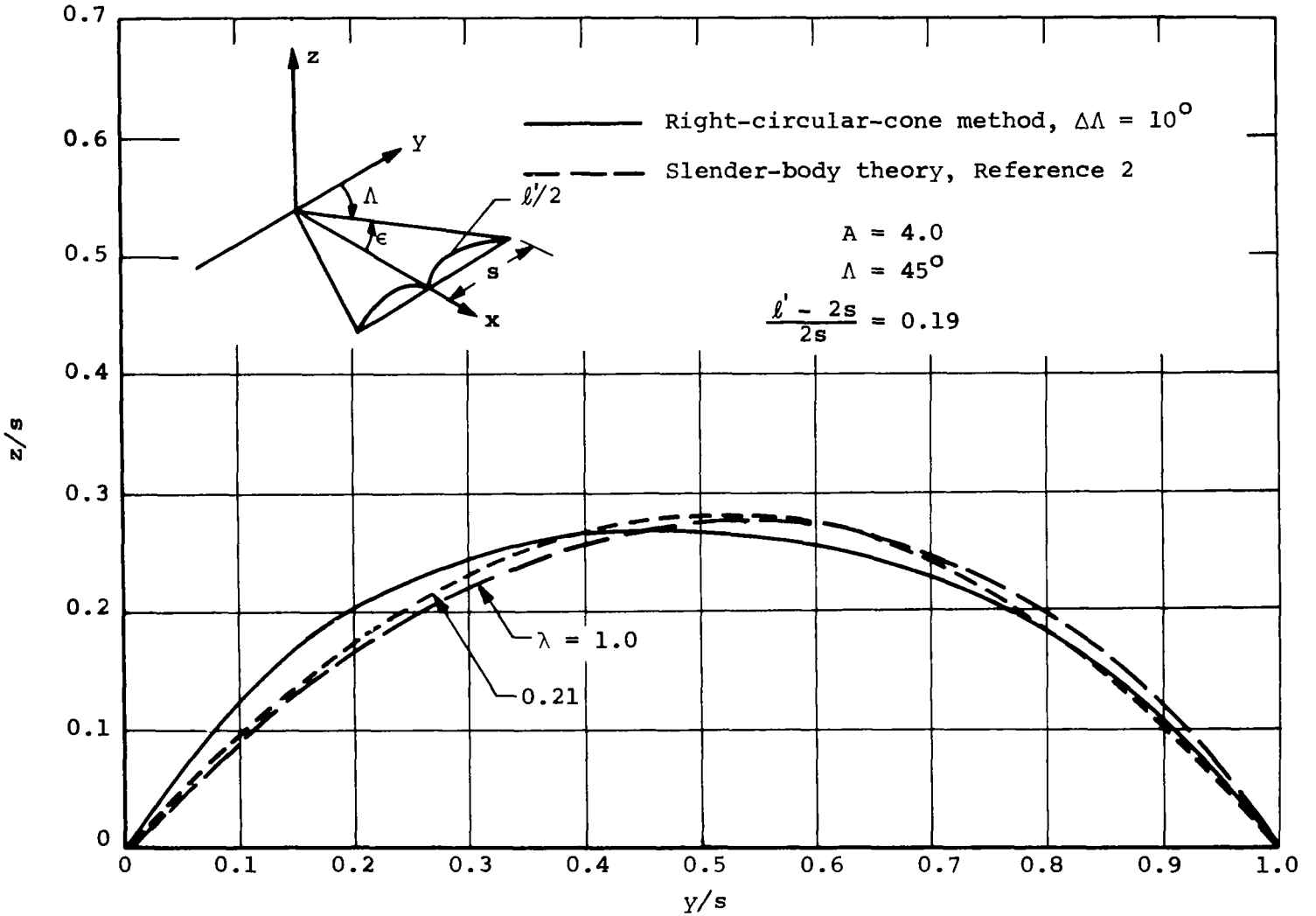

Figure 8.- Comparison of triangular wing trailing-edge shapes given by slender-body theory and the right-circular-cone method.

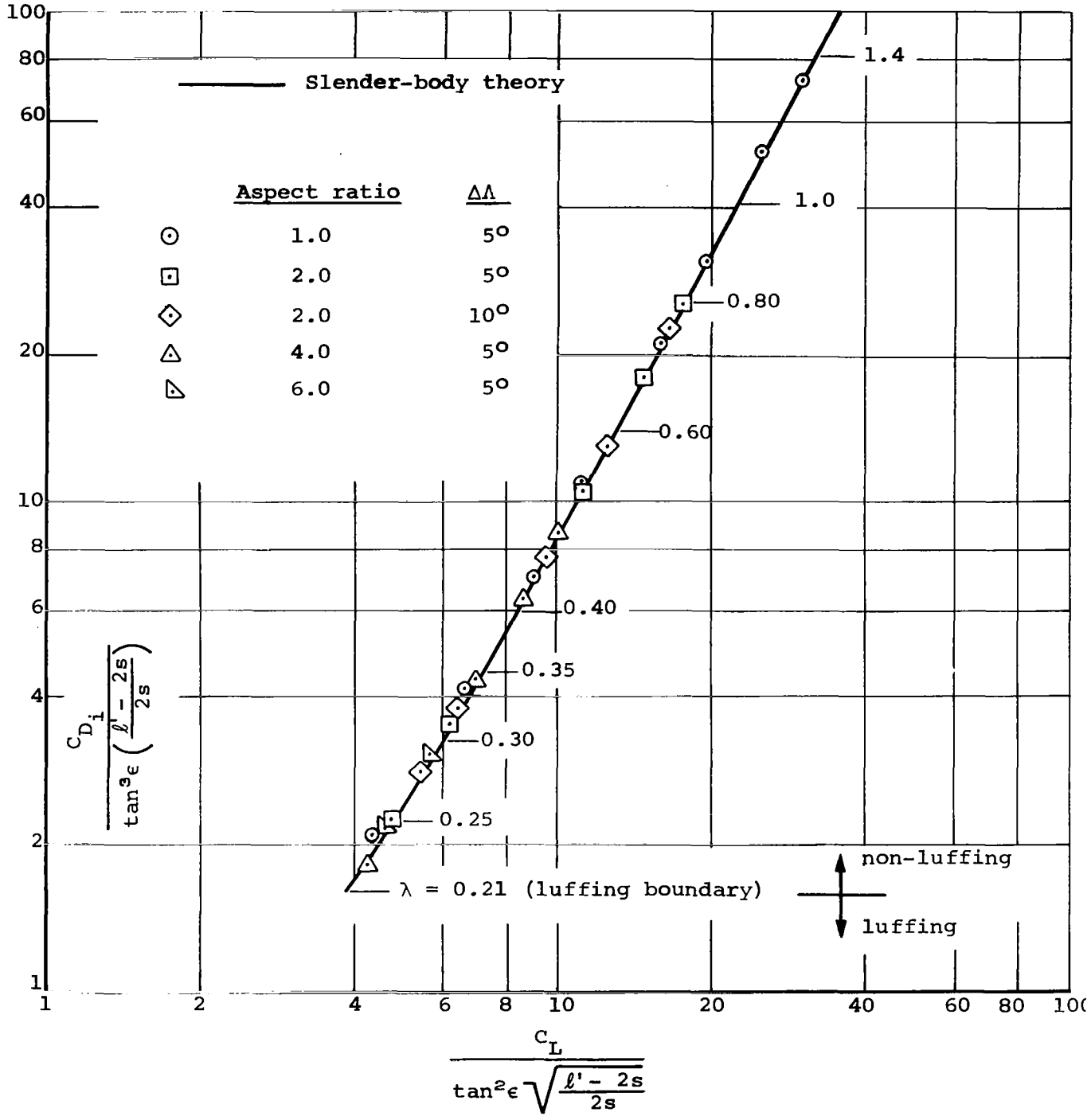

Figure 9.- Induced-drag correlation for triangular two-lobed parawings.

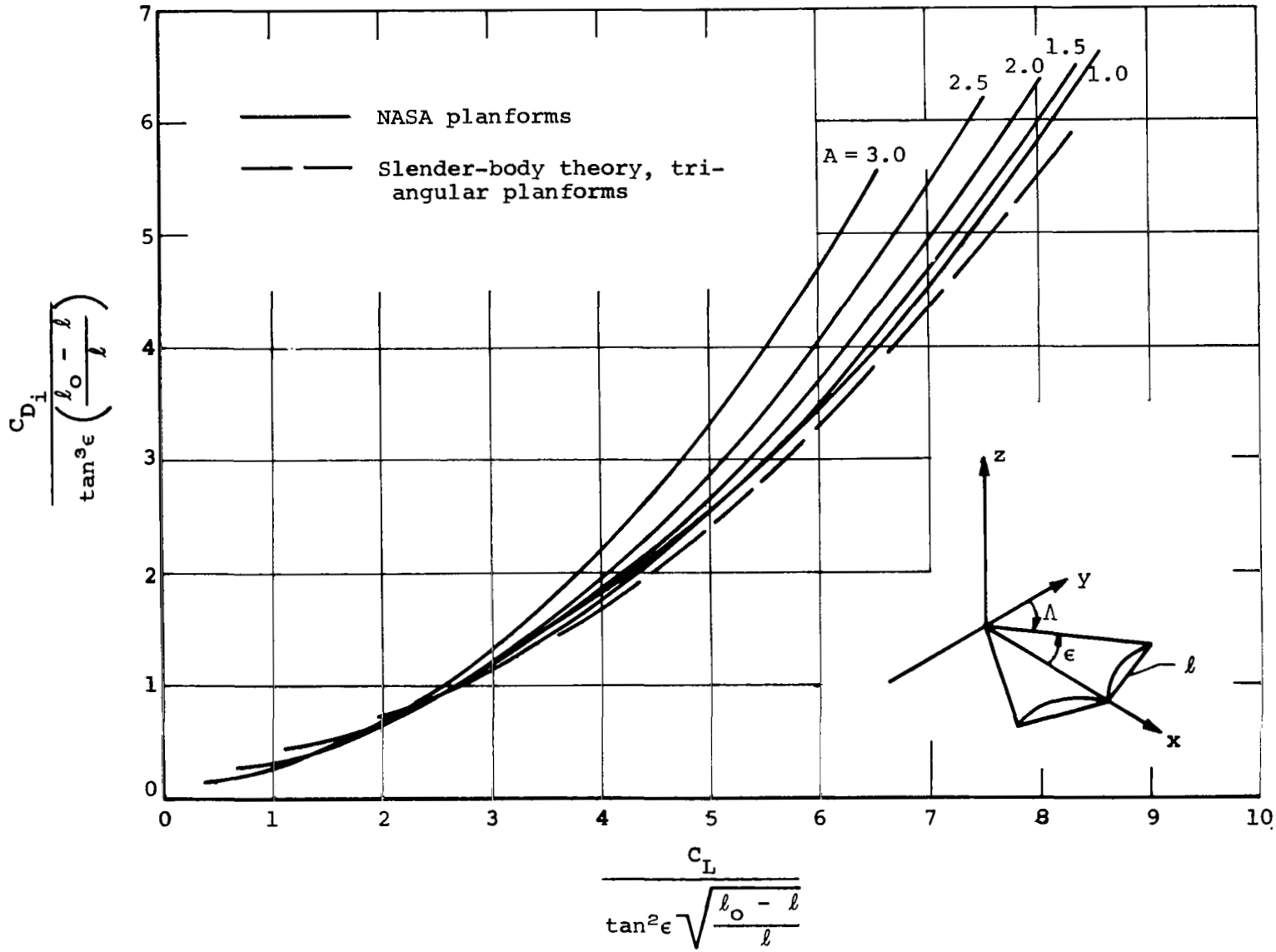

Figure 10.- Induced-drag correlation for two-lobed parawings of NASA planform.

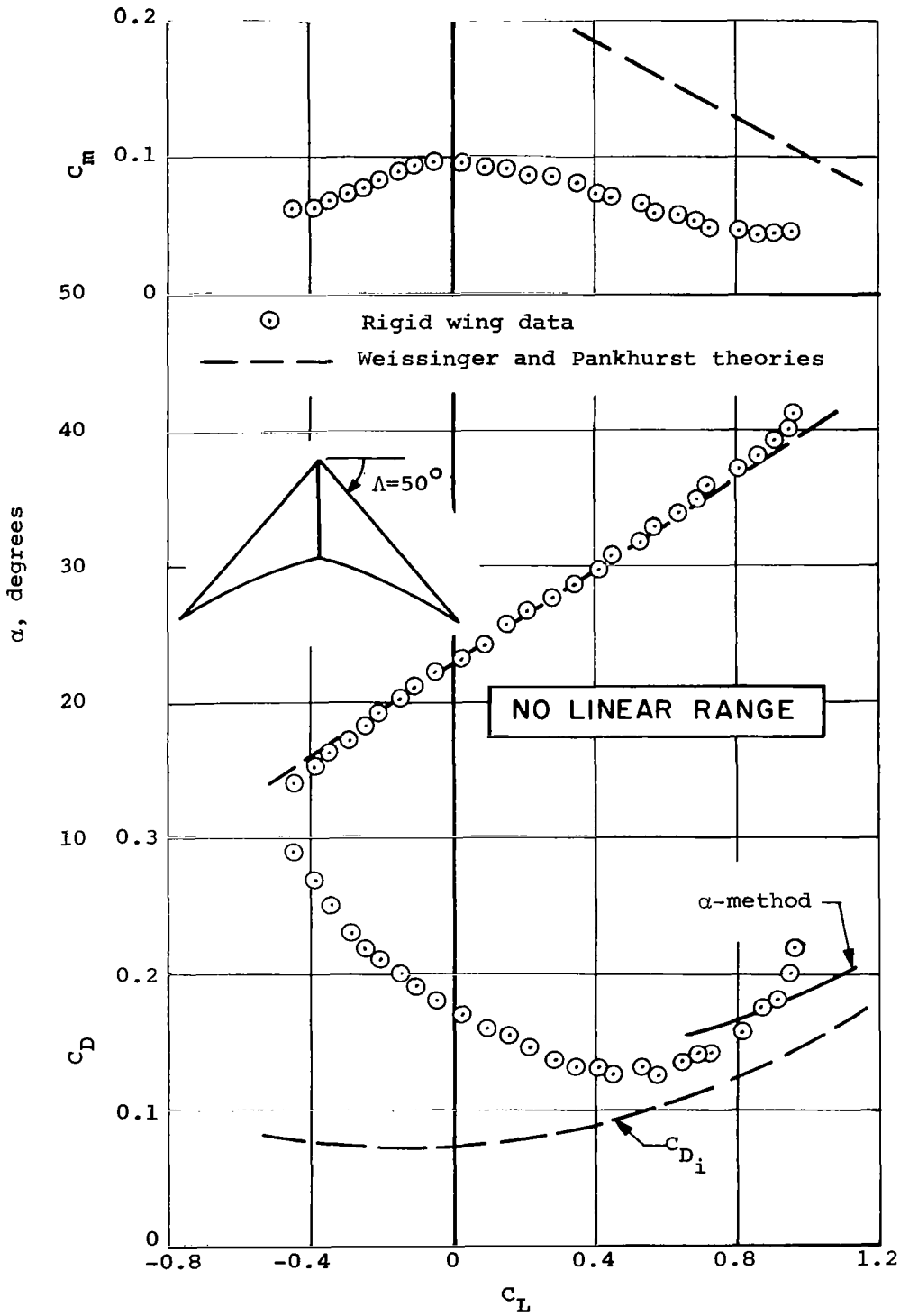

(a) Rigid Wing No. 1, $\Lambda_o = 35^o$, $2\beta = 157.8^o$.

Figure 11.- Comparison between experimental and predicted characteristics of aspect ratio 5.45 rigid wings, $\Lambda = 50^o$.

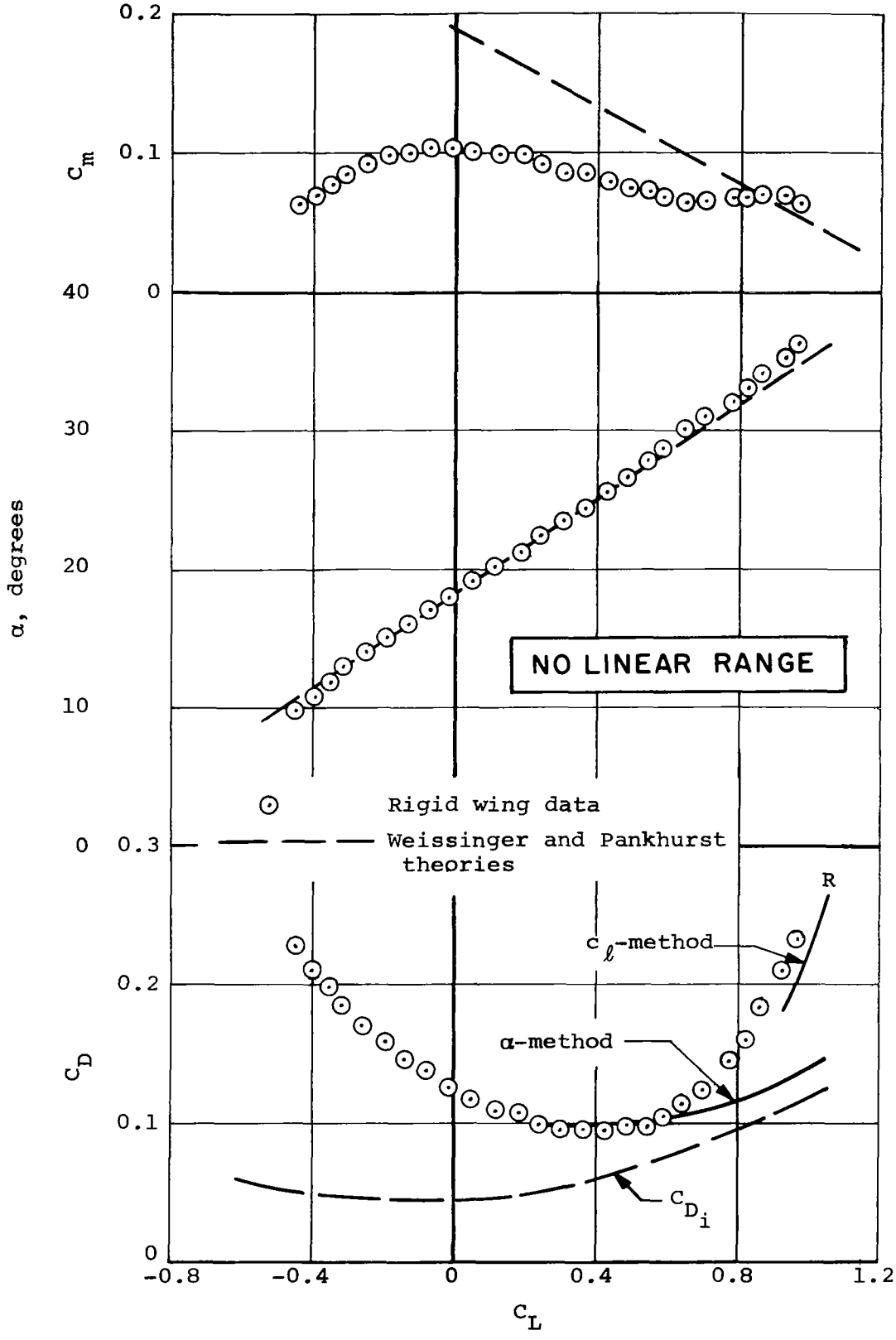

(b) Rigid Wing No. 2, $\Lambda = 40^\circ$, $2\beta = 135.1^\circ$.

Figure 11.- Continued.

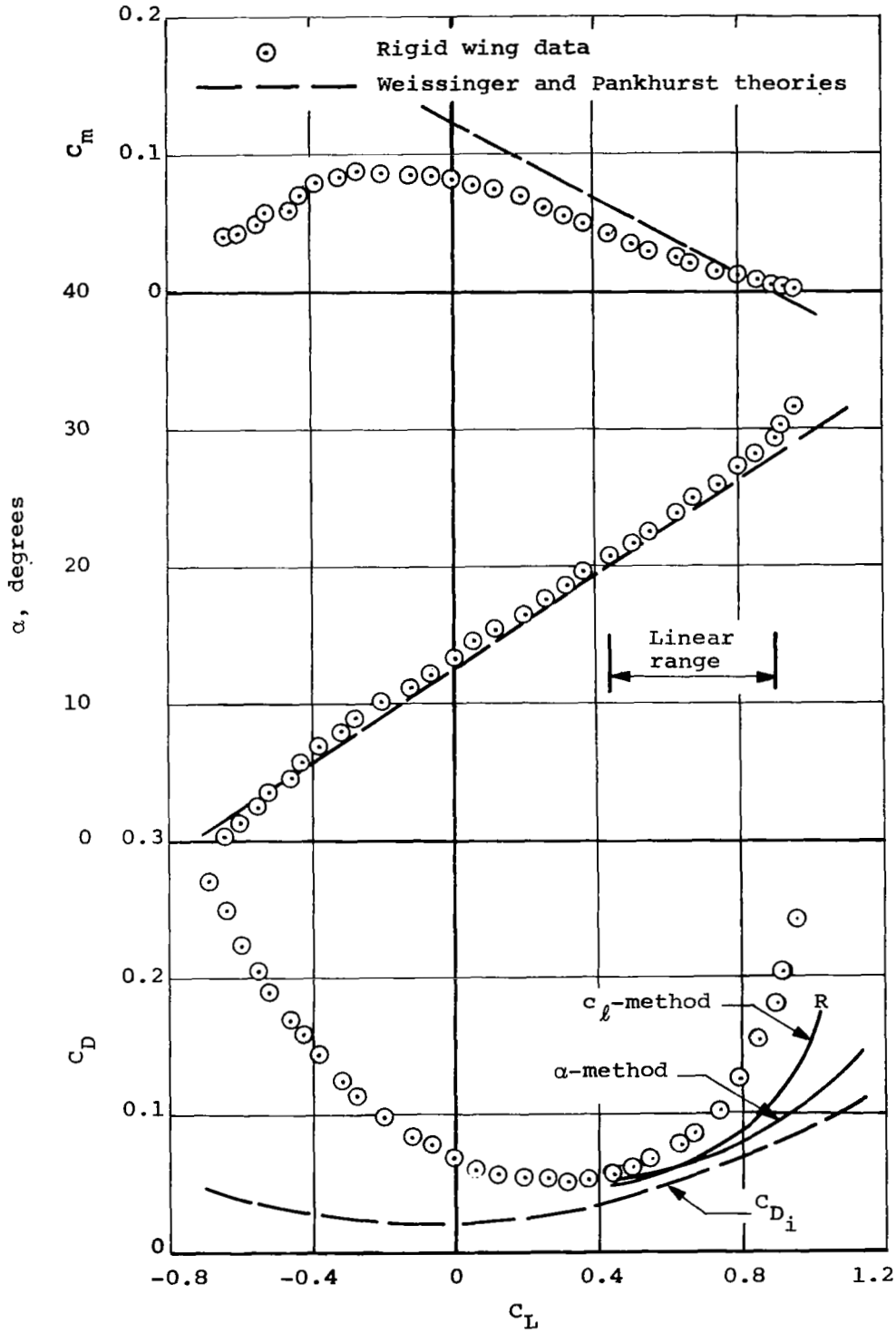

(c) Rigid Wing No. 3, $\Lambda_o = 45^o$, $2\beta = 102.9^o$.

Figure 11.- Continued.

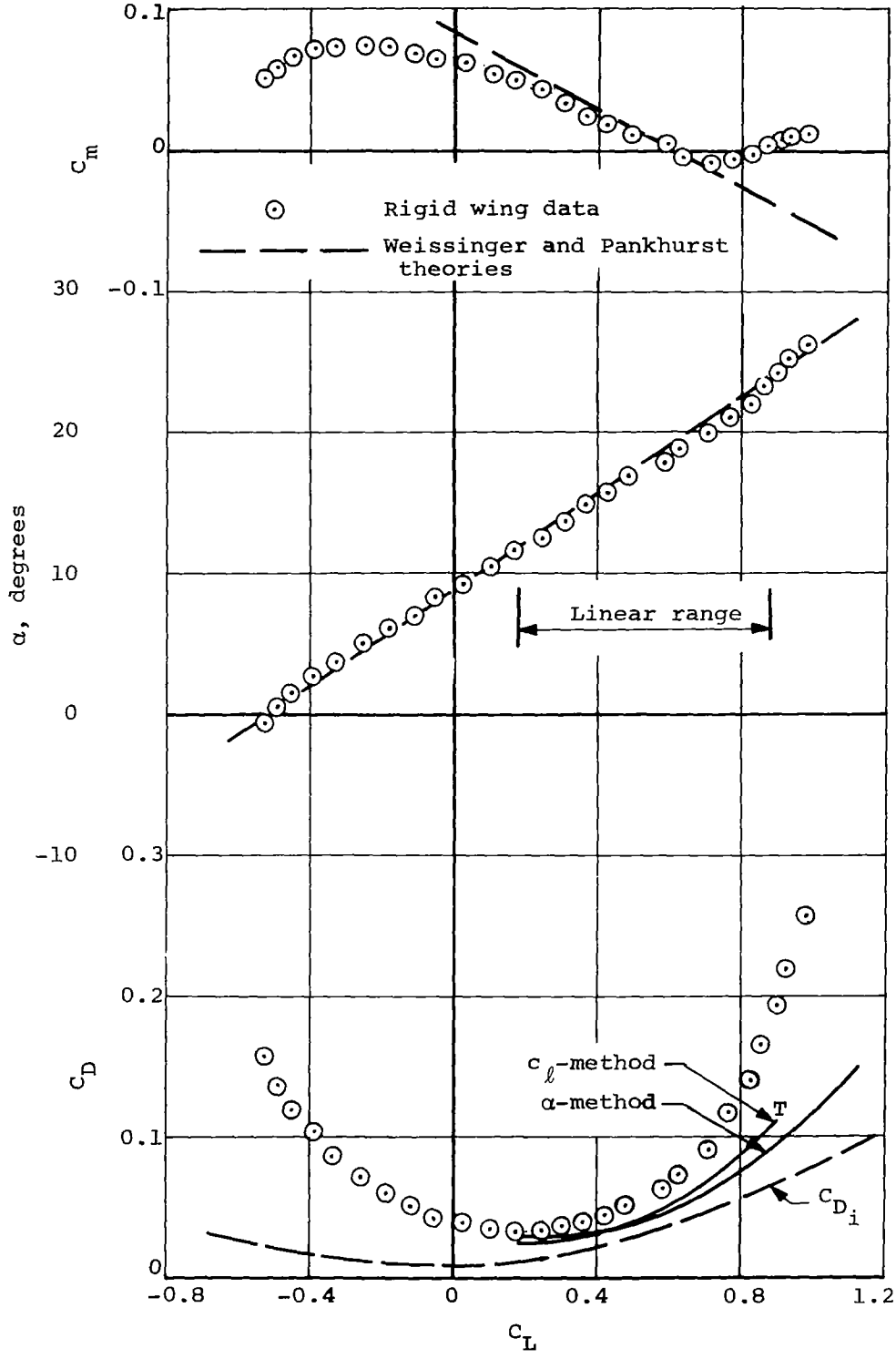

(d) Rigid Wing No. 4, $\Lambda_o = 47.5^o$, $2\beta = 79.2^o$.

Figure 11.- Continued.

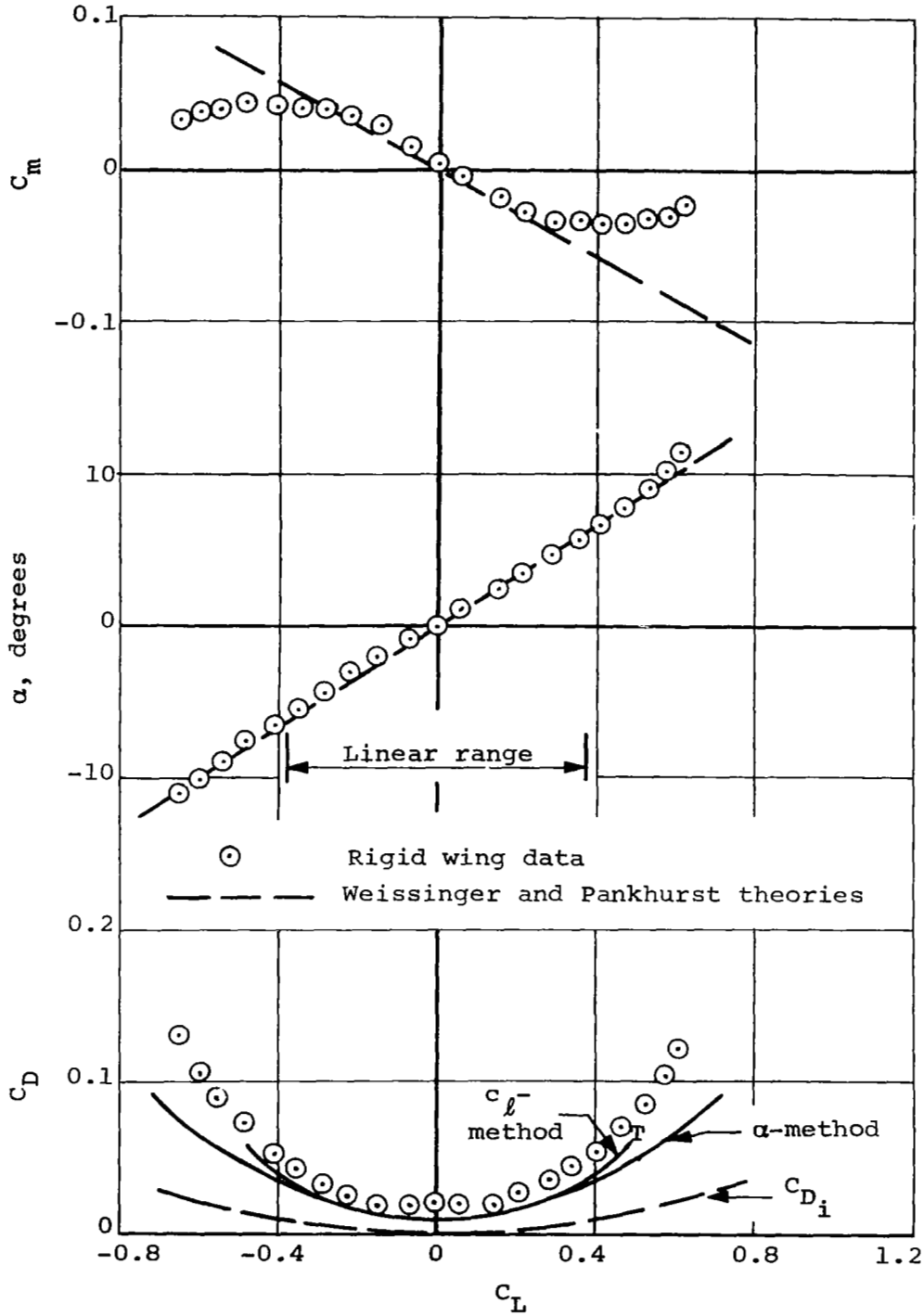

(e) Rigid Wing No. 5, $\Lambda_o = 50^o$.

Figure 11.- Concluded.

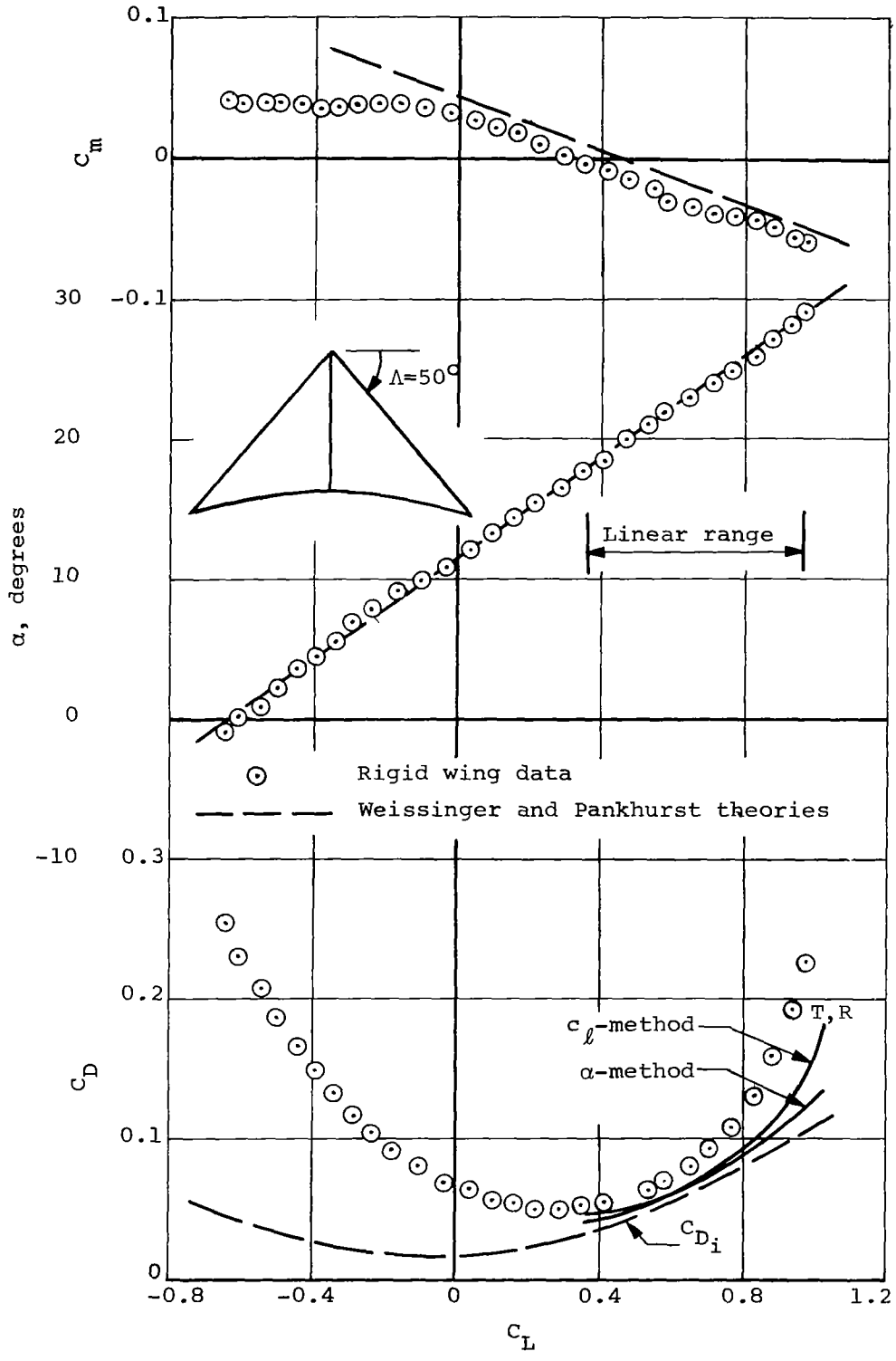

(a) Rigid Wing No. 6, $\Lambda_o = 45^\circ$, $2\beta = 102.9^\circ$.

Figure 12.- Comparison between experimental and predicted characteristics of aspect ratio 4.0 rigid wings, $\Lambda = 50^\circ$.

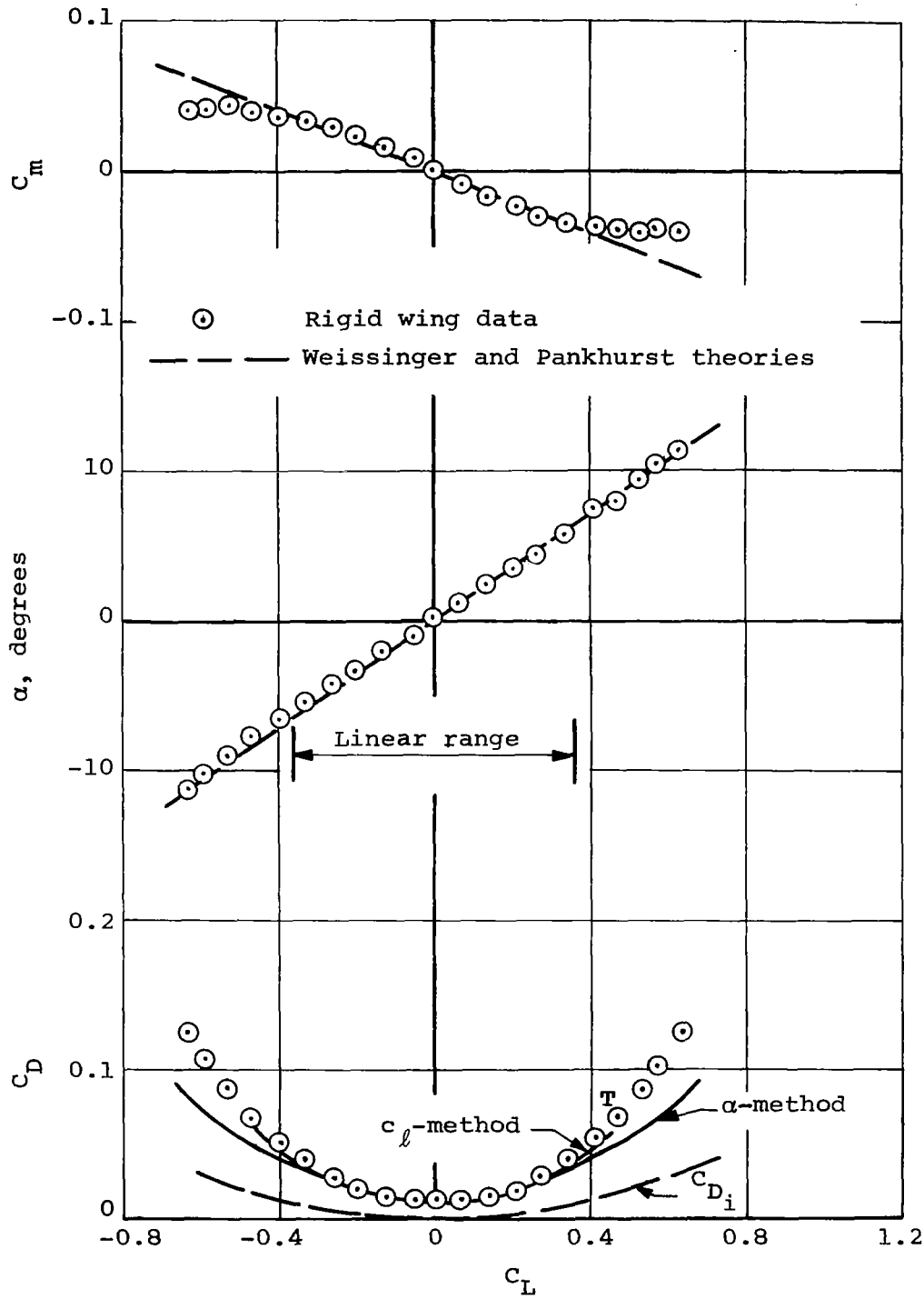

(b) Rigid Wing No. 7, $\Lambda_o = 50^\circ$.

Figure 12.- Concluded.

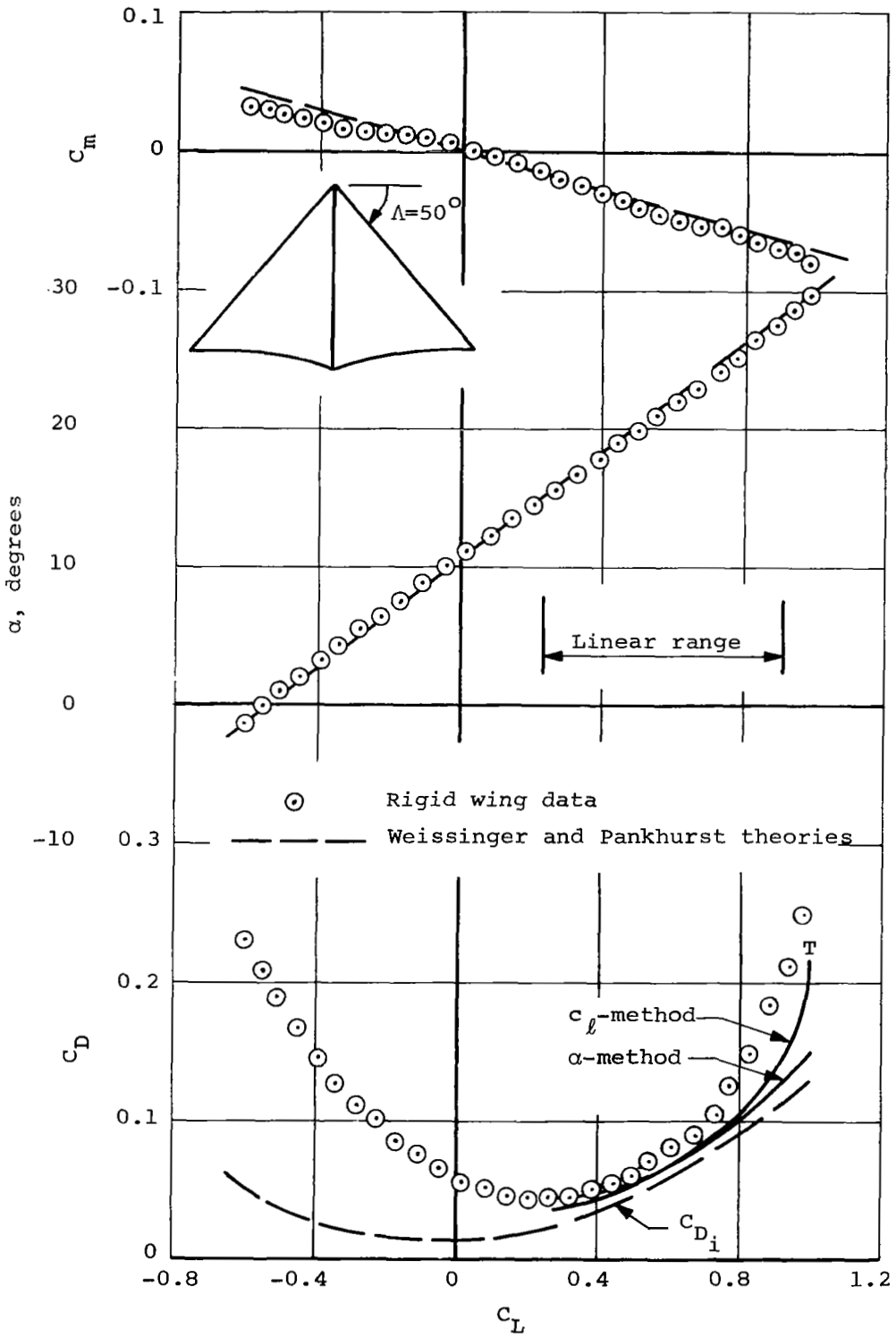

(a) Rigid Wing No. 8, $\Lambda_o = 45^o$, $2\beta = 102.9^o$.

Figure 13.- Comparison between experimental and predicted characteristics of aspect ratio 3.0 rigid wings, $\Lambda = 50^o$.

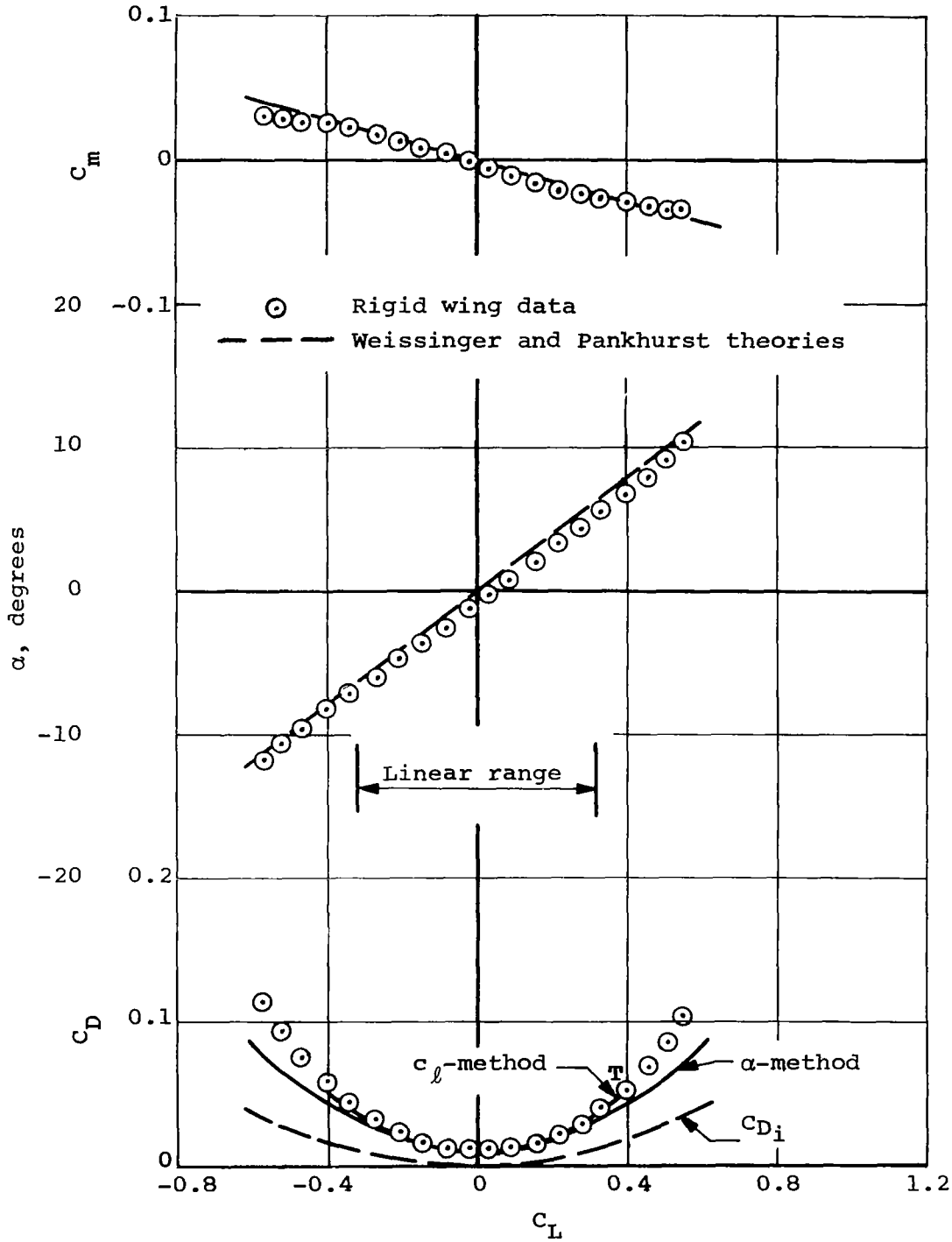

(b) Rigid Wing No. 9, $\Lambda_o = 50^o$.

Figure 13.- Concluded.

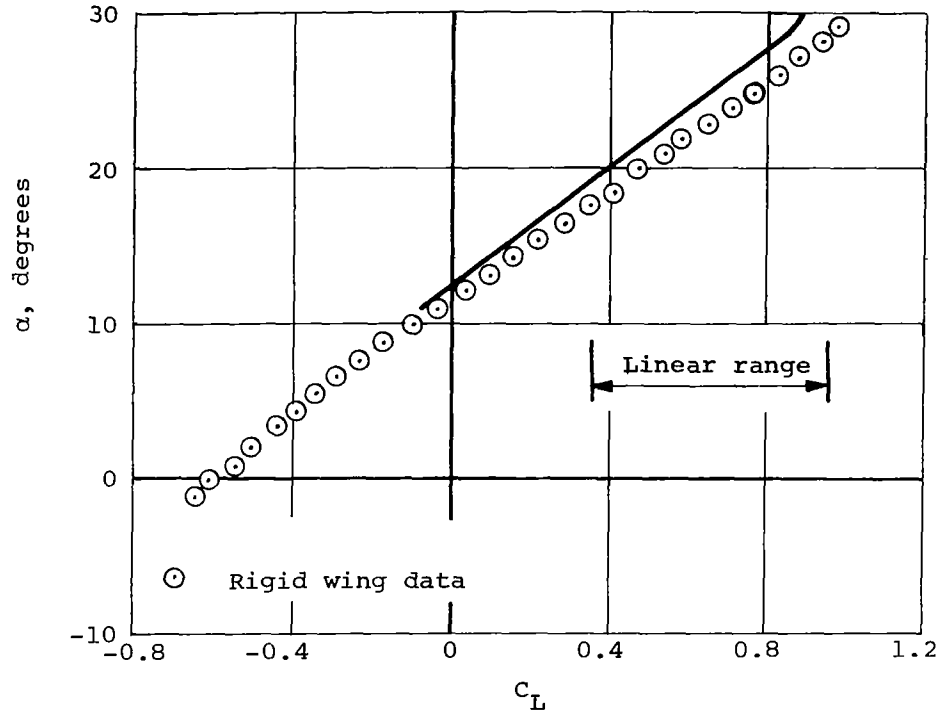

(a) Rigid Wing No. 6, $\Lambda_o = 45^o$, $2\beta = 102.9^o$.

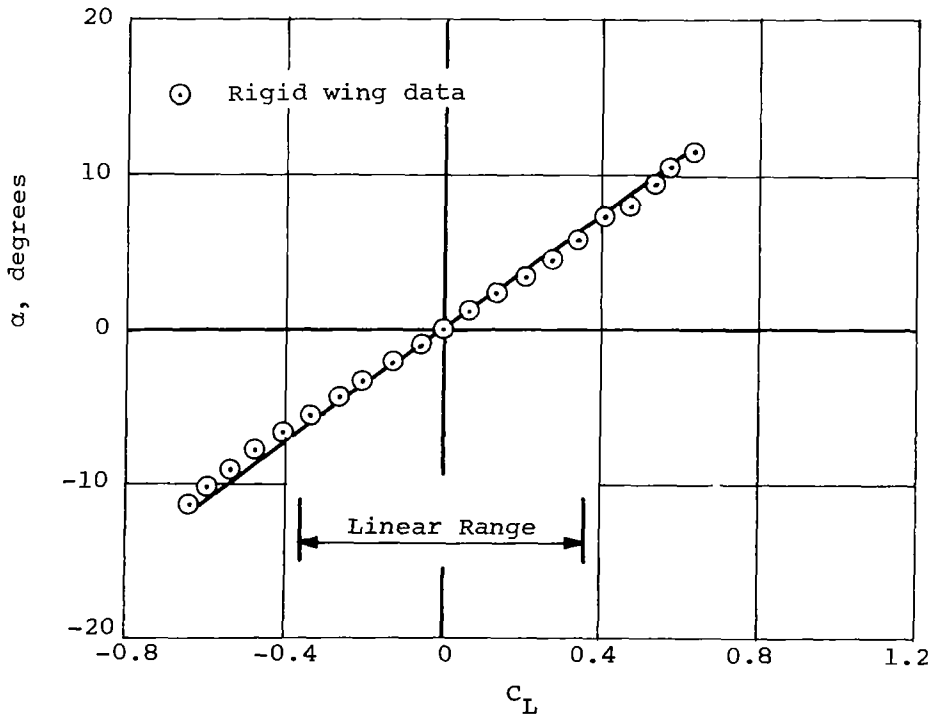

(b) Rigid Wing No. 7, $\Lambda_o = 50^o$.

Figure 14.- Comparison between experiment and theoretical characteristics computed by the iterative nonlinear method on aspect ratio 4.0 wings, $\Lambda = 50^o$.

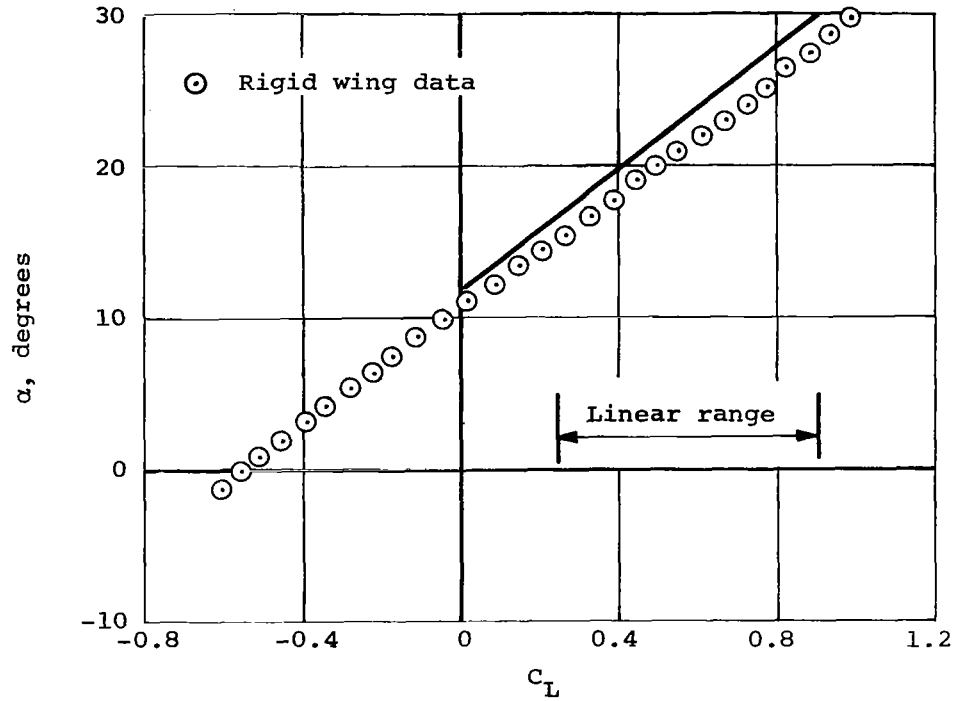

(a) Rigid Wing No. 8, $\Lambda_o = 45^o$, $2\beta = 102.9^o$.

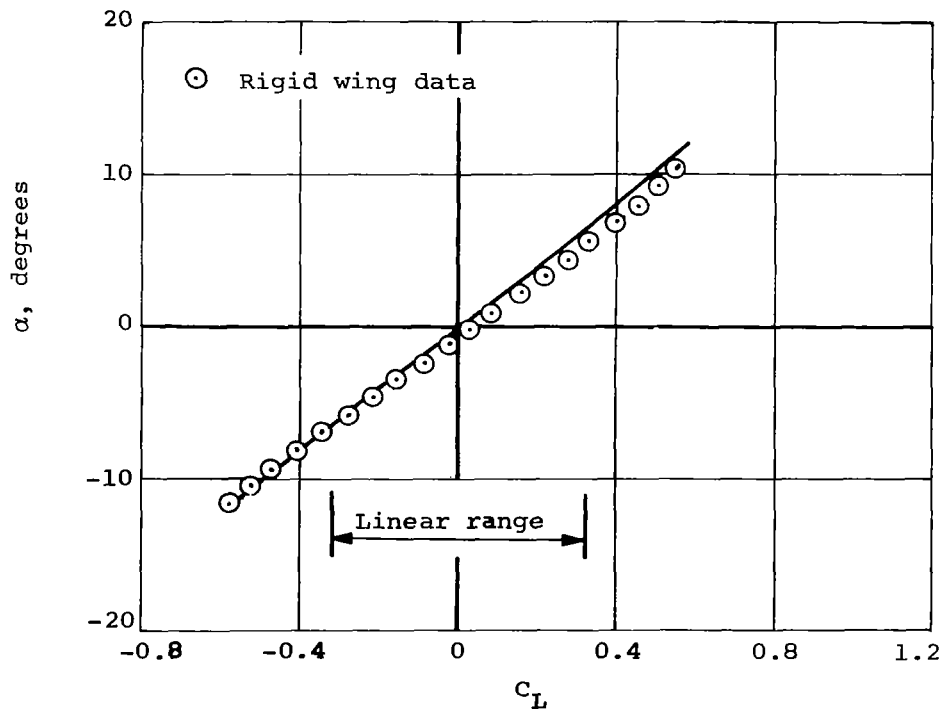

(b) Rigid Wing No. 9, $\Lambda_o = 50^o$.

Figure 15.- Comparison between experiment and theoretical characteristics computed by the iterative nonlinear method on aspect ratio 3.0 rigid wings, $\Lambda = 50^o$.

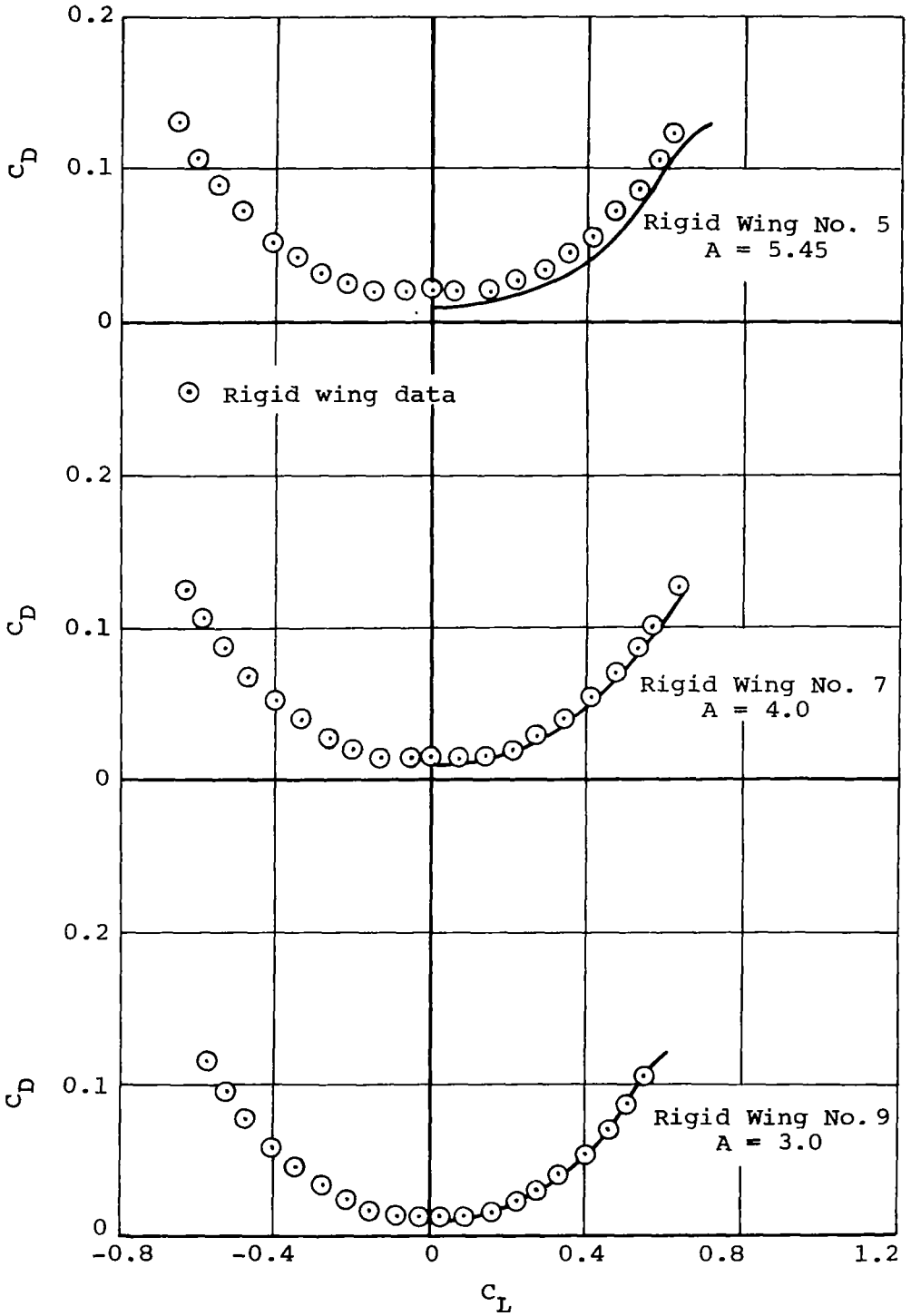

Figure 16.- Comparison of measured drag for swept uncambered untwisted wings with drag predicted by the Polhamus method.

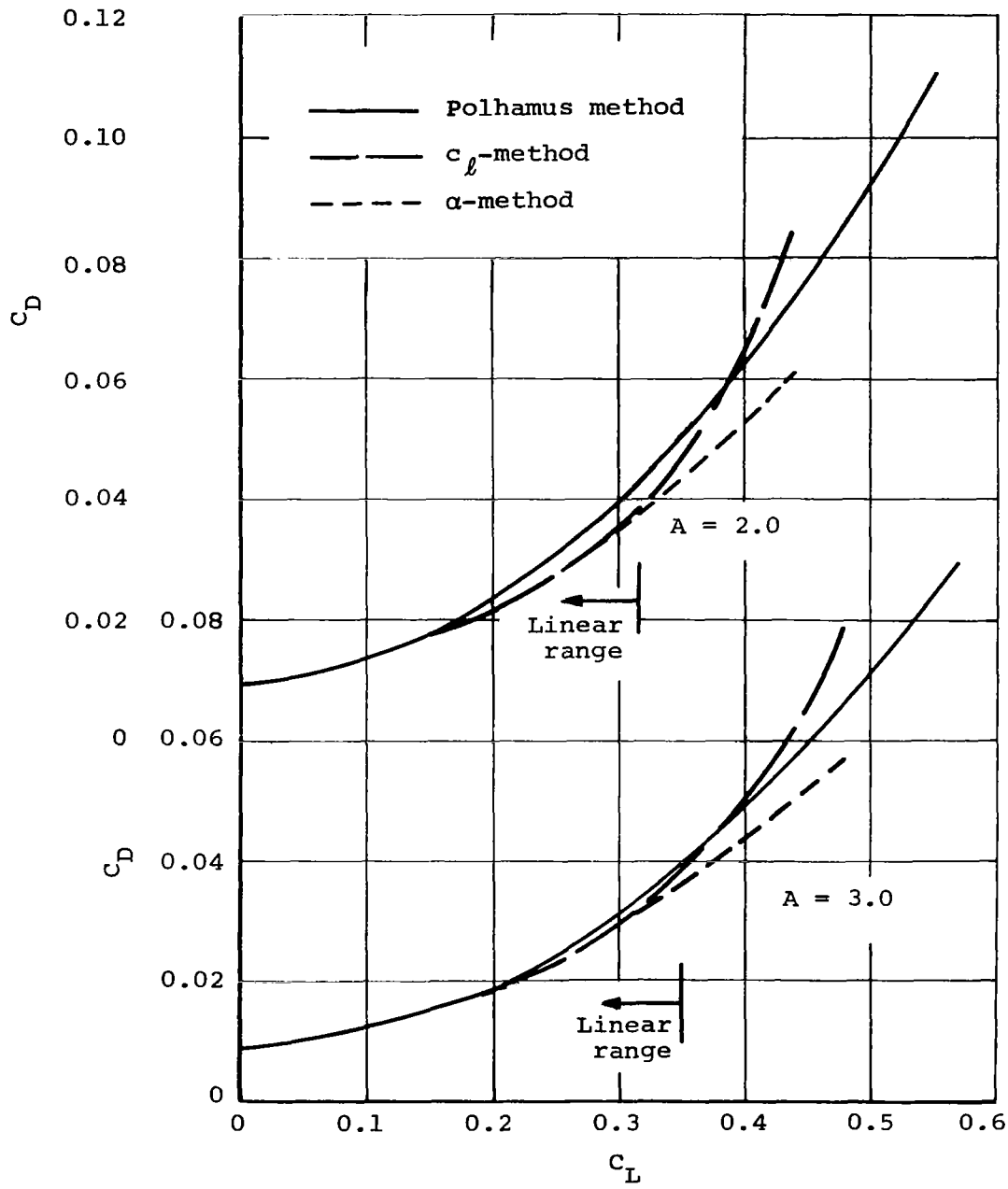

(a) Aspect ratio 2.0 and 3.0.

Figure 17.- Comparison of profile-drag prediction methods for flat wings of NASA planform.

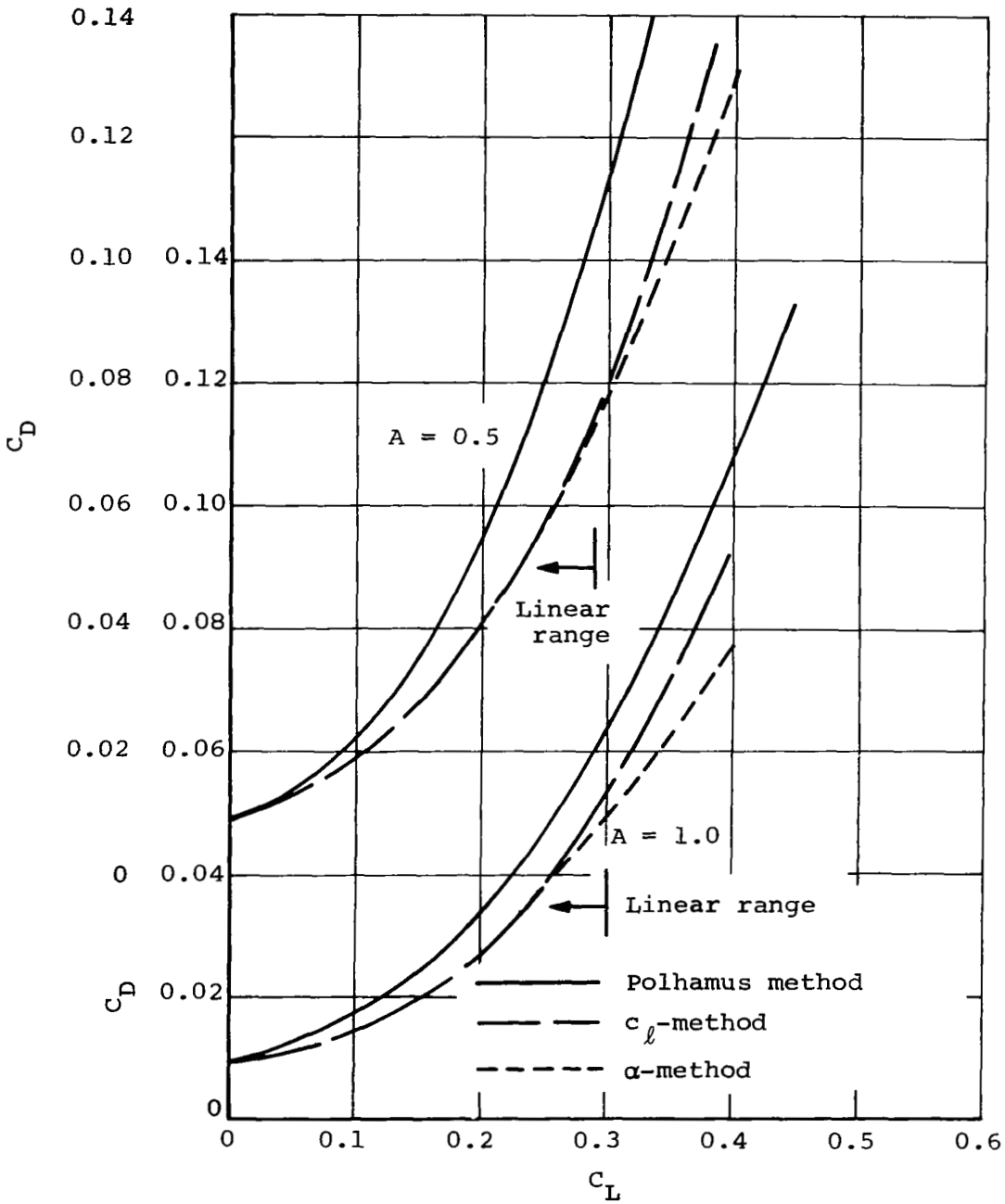

(b) Aspect ratio 0.5 and 1.0.

Figure 17.- Concluded.

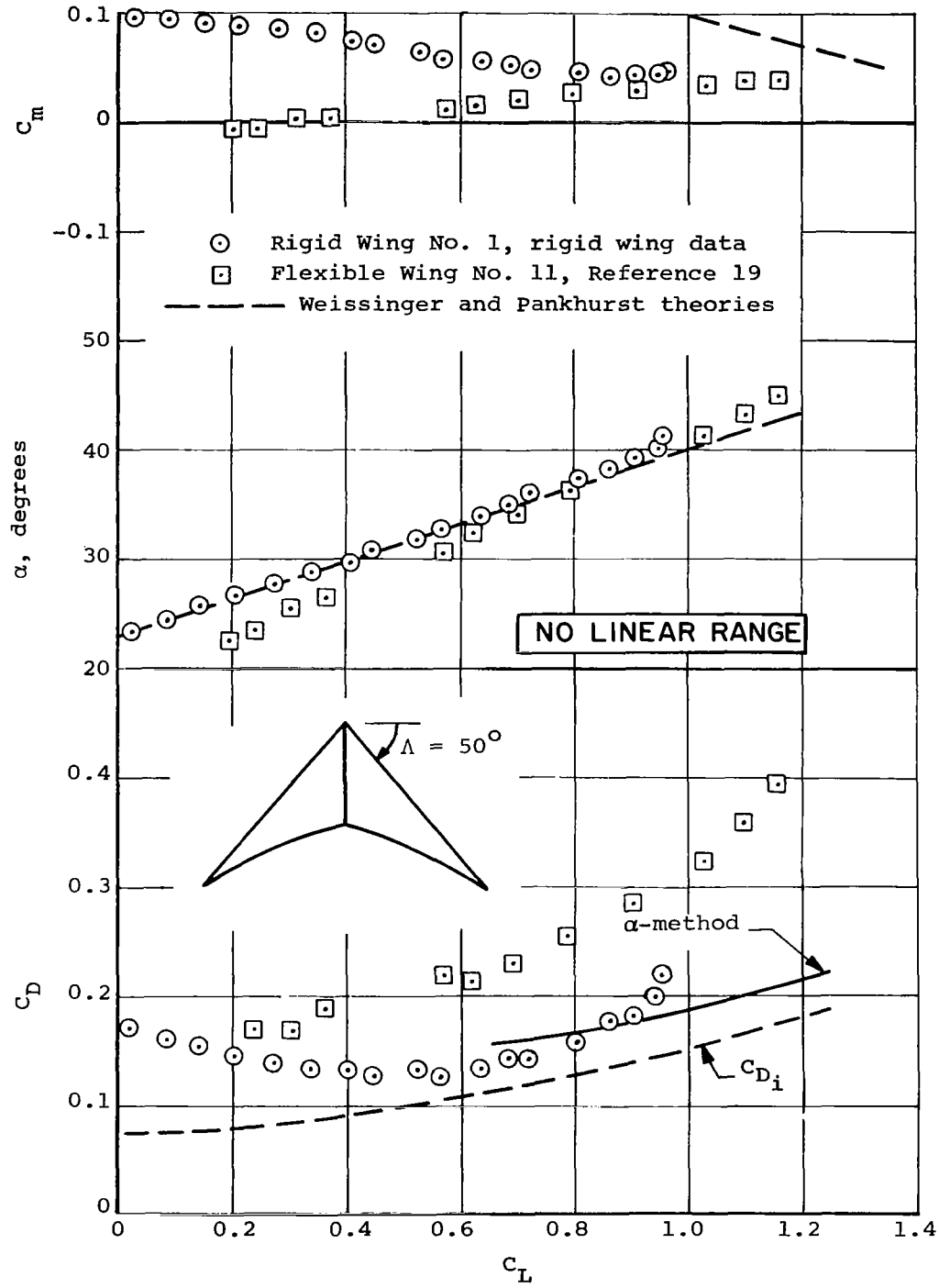

(a) $\Lambda_o = 35^o$.

Figure 18.- Comparison between experimental and predicted characteristics of rigid and flexible wings of aspect ratio 5.45, $\Lambda = 50^o$.

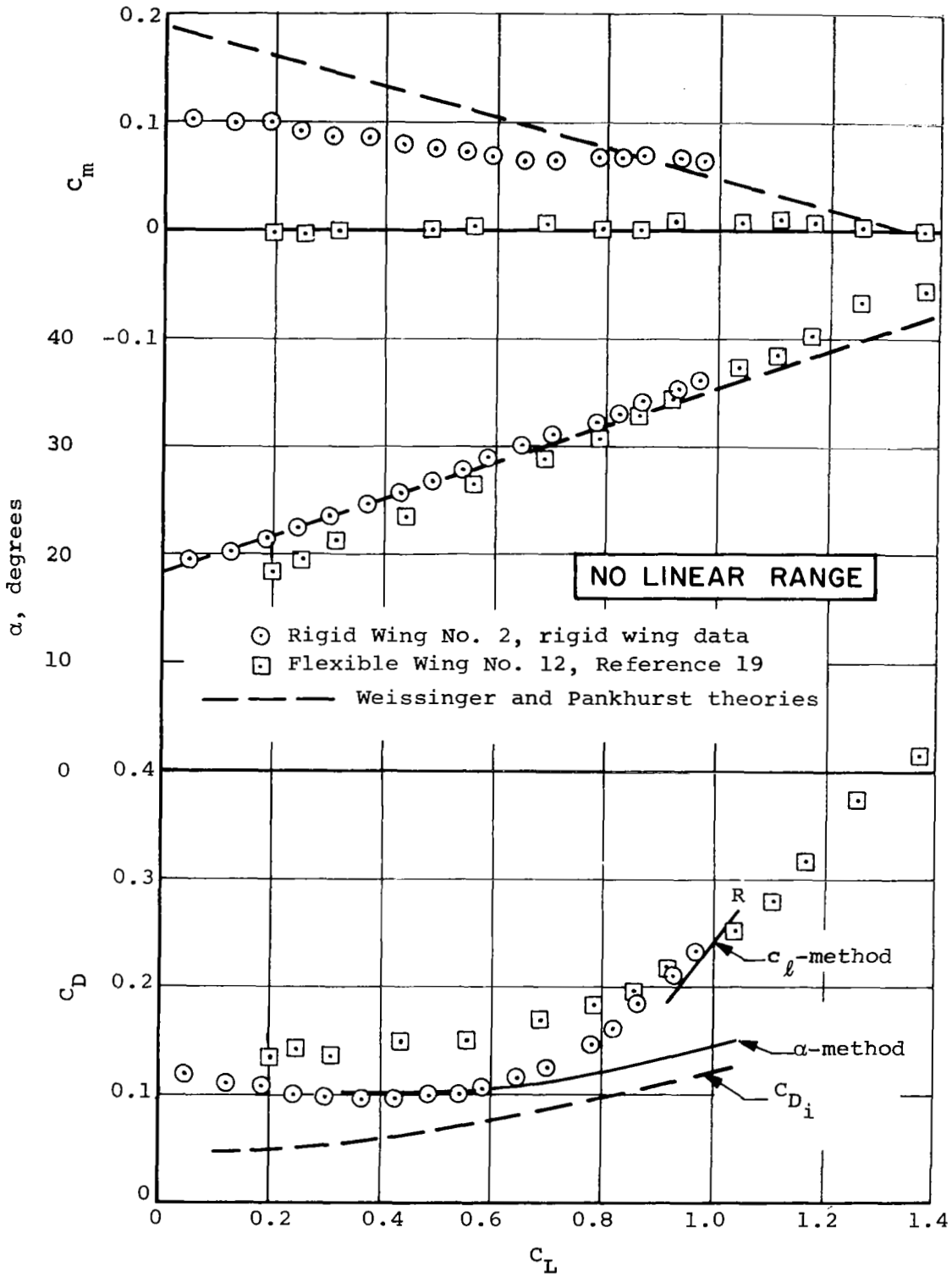

(b) $\Lambda_o = 40^o$.

Figure 18.- Continued.

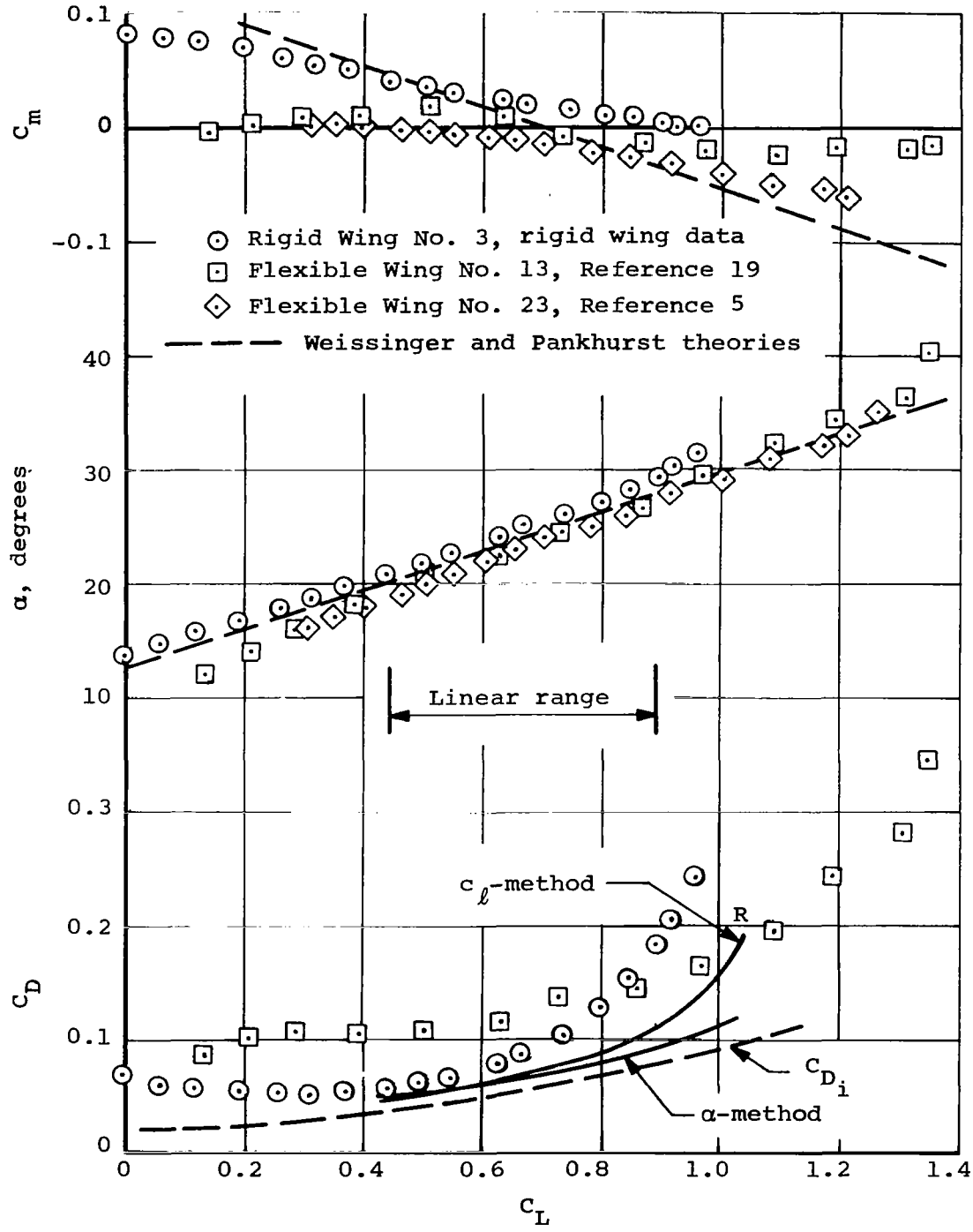

(c) $\Lambda_o = 45^o$.

Figure 18.- Continued.

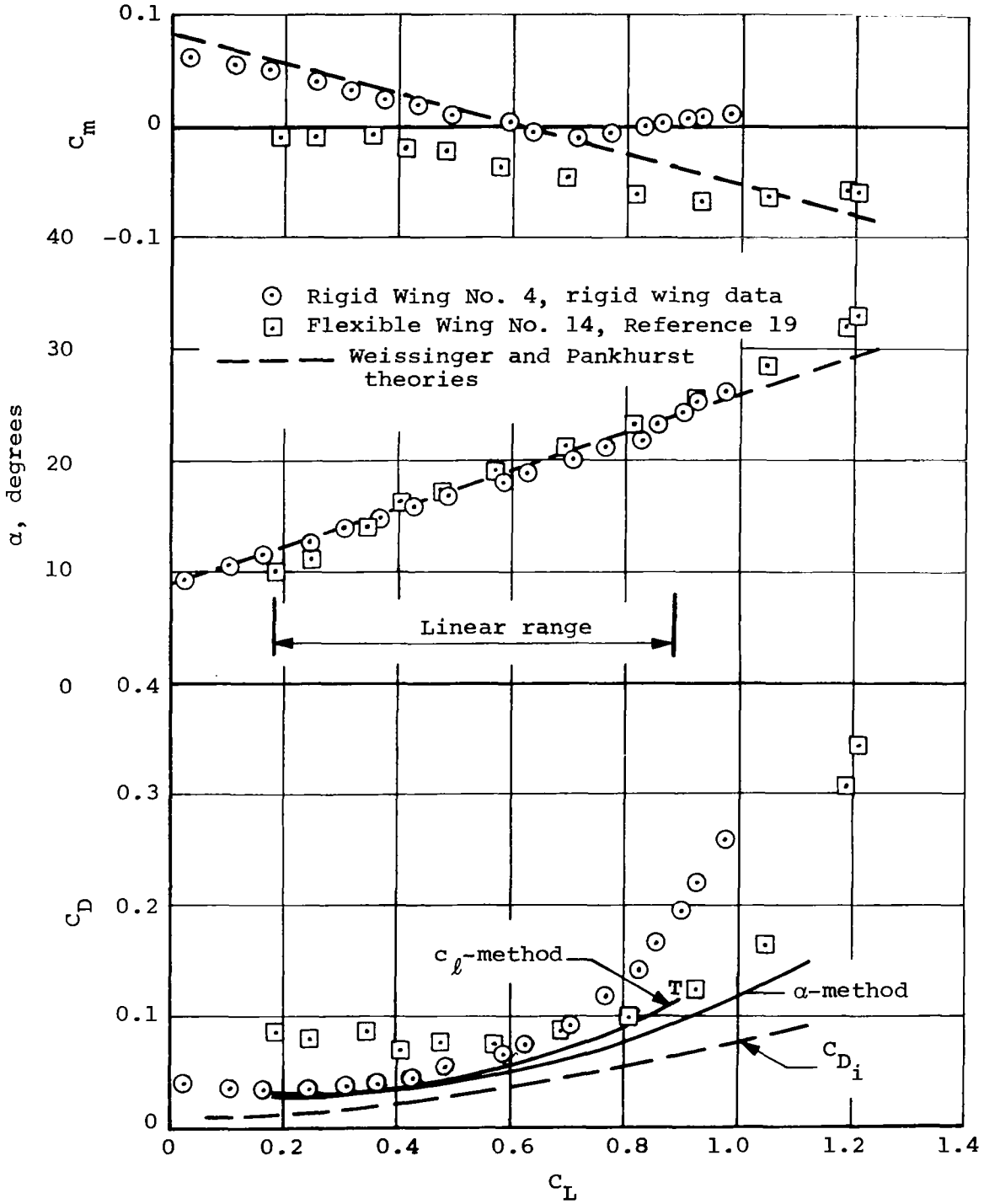

(d) $\Lambda_o = 47.5^o$.

Figure 18.- Concluded.

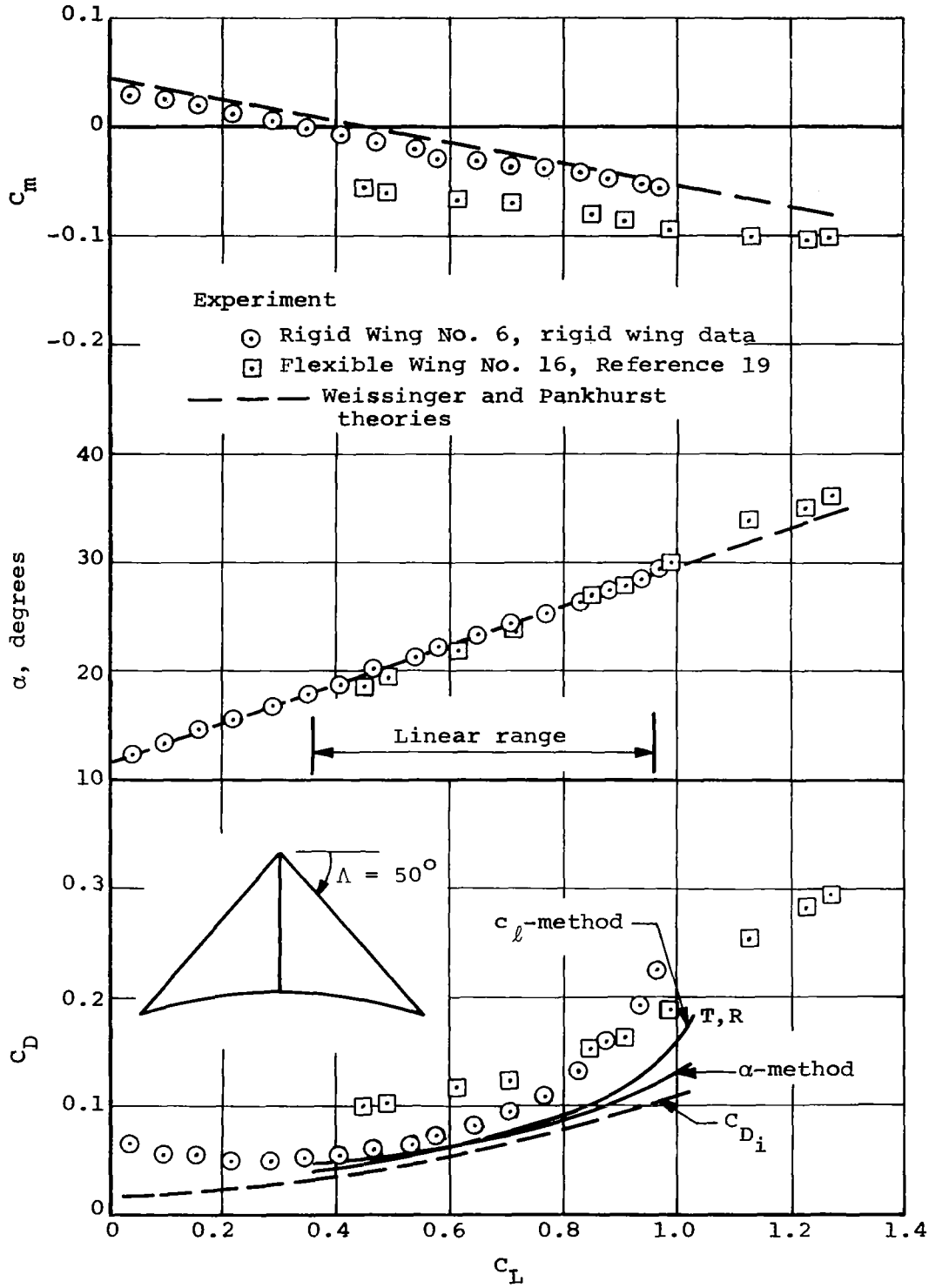

Figure 19.- Comparison between experimental and predicted characteristics of rigid and flexible wings of aspect ratio 4.0, $\Lambda = 50^\circ$, $\Lambda_o = 45^\circ$.

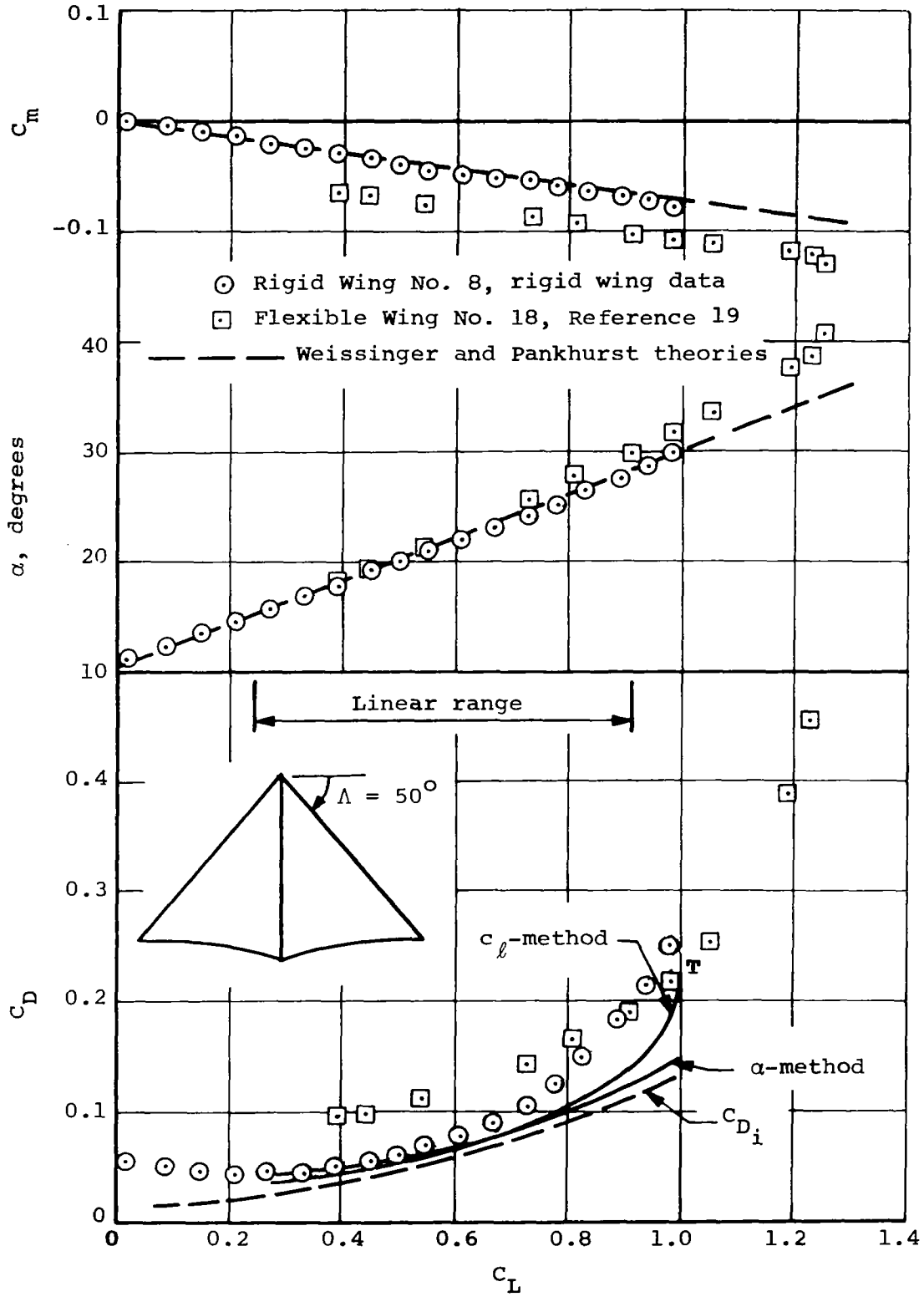

Figure 20.- Comparison between experimental and predicted characteristics of rigid and flexible wings of aspect ratio 3.0, $\Lambda = 50^\circ$, $\Lambda_o = 45^\circ$.

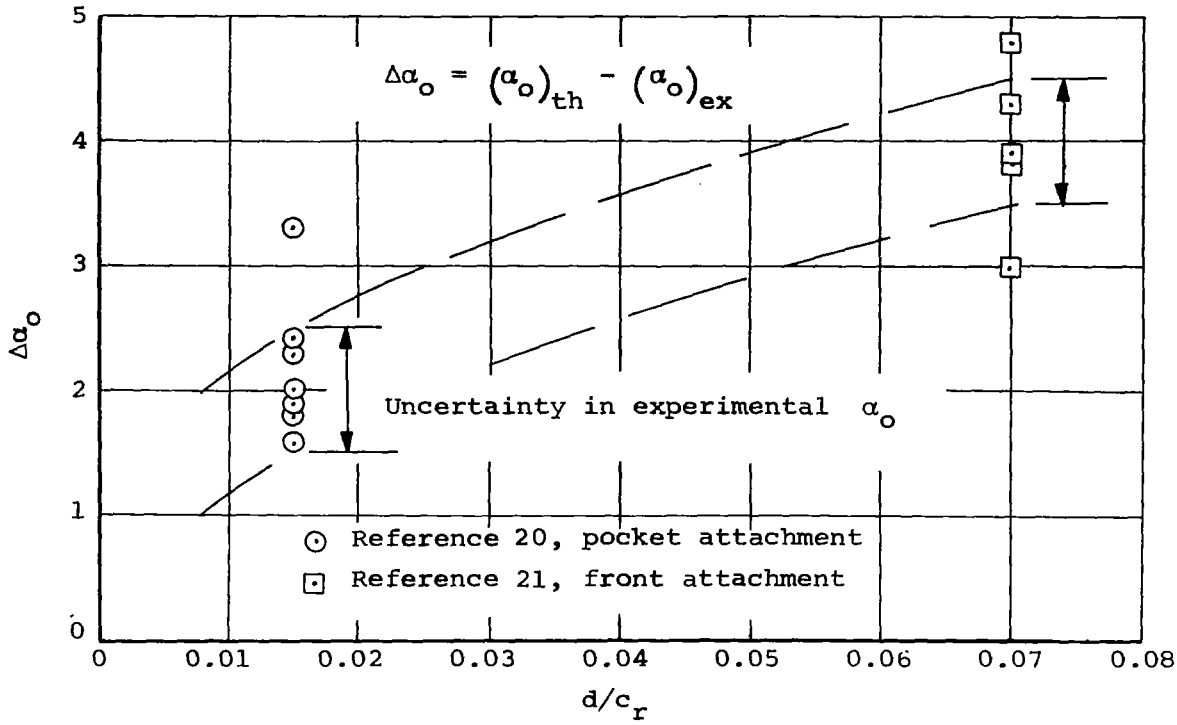

(a) NASA planform parawings with constant diameter leading-edge booms.

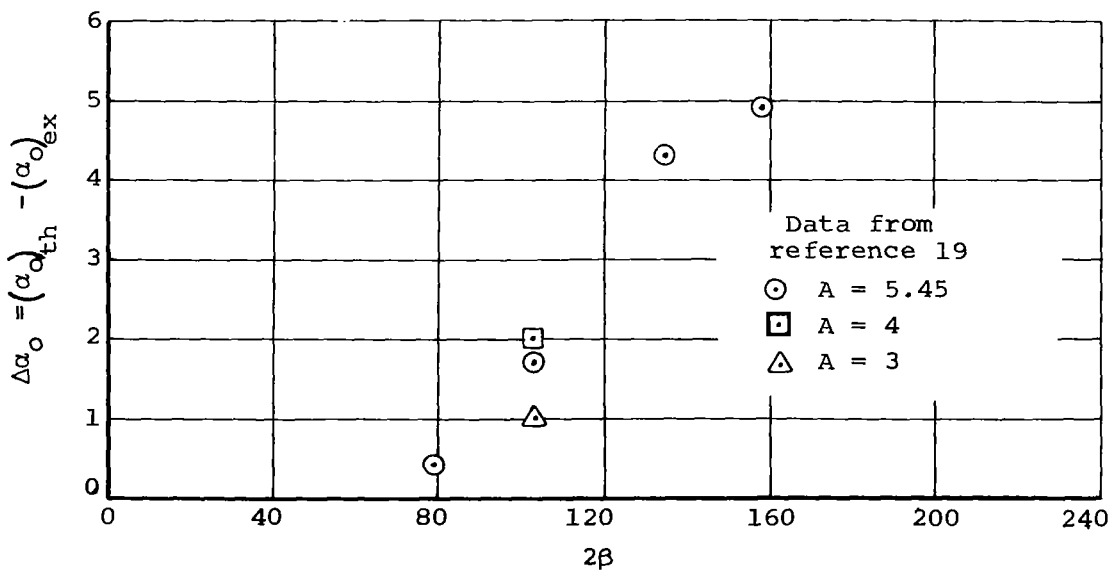

(b) Flexible parawings with tapered leading-edge booms, front attachment.

Figure 21.- Differences between measured and predicted angles of zero lift for flexible parawings.

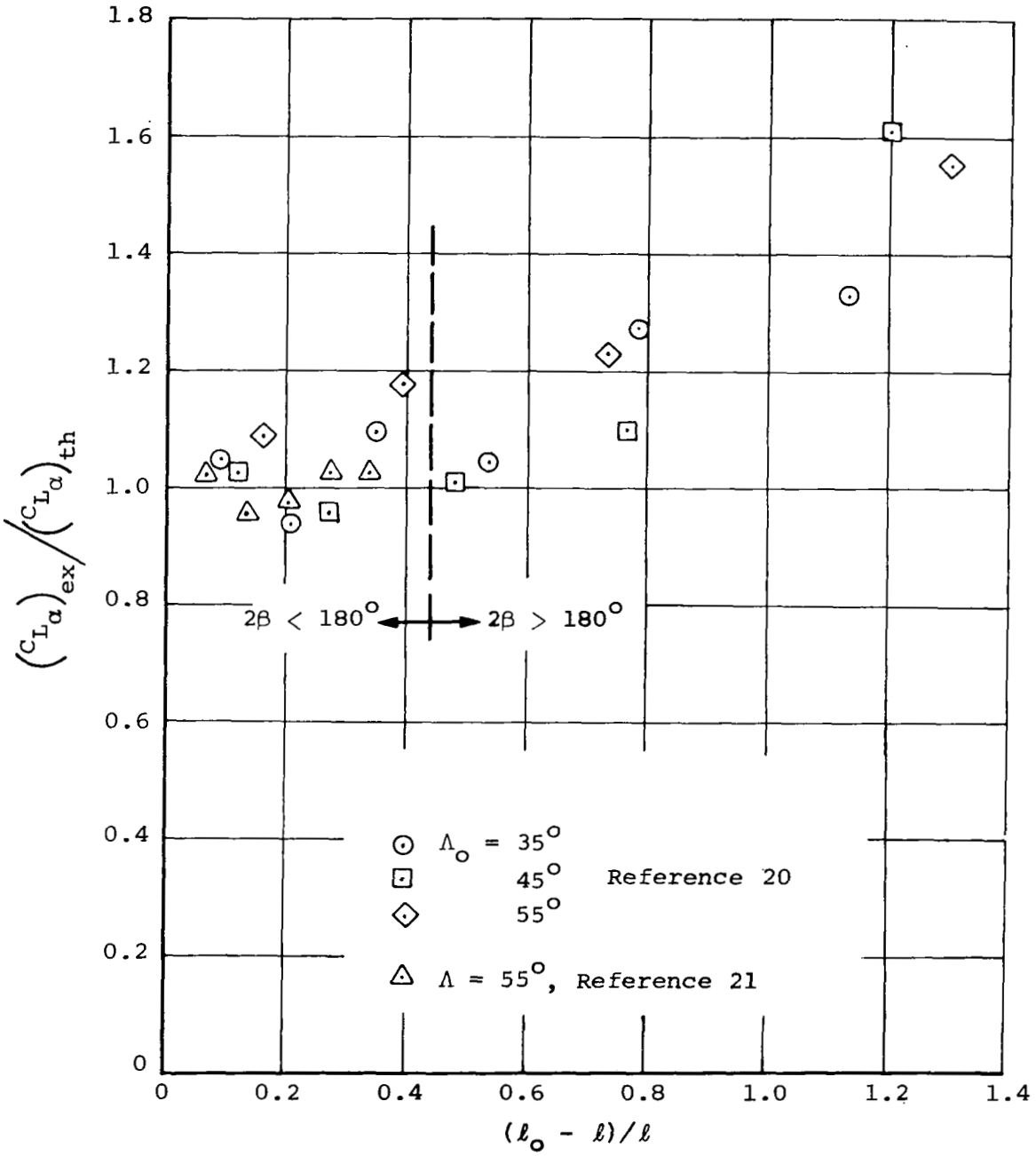

(a) NASA planform parawings with constant diameter leading-edge booms.

Figure 22.- Effect of slackness ratio on the lift-curve slope of two-lobed parawings.

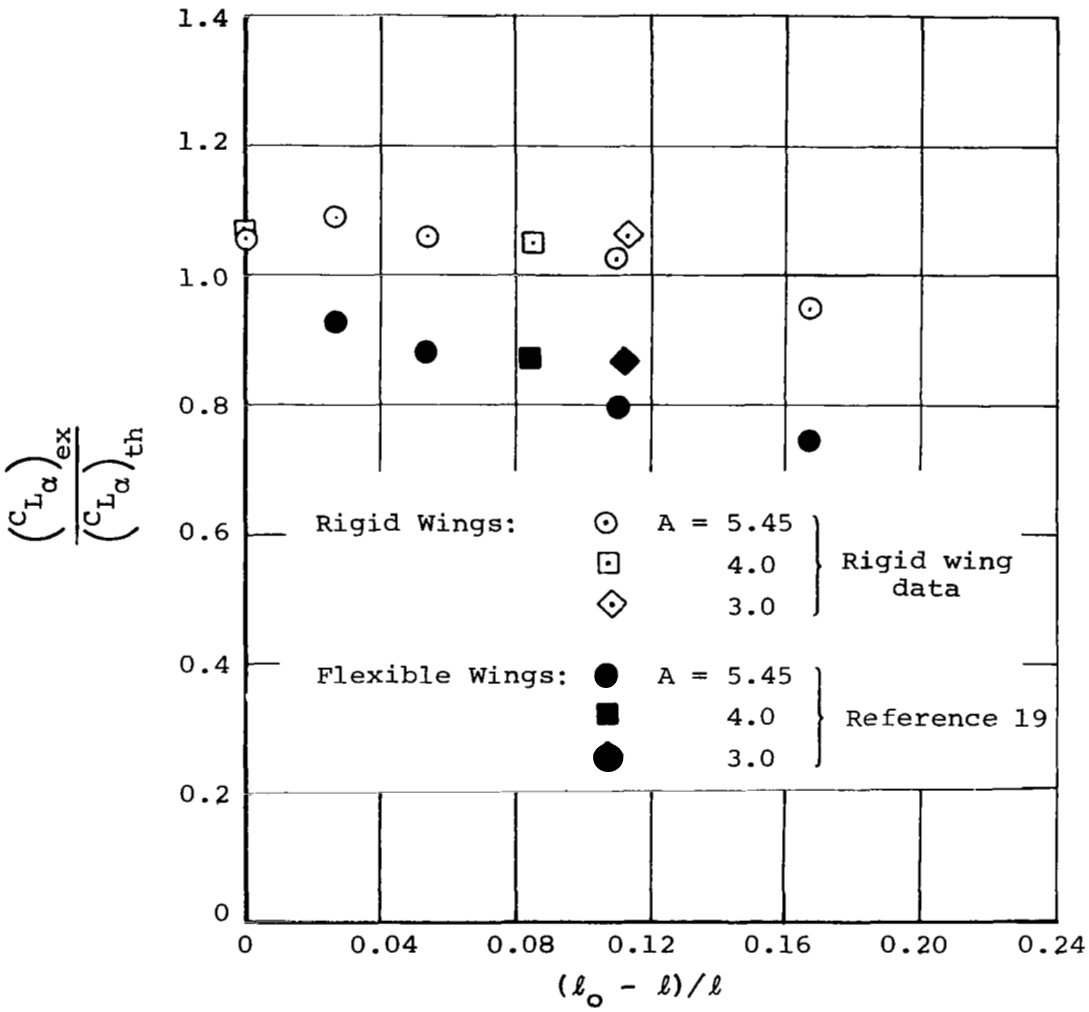

(b) Rigid parawings and flexible parawings with tapered leading-edge booms, front attachment.

Figure 22.- Concluded.

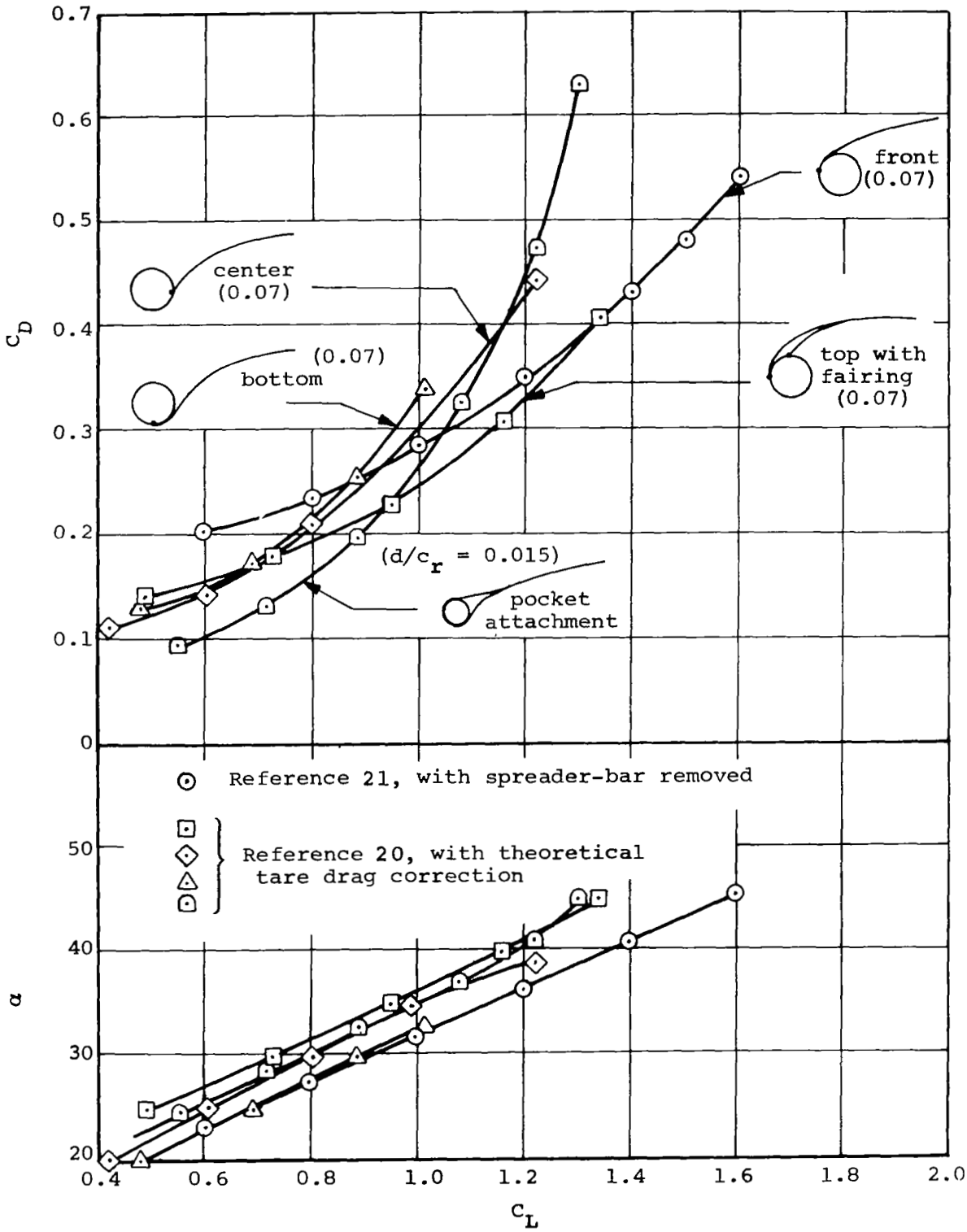

Figure 23.- Effects of leading-edge diameter and canopy attachment methods on aerodynamic characteristics of flexible NASA planform parawings, $\Lambda_o = 45^o$, $\Lambda = 55^o$.

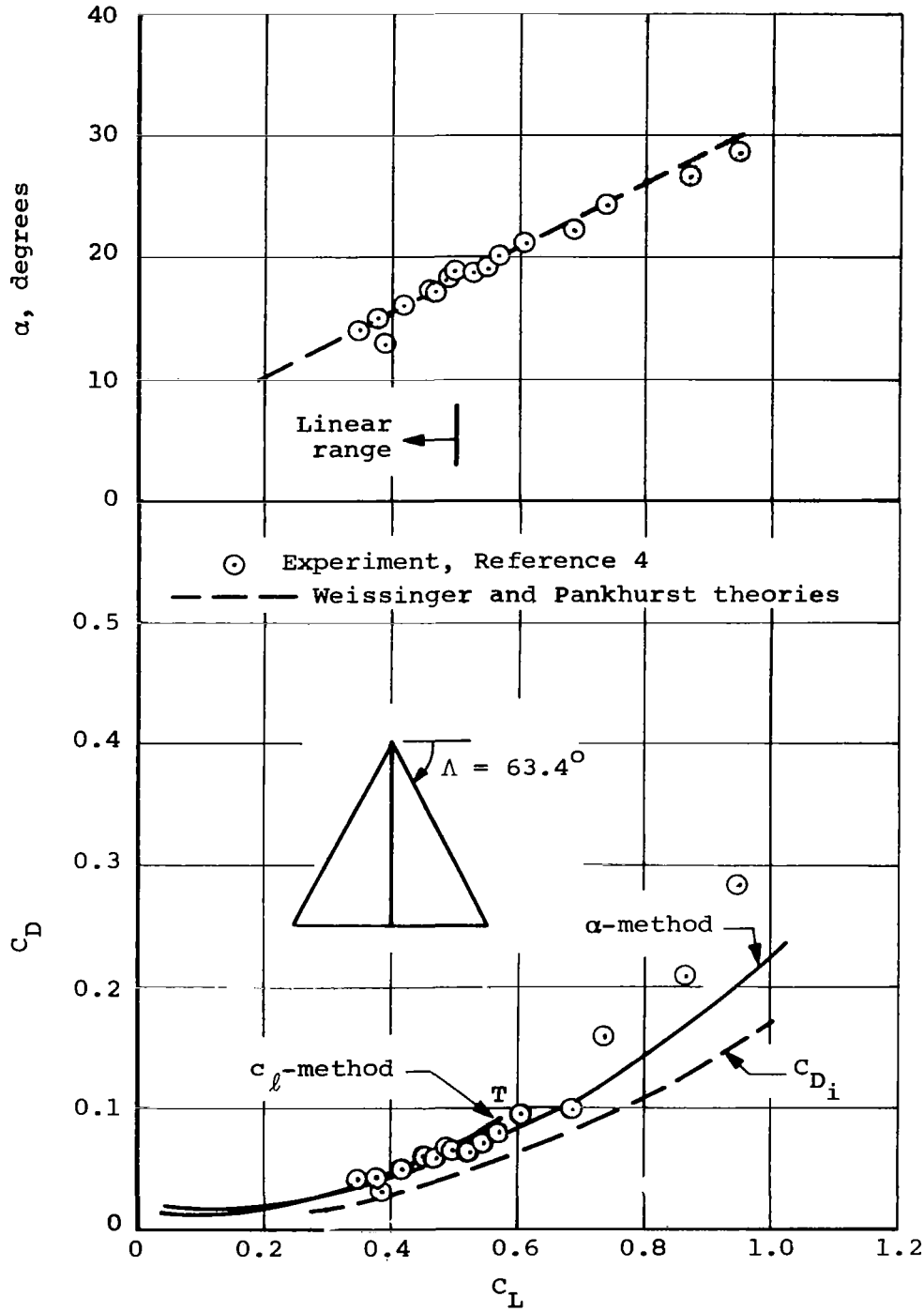

(a) Wing No. AR2-2.07, A = 2.0, 2β = 74.2°.

Figure 24.- Comparison between experimental and predicted characteristics of triangular parawings with small constant-diameter leading-edge booms with front attachment.

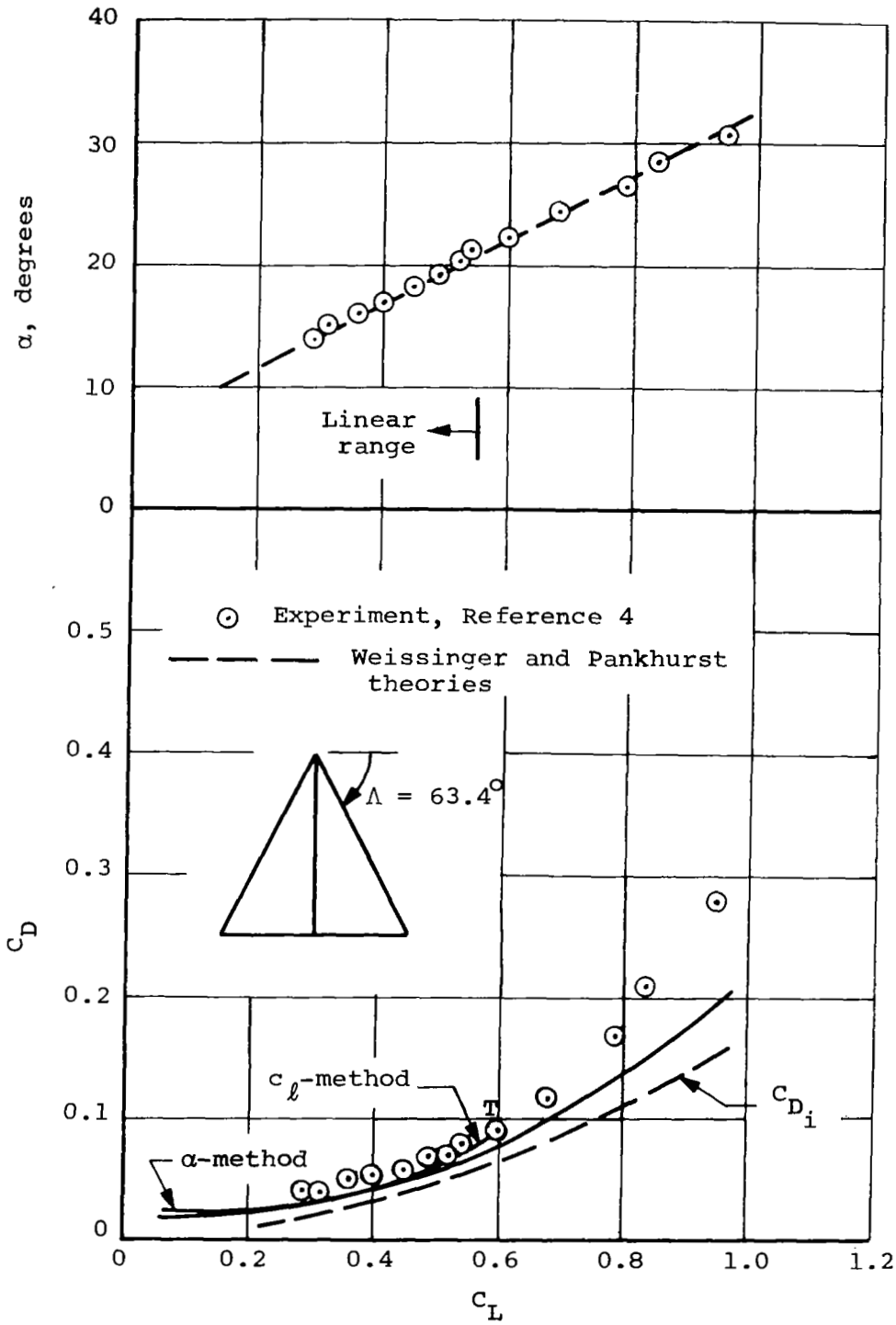

(b) Wing No. AR2-2.10, A = 2.0, 2β = 90.3°.

Figure 24.- Continued.

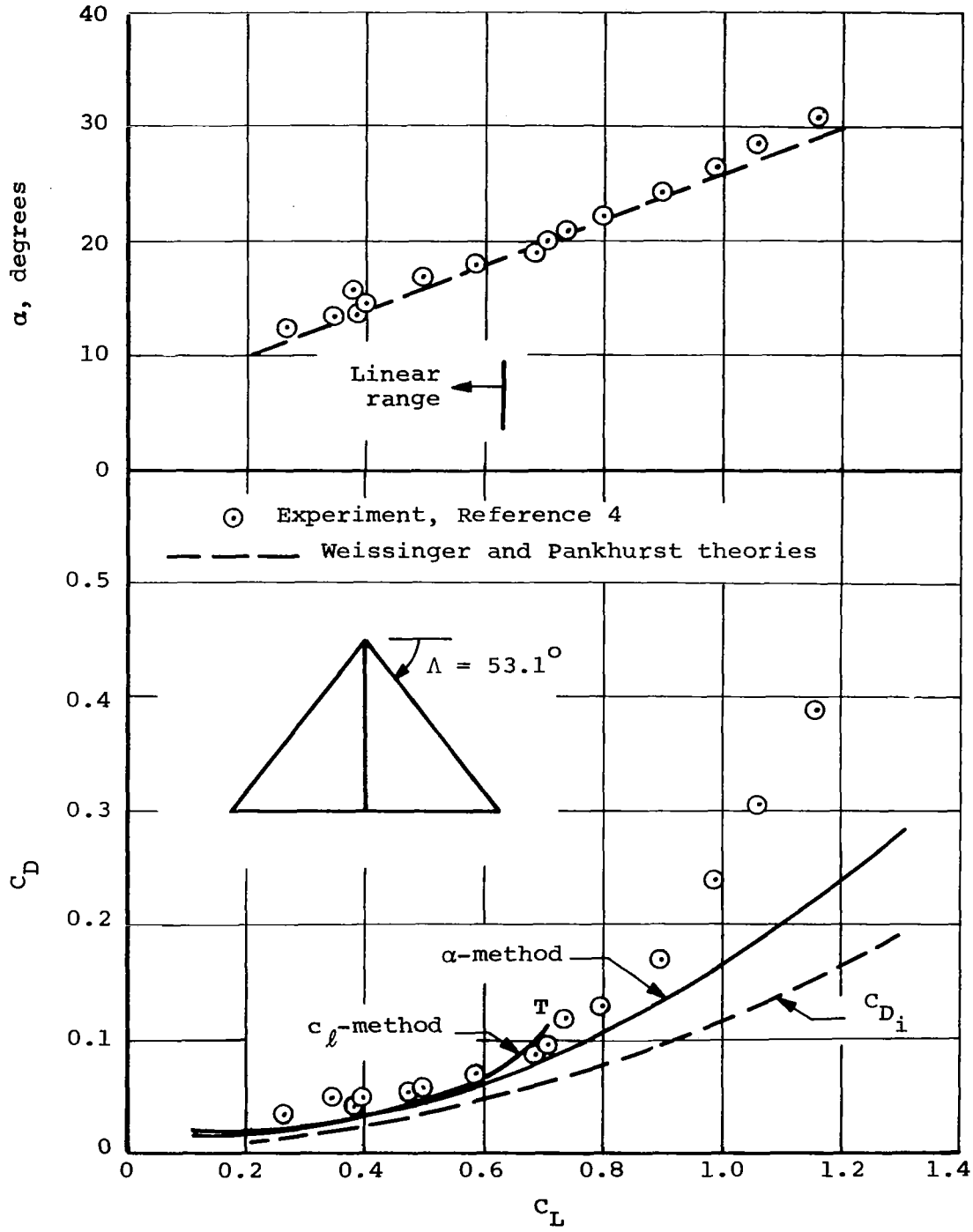

(c) Wing No. AR3-2.04, A = 3.0, 2β = 68.9°.

Figure 24.- Concluded.

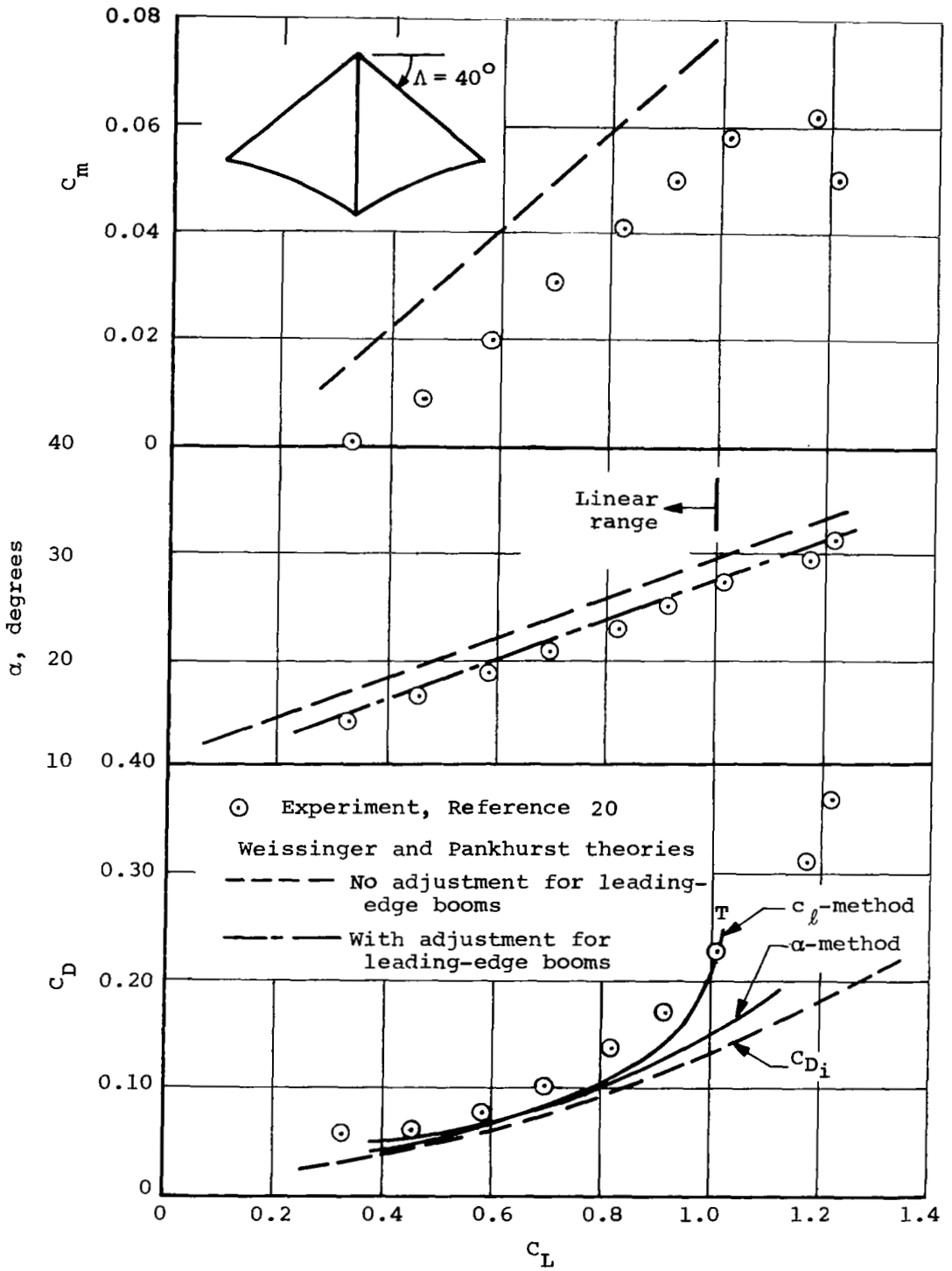

(a) $\Lambda_o = 35^\circ$, $\Lambda = 40^\circ$, $2\beta = 98.8^\circ$.

Figure 25.- Comparison between experimental and predicted characteristics of flexible NASA planform parawings with small constant-diameter leading-edge booms with pocket attachment.

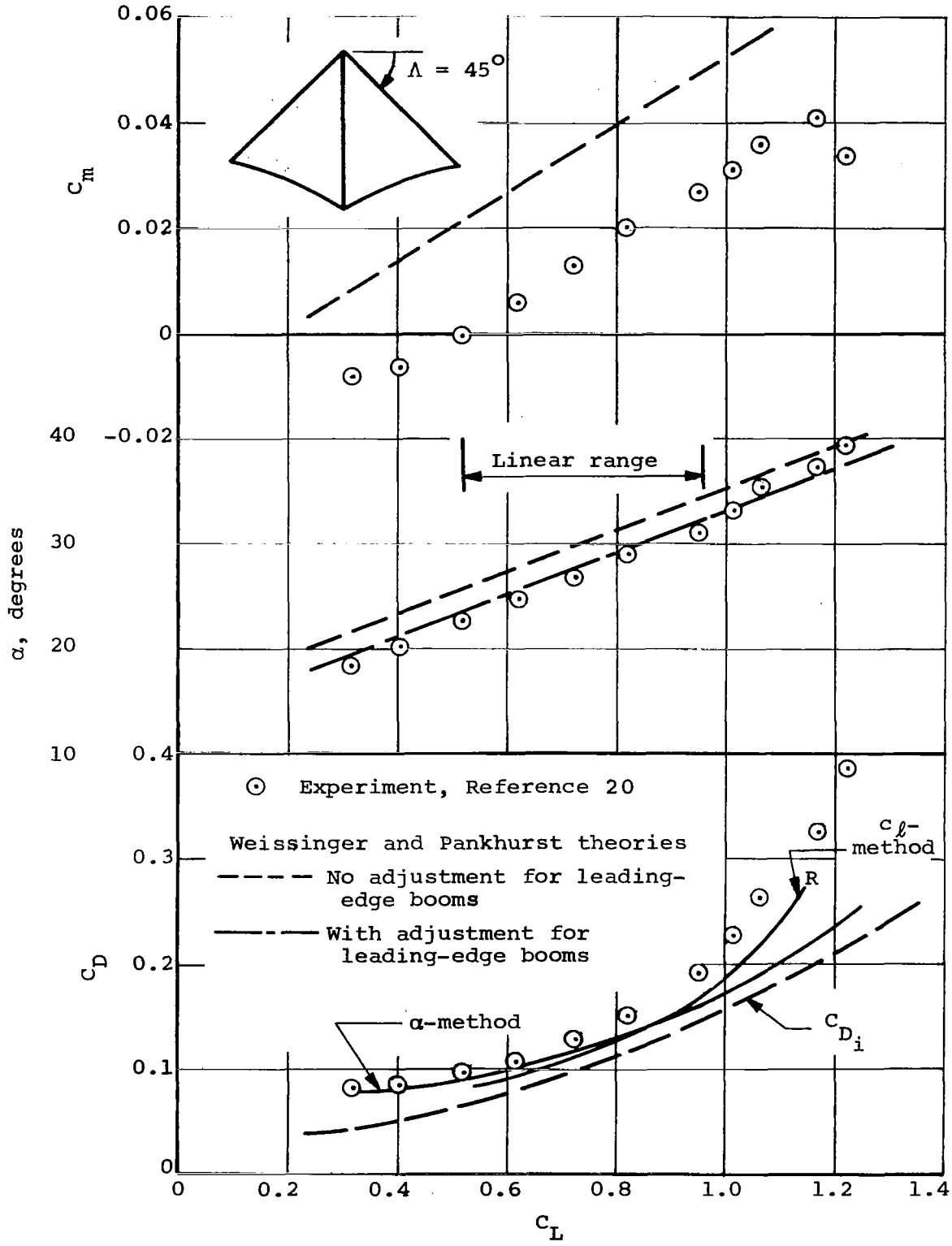

(b) $\Lambda_o = 35^\circ$, $\Lambda = 45^\circ$, $2\beta = 130.5^\circ$.

Figure 25.- Continued.

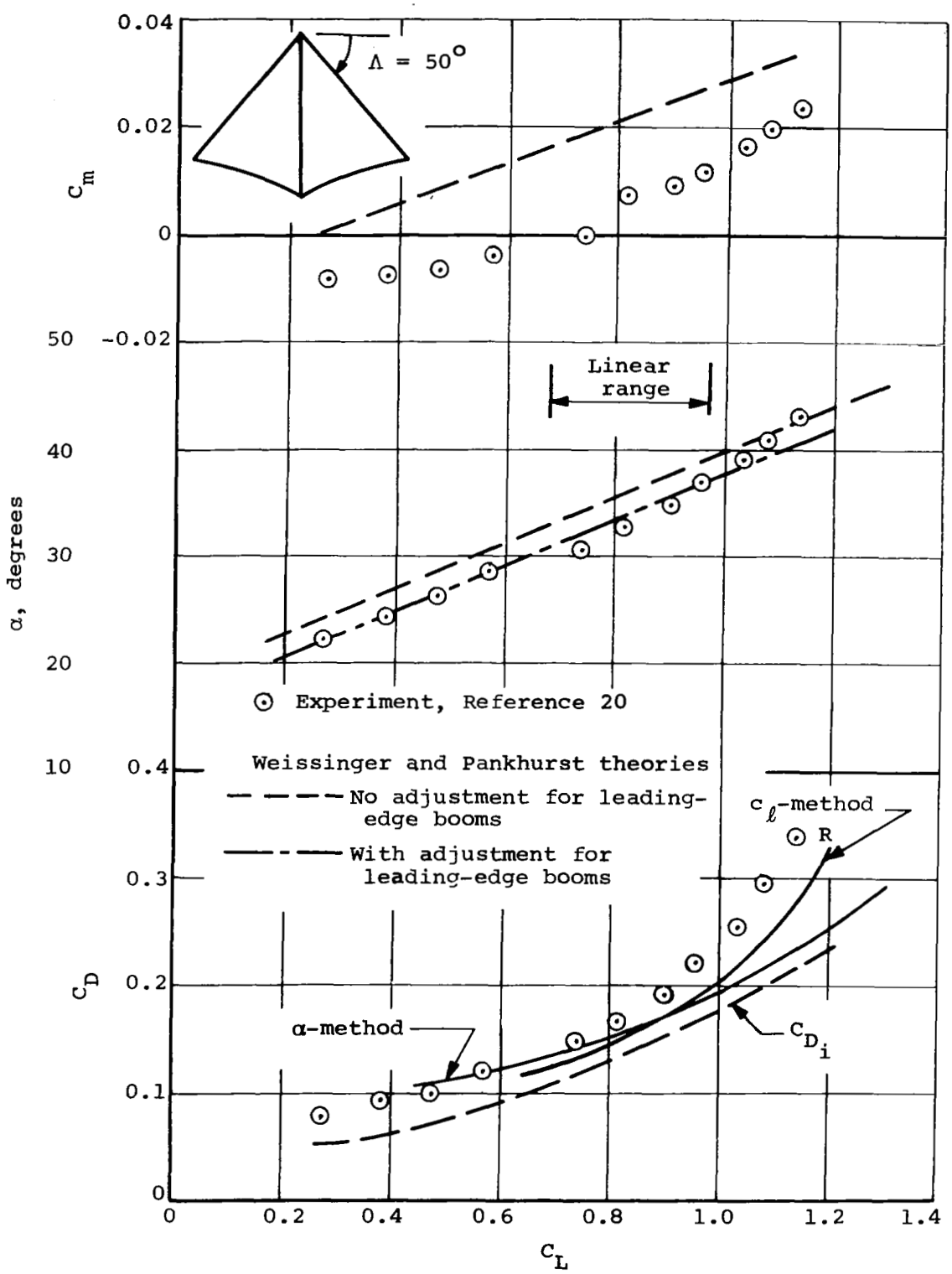

(c) $\Lambda_o = 35^\circ$, $\Lambda = 50^\circ$, $2\beta = 157.8^\circ$.

Figure 25.- Continued.

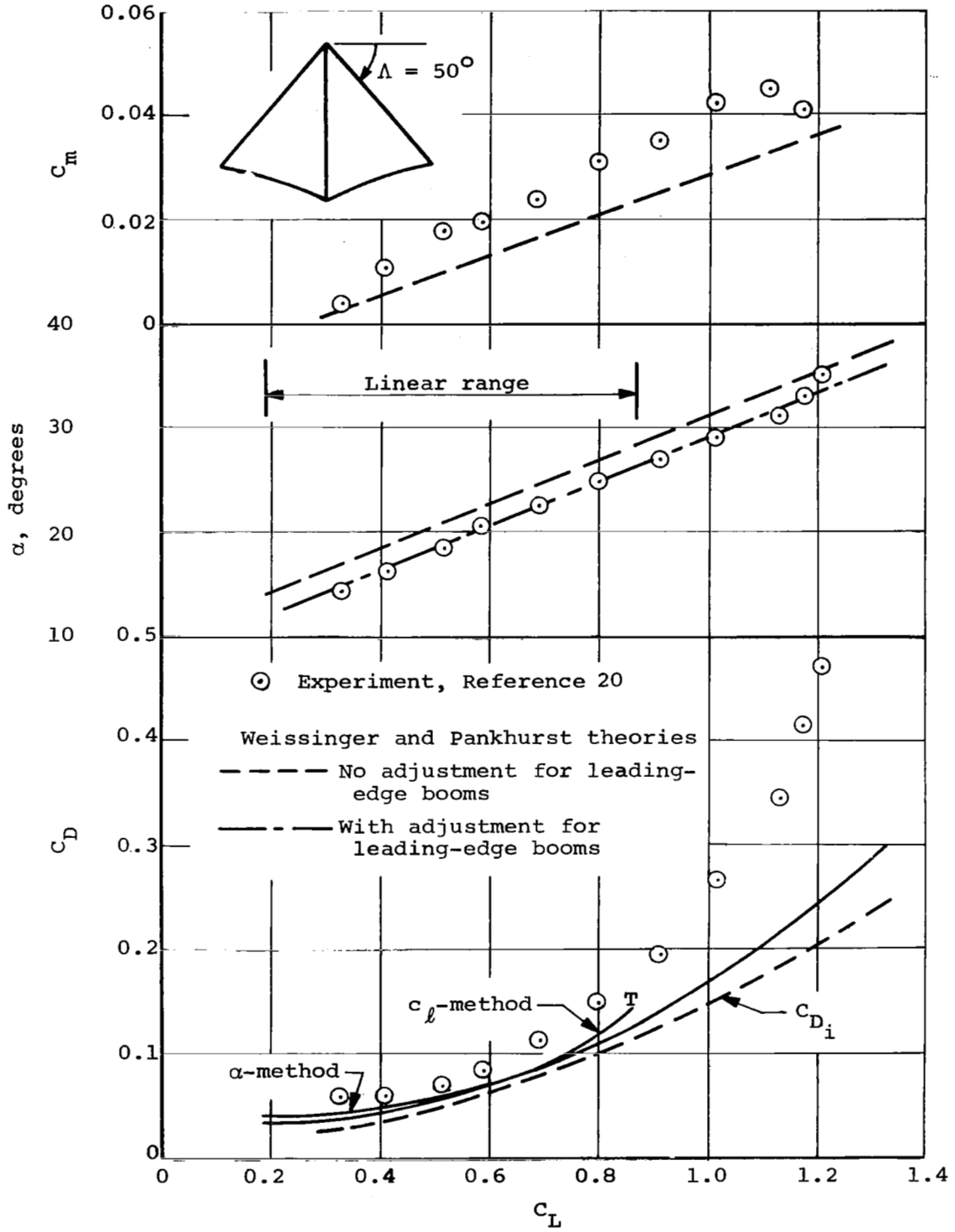

(d) $\Lambda_o = 45^\circ$, $\Lambda = 50^\circ$, $2\beta = 102.9^\circ$.

Figure 25.- Continued.

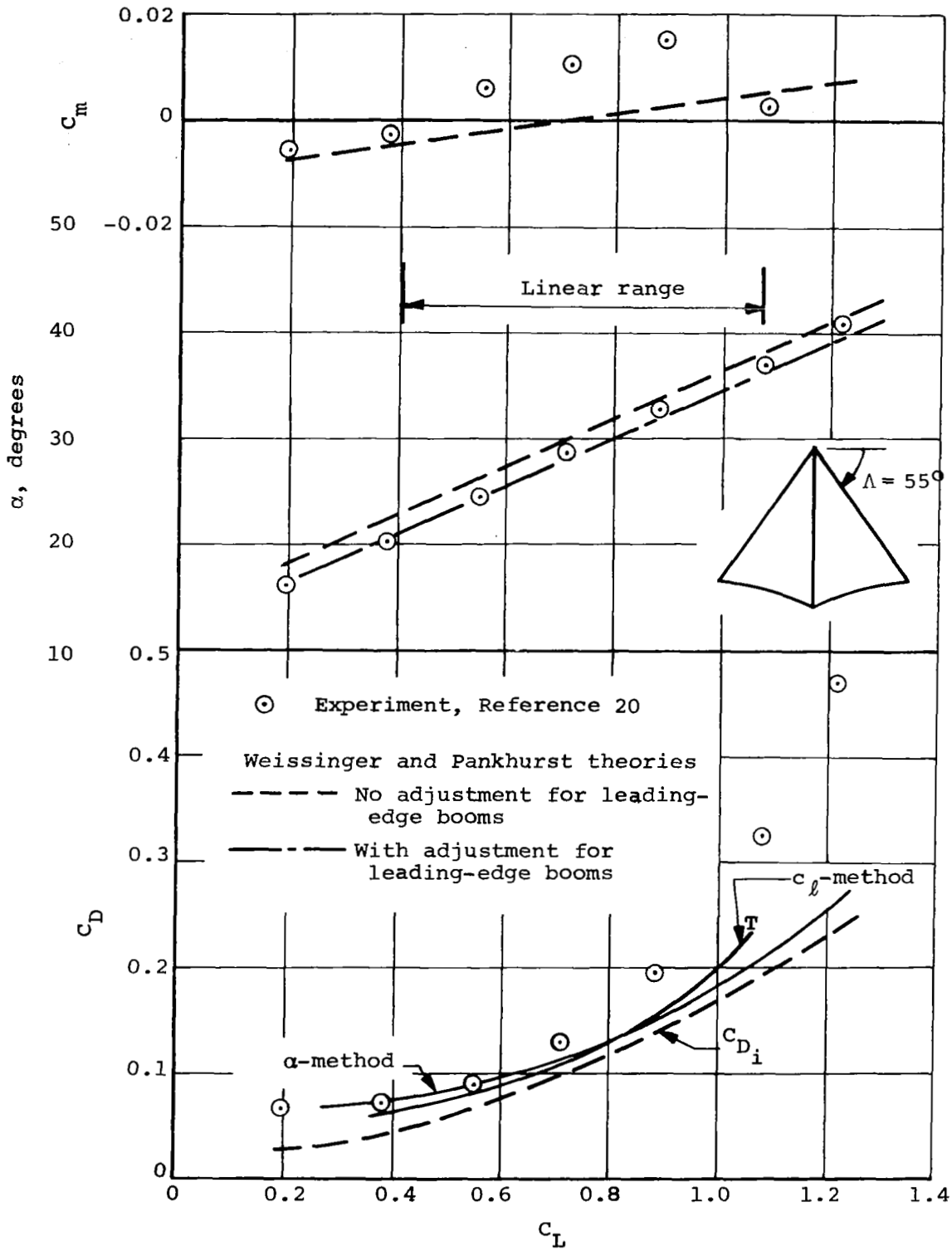

(e) $\Lambda_o = 45^\circ$, $\Lambda = 55^\circ$, $2\beta = 141.1^\circ$.

Figure 25.- Continued.

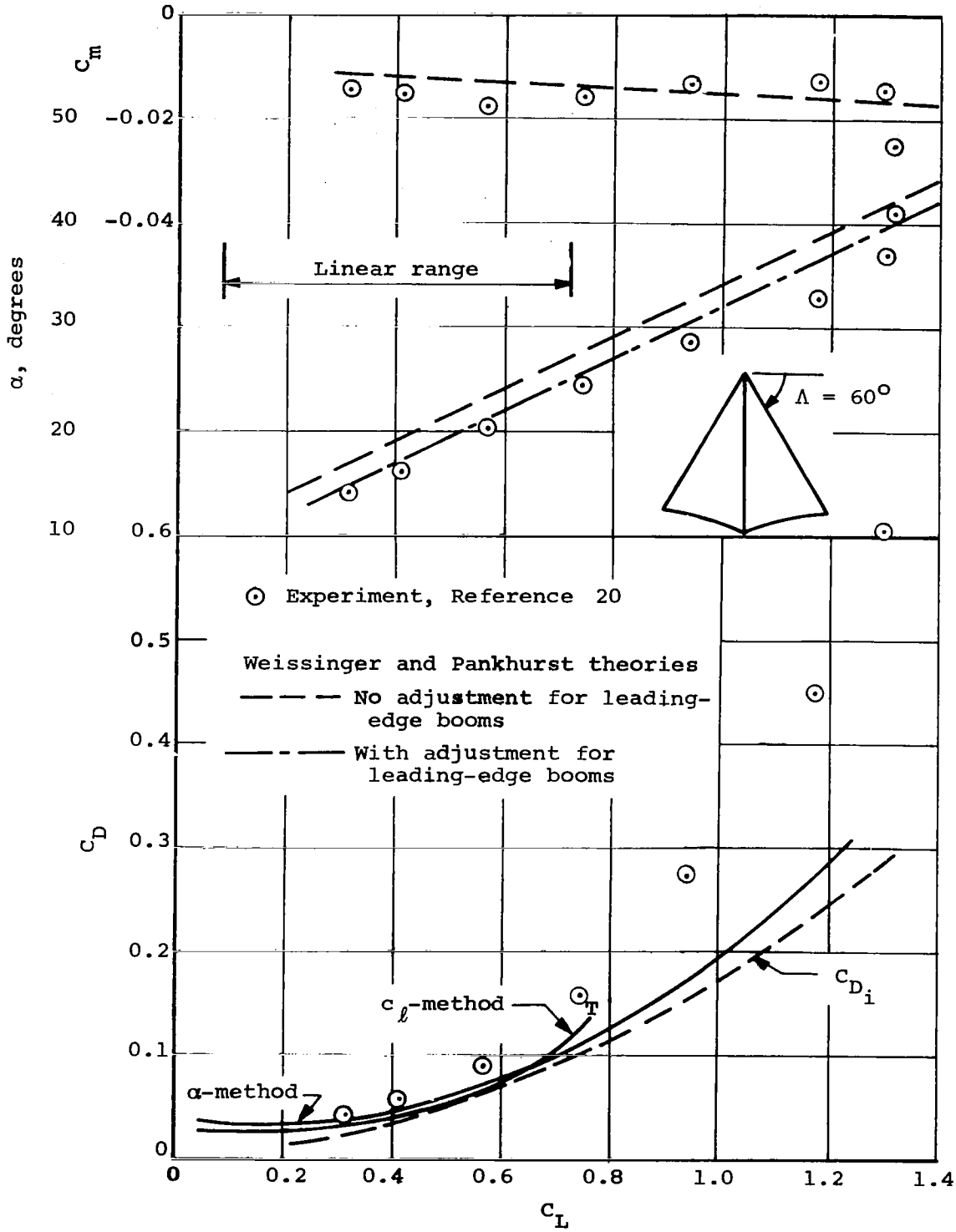

(f) $\Lambda_o = 55^\circ$, $\Lambda = 60^\circ$, $2\beta = 133.9^\circ$.

Figure 25.- Continued.

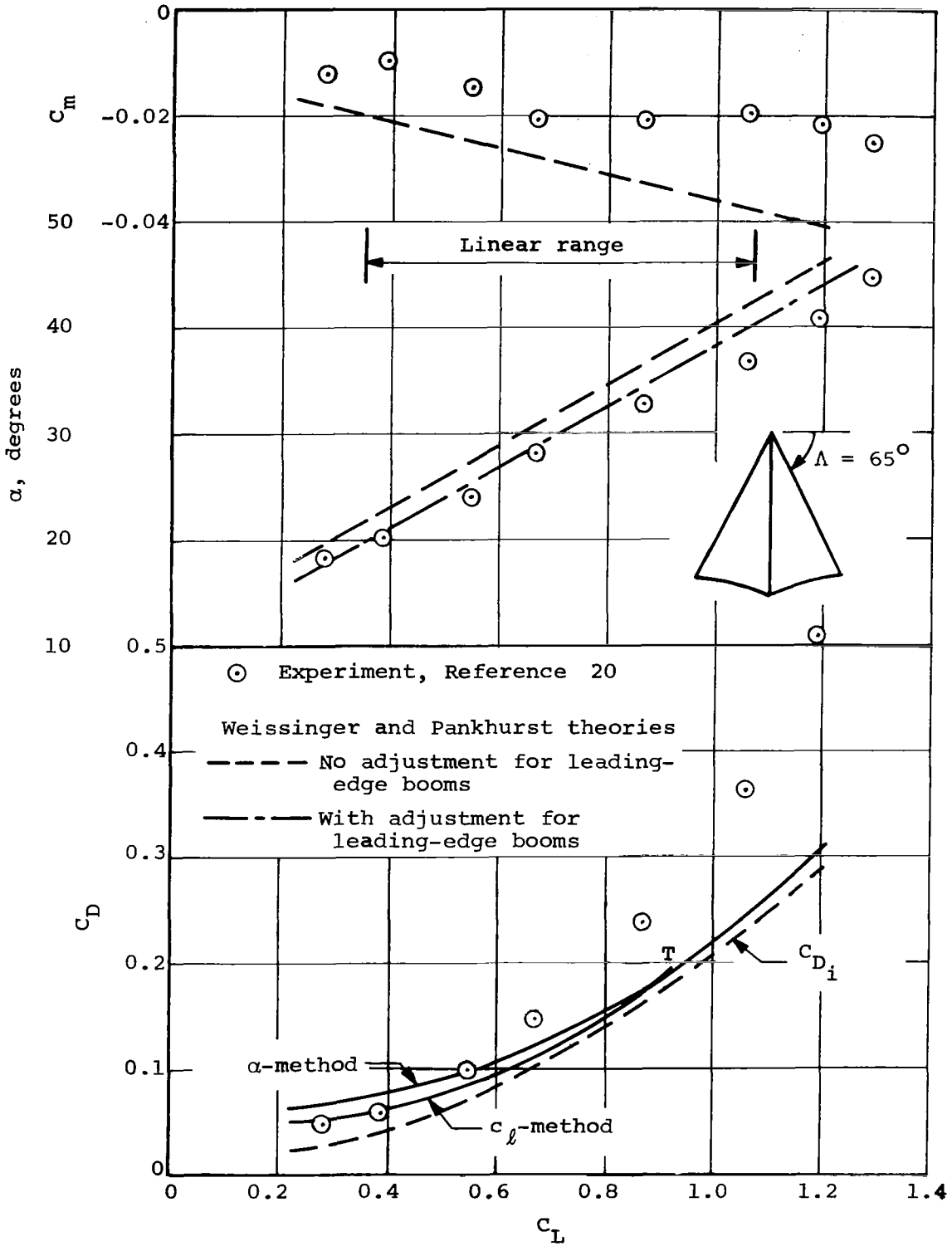

(g) $\Lambda_o = 55^\circ$, $\Lambda = 65^\circ$, $2\beta = 159.0^\circ$.

Figure 25.- Concluded.

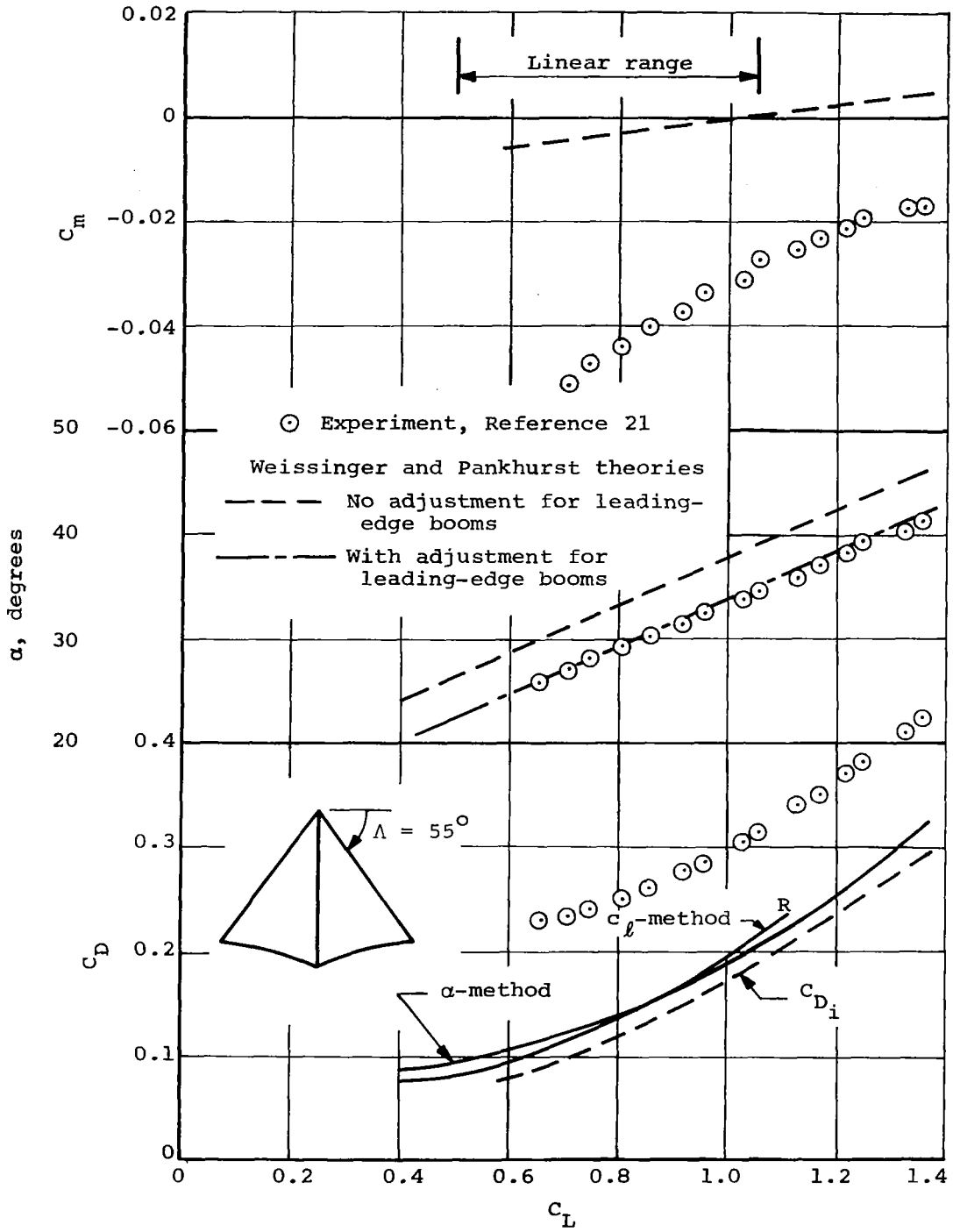

(a) $\Lambda = 42.5^\circ$, $2\beta = 153.8^\circ$.

Figure 26.- Comparison between experimental and predicted characteristics of flexible NASA planform parawings, $\Lambda = 55^\circ$ with large constant-diameter leading-edge booms with front attachment.

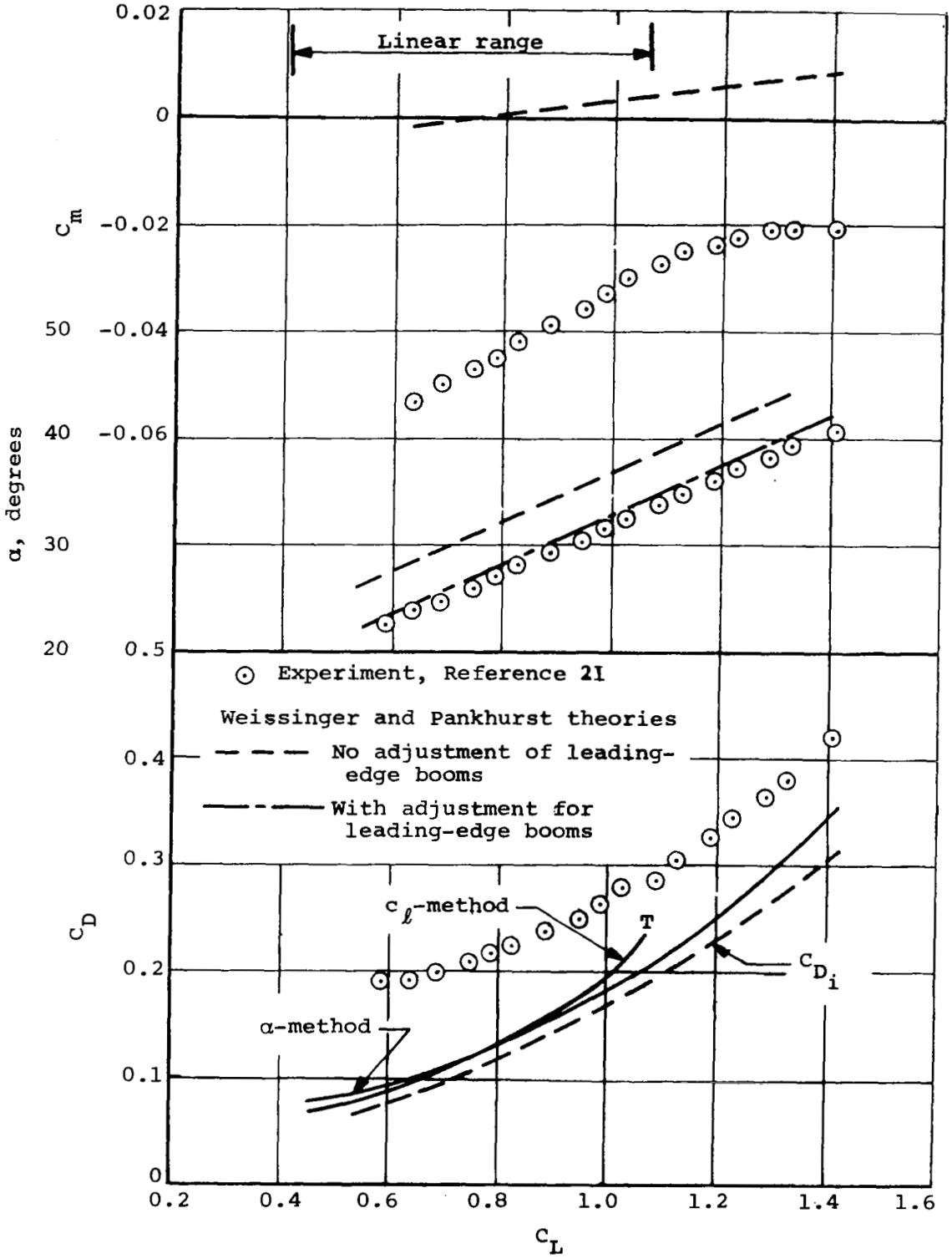

(b) $\Lambda_o = 45^\circ$, $2\beta = 141.1^\circ$.

Figure 26.- Continued.

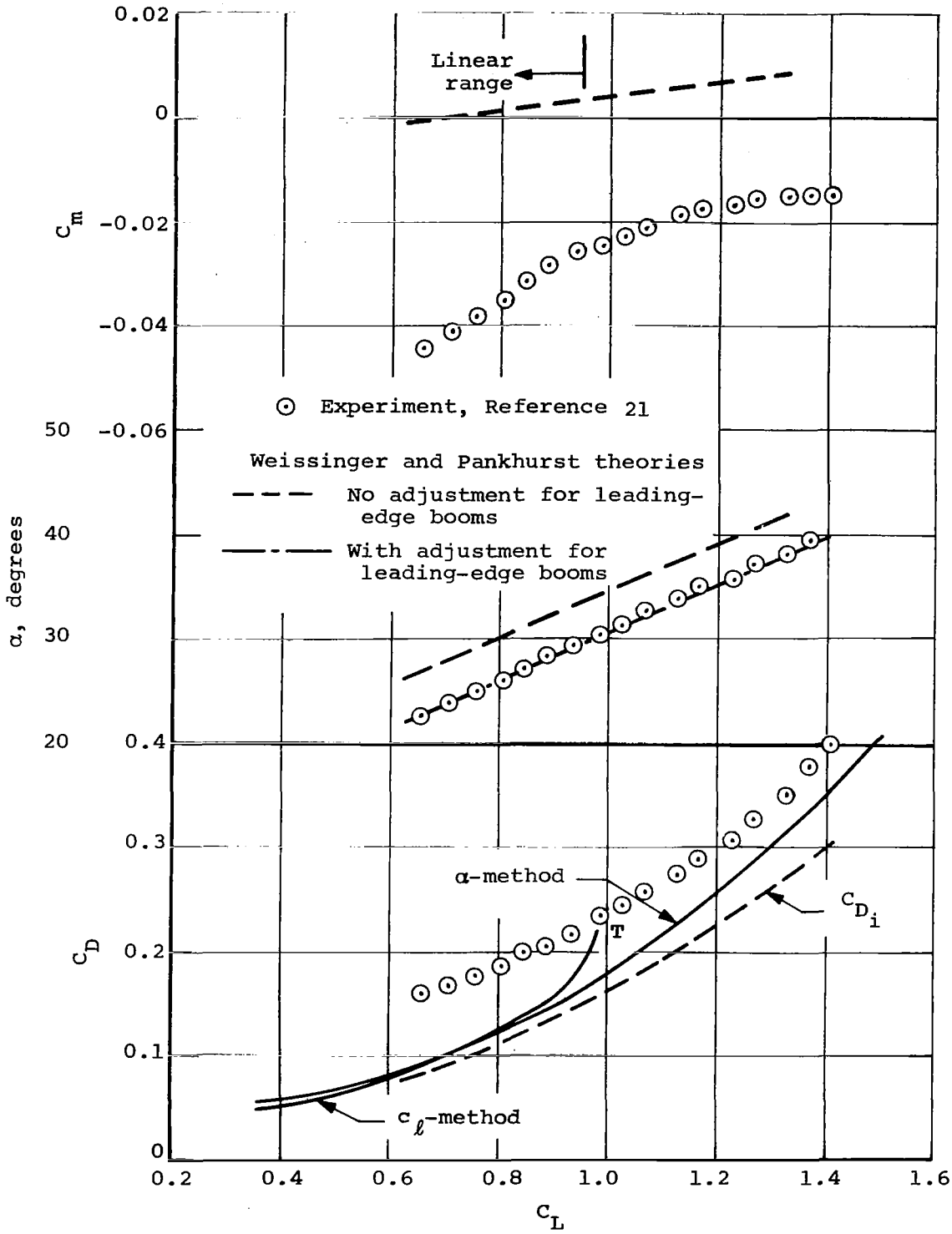

(c) $\Lambda_o = 47.5^o$, $2\beta = 125.8^o$.

Figure 26.- Continued.

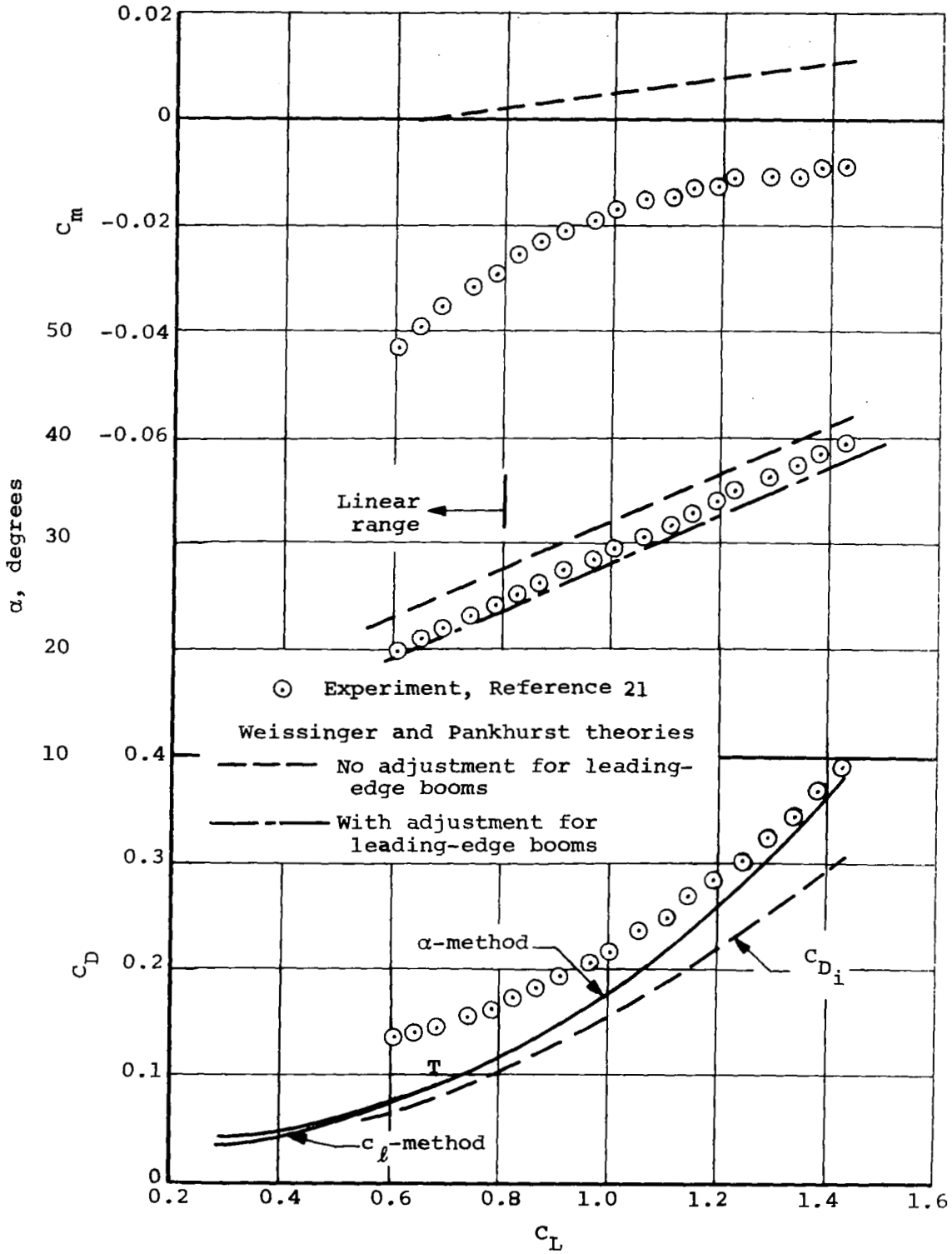

(d) $\Lambda_o = 50^o$, $2\beta = 106.8^o$.

Figure 26.- Continued.

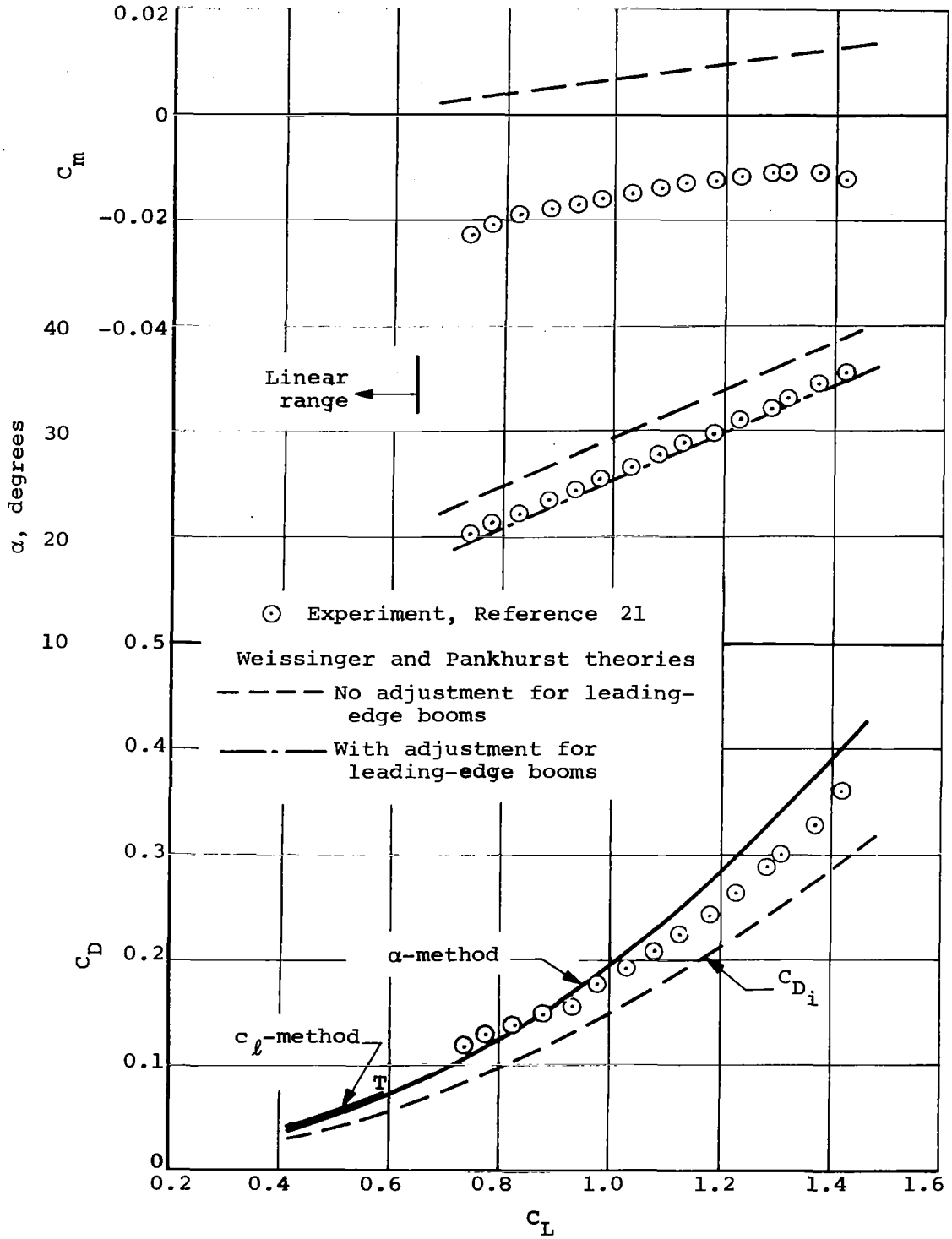

(e) $\Lambda_o = 52.5^\circ$, $2\beta = 80.9^\circ$.

Figure 26.- Concluded.

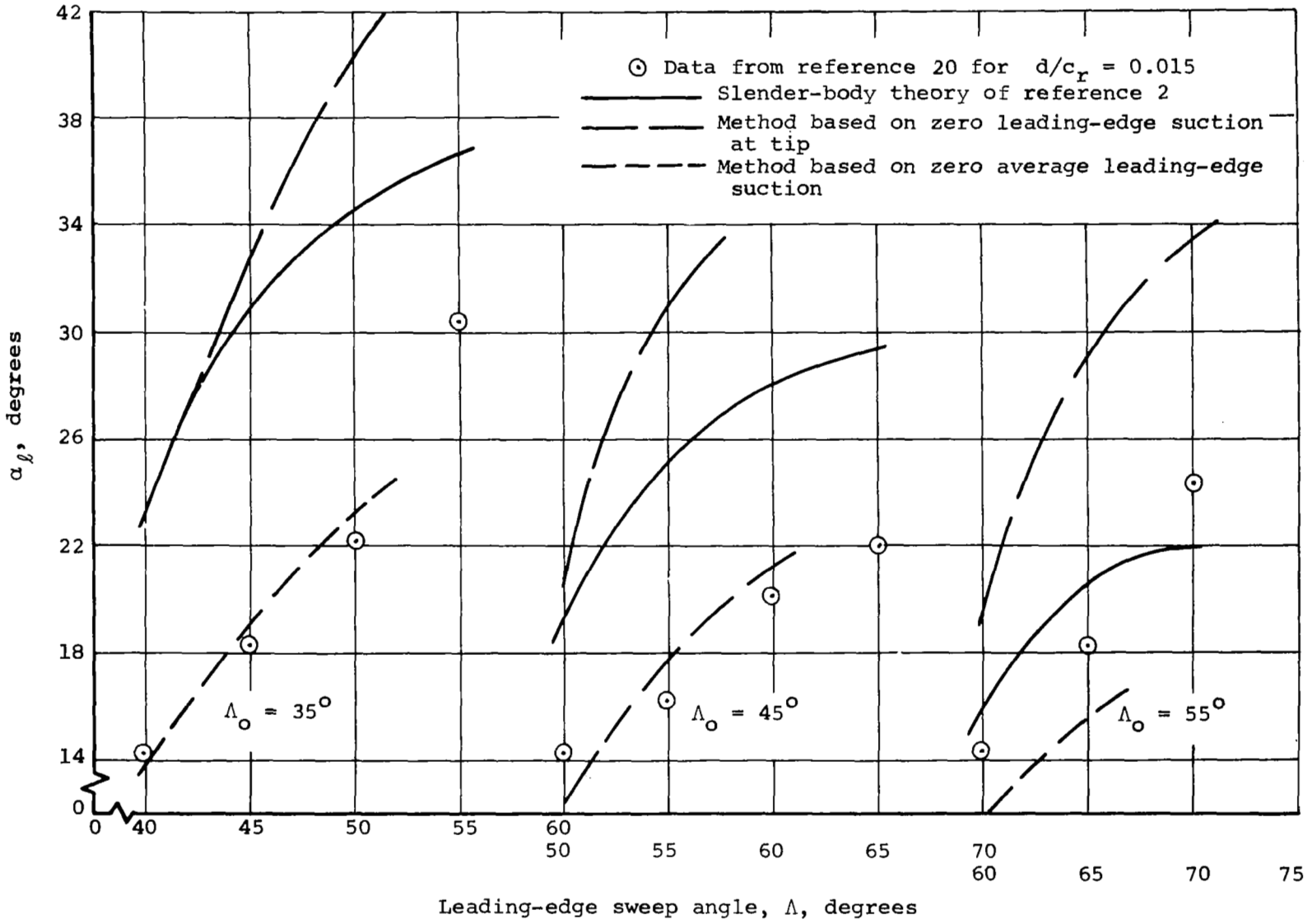

Figure 27.- Predicted and measured luffing angle of attack for NASA planforms.